

10-A093 466

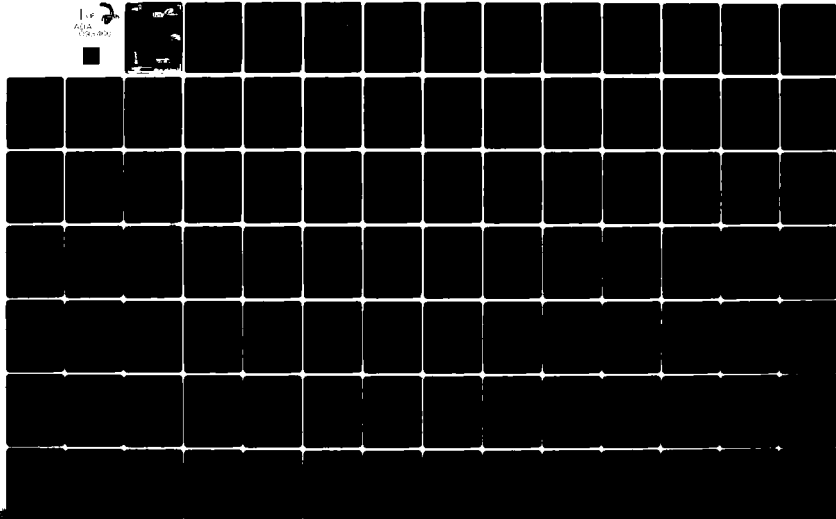
ATMOSPHERIC AND ENVIRONMENTAL RESEARCH INC CAMBRIDGE MA F/G 17/B  
INVESTIGATION OF THE EFFECT OF LOW LEVEL MARITIME HAZE ON DMSP --ETC(U)  
SEP 80 R 6 ISAACS

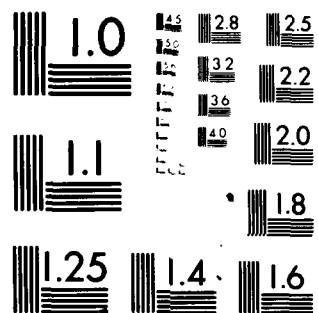
N00014-80-C-0262

NL

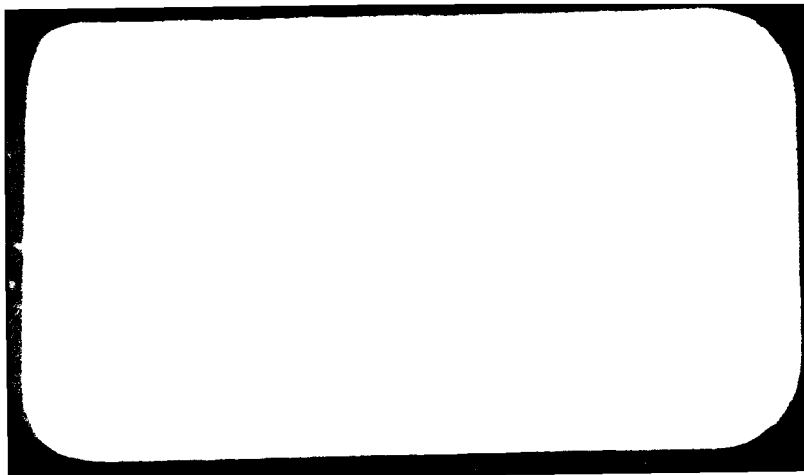
UNCLASSIFIED

10-A093 466





MICROCOPY RESOLUTION TEST CHART  
NATIONAL BUREAU OF STANDARDS-1963-A



INVESTIGATION OF THE EFFECT OF  
LOW LEVEL MARITIME HAZE ON DMSP  
VHR AND LF IMAGERY

RECEIVED  
JAN 2 1981  
C

prepared by:

Ronald G. Isaacs

Atmospheric and Environmental Research, Inc. ✓  
872 Massachusetts Avenue  
Cambridge, Massachusetts 02139

April 1, 1980 - September 30, 1980

Prepared under Contract Number:  
N00014 80-C-0262

Office of Naval Research  
Arlington, Virginia 22217

Reproduction in whole or in part is permitted for  
any purpose of the United States Government. This  
work funded by the Naval Environmental Prediction  
Facility under Program Element 62759N, Project  
9F 52551792 "Atmospheric Environmental Support."

DISTRIBUTION STATEMENT A

Approved for public release  
Distribution unlimited

ATMOSPHERIC AND ENVIRONMENTAL RESEARCH, INC.

872 MASSACHUSETTS AVENUE  
CAMBRIDGE, MASSACHUSETTS 02139

November 4, 1980

AREA CODE 617 547-6207  
547-6328

Defense Technical Information Center  
Bldg. 5, Cameron Station  
Alexandria, VA 22314

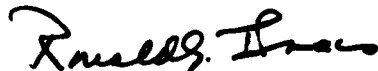
Subject: Submission of Final Report  
Contract No. N0014 80-C-0262  
Period of Performance: April 1-September 30, 1980

Dear Sir:

Enclosed please find 2 copies of our final report entitled:  
"Investigation of the Effect of Low Level Maritime Haze on DMSP  
VHR and LF Imagery" in fulfillment of contractual obligations  
for the period April 1 - September 30, 1980 under contract  
N0014 80-C-0262.

This report includes amendments and corrections to the draft  
submitted earlier in response to and coordinated by Mr. R. Fett,  
Tactical Applications Department, NEPRF, Monterey, CA.

Very truly yours,



Ronald G. Isaacs  
Principal Investigator

RGI/s  
enc.

REPORT DOCUMENTATION PAGE		READ INSTRUCTIONS BEFORE COMPLETING FORM
1. REPORT NUMBER	2. GOVT ACCESSION NO. AD A093 466	3. RECIPIENT'S CATALOG NUMBER
4. TITLE (and Subtitle) INVESTIGATION OF THE EFFECT OF LOW LEVEL MARITIME HAZE ON DMSP VHR AND LF IMAGERY.		5. TYPE OF REPORT & DATES COVERED FINAL REPORT Apr 80 - Sep 80
7. AUTHOR(s) Ronald G. Isaacs		6. PERFORMING ORG. REPORT NUMBER
9. PERFORMING ORGANIZATION NAME AND ADDRESS Atmospheric & Environmental Research, Inc. 872 Massachusetts Avenue Cambridge, MA 02139		8. CONTRACT OR GRANT NUMBER(s) N00014-80-C-1262
11. CONTROLLING OFFICE NAME AND ADDRESS Procuring Contracting Officer Office of Naval Research, Dept. of Navy 800 N. Quincy St., Arlington, VA 32217		10. PROGRAM ELEMENT, PROJECT, TASK AREA & WORK UNIT NUMBERS 9F 52551792
14. MONITORING AGENCY NAME & ADDRESS (if different from Controlling Office) DCASMA 666 Summer Street Boston, MA 02110		12. REPORT DATE 9 Sep 80
16. DISTRIBUTION STATEMENT (of this Report)		13. NUMBER OF PAGES 125
17. DISTRIBUTION STATEMENT (of the abstract entered in Block 20, if different from Report)		15. SECURITY CLASS. (of this report)
18. SUPPLEMENTARY NOTES This work funded by the Naval Environmental Prediction Research Facility under Program Element 62759N, Project 9F 52551792 "Atmospheric Environmental Support."		
19. KEY WORDS (Continue on reverse side if necessary and identify by block number) Aerosols Atmospheric Optical Properties Radiative Transfer Remote Sensing		
20. ABSTRACT (Continue on reverse side if necessary and identify by block number) An efficient modeling approach is described to simulate the dependence of remotely sensed radiances at visible and near infrared wavelengths (0.4-1.1 $\mu$ m) on meteorological variables such as relative humidity, wind speed, and visual range. Model elements include: (1) atmospheric opacity due to Rayleigh scattering and gaseous absorption, (2) physical modeling of aerosol size distribution, (3) aerosol optical properties calculations, and (4) implementation of radiative transfer theory. Sensitivity analyses are		

3927144

## 20 ABSTRACT (cont.)

performed for these variables in the context of examining modeled meteorological influences in the marine environment on the DMSP VHR and LF sensors. The sensitivity of emergent radiances in the near infrared spectral windows to the presence of relative humidity and wind speed dependent coarse mode aerosols of oceanic origin is demonstrated.

Accession For	
NTIS GRA&I	<input checked="" type="checkbox"/>
DTIC TAB	<input type="checkbox"/>
Unannounced	<input type="checkbox"/>
Justification	
By	
Distribution/	
Availability Codes	
Avail and/or	
Dist	Special

## TABLE OF CONTENTS

	Page
Abstract	4
1. Introduction	1-1
1.1 Background	1-1
1.2 Study Objectives	1-2
1.3 Summary of Report	1-4
2. Methodology	2-1
2.1 Overview	2-1
2.2 Technical Approach	2-5
3. Atmospheric (Non-Aerosol) Optical Properties	3-1
3.1 Rayleigh Scattering Optical Depth, $\tau_R^*$	3-1
3.2 Absorption Optical Depth, $\tau_g$	3-3
3.3 Total Non-Aerosol Optical Depth, $\tau_{na}$	3-9
4. Physical Models of Maritime Aerosols	4-1
4.1 Aerosol Size Distribution	4-1
4.2 Effect of Relative Humidity	4-10
4.3 Candidate Physical Models	4-16
5. Aerosol Optical Properties	5-1
5.1 Mie Theory Calculations	5-1
5.2 Meteorological Dependence of Aerosol Optical Properties	5-3
5.2.1 Maritime Model	5-3
5.2.2 Hybrid Model	5-4
5.3 Number Density/Visual Range Normalization	5-11
5.4 Aerosol Optical Depths, $\tau_i^{e,s}$	5-12



	Page
6. Radiative Transfer	6-1
6.1 Technique Selection Criteria	6-1
6.2 Analytical Approaches	6-2
6.3 Adopted Approach	6-6
6.4 Theory	6-7
6.5 Ensemble Atmospheric Optical Properties	6-18
6.6 DMSP Bandpass Weighted Radiances	6-19
7. Discussion of Results	7-1
7.1 Scope	7-1
7.2 Maritime Model - Geometry	7-1
7.3 Maritime Model - Surface Albedo	7-3
7.4 Maritime Model - Scale Height and Relative Humidity Dependence	7-4
7.5 Hybrid Model - Relative Humidity, Wind Speed, and Size Range Dependence	7-10
7.5.1 Hybrid Model - Accumulation Mode Only	7-10
7.5.2 Hybrid Model - Relative Humidity	7-13
7.5.3 Hybrid Model - Wind Speed	7-16
7.6 Visual Range	7-16
7.7 DMSP Bandpass-Weighted Radiances	7-19
7.7.1 Maritime Model	7-19
7.7.2 Hybrid Model	7-21
8. Summary of Results	8-1
9. Conclusions and Recommendations	9-1
9.1 Conclusions	9-1
9.2 Recommendations for Further Study	9-3
10. Acknowledgements	10-1
11. References	11-1
12. Appendix	12-1

## ABSTRACT

An efficient modeling approach is described to simulate the dependence of remotely sensed radiances at visible and near infrared wavelengths (0.4-1.1  $\mu\text{m}$ ) on meteorological variables such as relative humidity, wind speed, and visual range. Model elements include: (1) atmospheric opacity due to Rayleigh scattering and gaseous absorption, (2) physical modeling of aerosol size distribution, (3) aerosol optical properties calculations, and (4) implementation of radiative transfer theory. Sensitivity analyses are performed for these variables in the context of examining modeled meteorological influences in the marine environment on the DMSP VHR and LF sensors. The sensitivity of emergent radiances in the near infrared spectral windows to the presence of relative humidity and wind speed dependent coarse mode aerosols of oceanic origin is demonstrated.

## 1. INTRODUCTION

### 1.1 Background

Anomalous gray shade patterns appearing in DMSP (Defense Meteorological Satellite Program) visible VHR (Very High Resolution) and LF (Light Fine) imagery are variously attributable to low level haze and moisture, light fog, cirrus cloudiness, shallow or turbid water, ocean spray, and sun glint (Fett and Mitchell, 1977). In a recent study focusing on reduced visibility situations at sea (Barnes et al., 1978), DMSP and concurrent LANDSAT MSS (Multi-Spectral Scanner) data were examined to delineate the roles of aerosol and water vapor in producing anomalous gray shades. Although results of the imagery analysis were not conclusive, an accompanying theoretical study based on radiative transfer theory indicated that simulated satellite-based intensities are highly dependent on the atmosphere's aerosol loading (parameterized by the surface visual range) while the role of water vapor (varied over two orders of magnitude) was relatively insignificant. In conducting this preliminary analysis, however, a number of approximations and simplifying assumptions were adopted including: (a) choice of a specific aerosol model, (b) neglecting the coupling between relative humidity and aerosol growth, (c) assuming that the aerosol scattered light isotropically (independent of direction), and (d) neglecting the influence of other meteorological factors such as wind speed on the aerosol size distribution.

In a subsequent study relaxing a number of these assumptions (Fett and Isaacs, 1979), the sensitivity of DMSP VHR and LF sensors in delineating regions of optically thin maritime haze was demonstrated for a specific case. The accompanying analysis suggested that this sensitivity is a result of the system's broad spectral response extending into and peaking at near infrared (NIR) wavelengths. Furthermore, the calculation presented suggested specifically that a number of factors related to optical properties of maritime hazes including scattering anisotropy and wavelength dependent extinction are responsible for the apparent capability of broadband sensors to "see" low level haze while exclusively visible sensors cannot.

## 1.2 Study Objectives

Since low level haze situations with reduced visibility have potential adverse impact on a variety of Naval electro-optical systems, these preliminary findings suggested a requirement to further investigate the capabilities of DMSP imagery to delineate such cases. The study described in this document was undertaken to extend the investigation of the phenomena described above and to examine relevant factors neglected in the previous work. The primary objectives of this research effort were to:

- (1) Implement a physically realistic maritime haze model including altitude variations of relevant size ranges and the dynamic response of aerosol

size distribution and complex index of refraction to meteorological variables such as:

- . wind speed
- . relative humidity.

- (2) Evaluate the wavelength dependent optical properties of the model maritime haze for implementation in the radiative transfer calculations to follow.

These optical properties include:

- . extinction and scattering coefficients
- . single scattering albedo
- . phase function.

- (3) Adopt an appropriate radiative transfer technique capable of treating the mechanisms of:

- . multiple scattering
- . near infrared water vapor absorption
- . surface reflection
- . scattering anisotropy of the maritime haze model
- . sun/sensor geometry effects.

- (4) Compute wavelength and meteorologically dependent emergent intensities in the spectral region from 0.4 to 1.1  $\mu\text{m}$  based on the previous modeling efforts and simulate the response of the DMSP VHR and LF sensors to variations in meteorological variables by appropriately weighting results using the DMSP sensor response function.

- (5) Investigate the sensitivity of the DMSP visible/NIR sensors to a variety of representative meteorological conditions and subsequently examine the feasibility of developing user-oriented operational nomographs based on these results.

For the most part, these objectives have been satisfied.

### 1.3 Summary of Report

This document is organized into nine sections. Section 2 describes the methodology employed to accomplish the objectives cited above as well as an overview of this research effort from the perspective of existing optical propagation models. Sections 3 through 6 discuss technical implementation of the adopted methodology. Section 3 reviews the calculation of non-aerosol atmospheric optical properties. Section 4 discusses modeling the physical properties of maritime aerosols, while Section 5 includes a description of the calculations required to transform from aerosol physical to aerosol optical properties. Section 6 provides the theoretical basis for the adopted radiative transfer treatment. Results are presented and discussed in Section 7. A summary of results is given in Section 8. Finally, Section 9 includes relevant conclusions and recommendations.

## 2. METHODOLOGY

### 2.1 Overview

A variety of mathematical models are currently available to assess the influence of meteorological variables on in situ, point-to-point atmospheric transmission which may constrain the operational effectiveness of proposed or deployed electro-optical systems. These codes include the atmospheric transmittance algorithms developed at the Air Force Geophysics Laboratories (LOWTRAN 2, Selby and McClatchey, 1972; LOWTRAN 3, Selby and McClatchey, 1973; LOWTRAN 3B, Selby et al., 1976; LOWTRAN 4, Selby et al., 1978; HITRAN, McClatchey et al., 1973; Rothman and McClatchey, 1976; LASER, McClatchey and D'Agati, 1978), the optical parameter models (OPM) adopted by the Naval Surface Weapons Center (NSWC) (Wells et al., 1977; Hughes and Richter, 1979), and various battlefield scenario models developed by the Army (e.g., Gomez and Duncan, 1978). As described in the previous section, this investigation has focused on the development of computational algorithms to simulate the parametric response of remotely-sensed, wavelength-dependent radiances ( $\text{mW cm}^{-2} \mu\text{m}^{-1} \text{sr}^{-1}$ ) to representative variations in meteorological variables. An essential step in the adopted simulation methodology is the evaluation of meteorologically-dependent atmospheric optical properties facilitated by the application of the propagation codes cited above. This information is required to perform radiative transfer calculations to obtain

satellite-incident radiances. In a fundamental sense, therefore, the models developed in the course of this investigation are an extension of extant surface propagation models and may provide a potentially informative link between available in situ and remotely-sensed data sets.

The results reported here are confined to an examination of meteorological influences on remotely-sensed radiances within the DMSP VHR and LF sensor bandpass illustrated in Figure 1 (Fett and Mitchell, 1977). This spectral region encompasses both visible (0.4 to .7  $\mu\text{m}$ ) and near infrared (NIR) (.7-1.1  $\mu\text{m}$ ) wavelengths which arise due to backscattering of incident solar radiation from the atmosphere and reflection from the atmosphere and the earth's surface. The meteorological variables treated and their respective domains are given in Table 1. It should be noted that number density (c) and visual range (d) are not independent variables. In practice, when visual range appears as a parameter, it has been used to compute an equivalent number density (see §5.3). Furthermore, the radiative transfer methods adopted depend on the product of number density and scale height [i.e., a column density ( $\text{cm}^{-2}$ )], not independently on each. Therefore, increases in scale height may be interpreted as changes in number density where appropriate (see §5.4). Subsequent discussion will clarify these points.



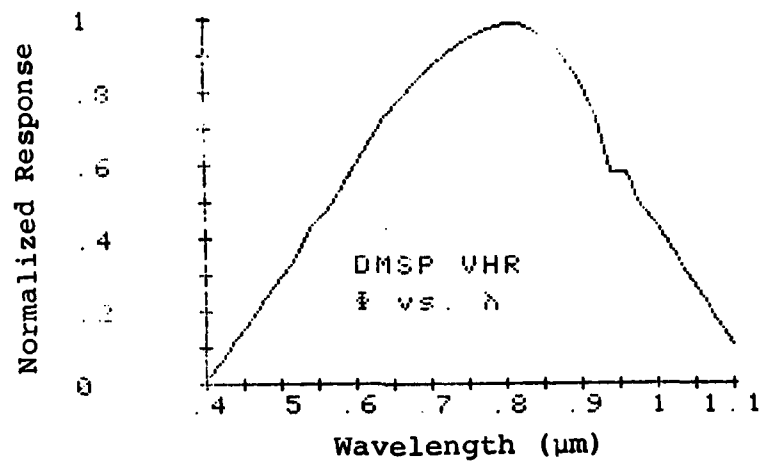


Figure 1  
DMSP Spectral Bandpass  
(Fett and Mitchell, 1977)

Table 1  
Meteorological Variables and  
Their Representative Domains

Variable	Domain
(a) Relative Humidity (%) RH	50, 70, 80, 90, 95
(b) Wind Speed ( $\text{ms}^{-1}$ ) WS	0, 5, 7, 10
(c) Number Density ( $\text{cm}^{-3}$ ) N	4000, 5000 (see text)
(d) Visual Range (km) $V_r$	5, 10, 23, 50
(e) Aerosol Scale Height (km) H	0.5, 1.0, 1.5, 2.0

## 2.2 Technical Approach

The general approach adopted in this investigation is summarized in Figure 2. Requisite input parameters include the meteorological variables: relative humidity (RH), wind speed (WS), number density (N) or visual range ( $V_r$ ), and aerosol scale heights (H)<sup>†</sup> and the geometric configuration of the sun/atmosphere-ocean/sensor system as determined from the solar zenith angle, sensor angle, and azimuth angle difference. Operationally, these geometric parameters vary spatially for individual resolution elements within a particular sensor's field-of-view and temporally due to sensor attitude drift. They are available, however, from standard spacecraft ephemeris data. For the purpose of these sensitivity studies, a nadir viewing sensor (sensor zenith angle, 0.0°) and a solar zenith angle of 60° were assumed. This provides a configuration with a scattering angle of 120° which is between those of the DMSP, NOAA5 and SMS spacecraft as described in Fett and Isaacs (1979). The results obtained for each set of input parameters are an intensity (or radiance) spectrum for wavelengths between 0.4 and 1.1  $\mu\text{m}$ ,  $I(\lambda)$ , and a DMSP VHR response function weighted radiance,  $\bar{I}(\text{DMSP})$ .

The processes linking input parameters and desired output as illustrated in Figure 2 may be divided into four basic modeling efforts: (a) atmospheric transmission (i.e., exclusive of aerosols), (b) physical modeling of aerosol properties

---

<sup>†</sup> Depending on the aerosol model adopted, individual scale heights H1 and H2 may be assigned to individual aerosol size ranges.

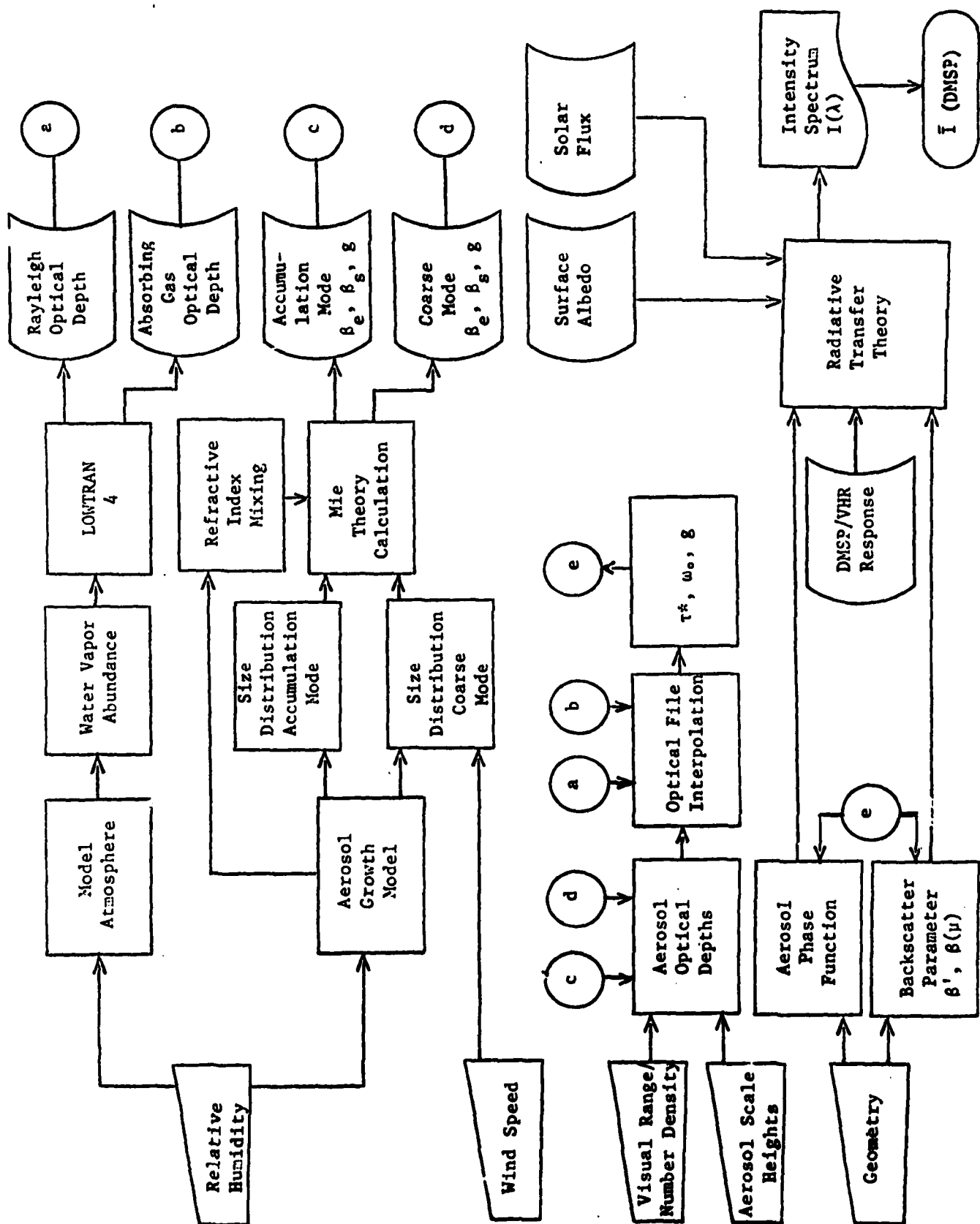


**Figure 2**  
**Technical Approach**

including relative humidity and wind speed dependence of aerosol size distribution and index of refraction, (c) determination of wavelength-dependent aerosol optical properties, and finally (d) radiative transfer theory. To a great extent, typical propagation models (§2.1) include elements (a), (b), and (c). Implementation of some form of radiative transfer code is required to evaluate radiances multiply-backscattered to a satellite sensor. In the formalism adopted, the radiative transfer theory is dependent (at each wavelength) on three variables which characterize the ensemble properties of the atmosphere's optically active gaseous and particulate constituent species. These are: (1) the total optical depth,  $\tau^*$ , (2) the single scattering albedo,  $\omega_0$ , and (3) the scattering phase function asymmetry parameter,  $g$ . These three dimensionless variables are determined from the wavelength-dependent optical properties of individual atmospheric constituents including: (a) scattering by molecules (i.e., Rayleigh scattering), (b) absorption by molecules (such as water vapor and ozone), and (c) scattering and absorption by aerosols. Atmospheric optical properties are, in turn, dependent on meteorological variables as illustrated in Figure 2. Relative humidity fixes both the abundance of water vapor in the atmosphere (assuming a model temperature profile) thereby controlling water vapor absorption where applicable (such as in the NIR water vapor bands) and the rate of aerosol growth which modifies aerosol size distribution and prescribes the appropriate aerosol index of refraction. Wind speed determines the rate of mechanical addition of coarse mode ( $r > 1.0 \mu\text{m}$ )

fugitive sea spray which in turn modifies size distribution.

A detailed discussion of the elements of the technical approach presented above follows in Sections 3 through 6.

### 3. ATMOSPHERIC (NON-AEROSOL) OPTICAL PROPERTIES

In the absence of aerosols, atmospheric optical properties in the 0.4-1.1  $\mu\text{m}$  spectral region are determined by molecular (Rayleigh) scattering and absorption by gases such as water vapor and ozone. Both the normal optical depth due to Rayleigh scattering,  $\tau_R^s$ , and that due to absorption by atmospheric gases,  $\tau_g$ , have been evaluated in this effort using a modified version of computer code LOWTRAN 4 (Selby et al., 1978). The model atmosphere chosen for this purpose is the tropical model given in Table 2.

#### 3.1 Rayleigh Scattering Optical Depth, $\tau_R^s$

The Rayleigh scattering optical depth,  $\tau_R^s$ , is obtained by integrating the Rayleigh scattering coefficient,  $\beta_R^s$ , throughout the atmosphere:

$$\tau_R^s(\lambda) = \int \beta_R^s(\lambda, z) dz \quad (1)$$

where (Penndorf, 1957):

$$\beta_R^s(\lambda) [\text{km}^{-1}] = \frac{8\pi^3}{3} \frac{(m^2 - 1)^2}{\lambda^4} \frac{1.061 \times 10^{21}}{n} \quad (2)$$

and  $m$  is the index of refraction of air (dependent on pressure, temperature, and wavelength)

$n(\text{cm}^{-3})$  is the local number density of air (dependent on pressure and temperature)

and  $\lambda(\mu\text{m})$  is the wavelength required.

Table 2

MODEL ATMOSPHERE USED AS A BASIS OF THE COMPUTATION OF  
ATMOSPHERIC OPTICAL PROPERTIES

TROPICAL					
Alt. (km)	Pressure (mb)	Temp. (°K)	Density (g/m <sup>3</sup> )	Water Vapor (g/m <sup>3</sup> )	Ozone (g/m <sup>3</sup> )
0	1.013E+03	300.0	1.167E+03	1.9E+01	5.6E-05
1	9.040E+02	294.0	1.064E+03	1.3E+01	5.6E-05
2	8.050E+02	288.0	9.689E+02	9.3E+00	5.4E-05
3	7.150E+02	284.0	8.756E+02	4.7E+00	5.1E-05
4	6.330E+02	277.0	7.951E+02	2.2E+00	4.7E-05
5	5.590E+02	270.0	7.199E+02	1.5E+00	4.5E-05
6	4.920E+02	264.0	6.501E+02	8.5E-01	4.3E-05
7	4.320E+02	257.0	5.855E+02	4.7E-01	4.1E-05
8	3.780E+02	250.0	5.258E+02	2.5E-01	3.9E-05
9	3.290E+02	244.0	4.708E+02	1.2E-01	3.9E-05
10	2.860E+02	237.0	4.202E+02	5.0E-02	3.9E-05
11	2.470E+02	230.0	3.740E+02	1.7E-02	4.1E-05
12	2.130E+02	224.0	3.316E+02	6.0E-03	4.3E-05
13	1.820E+02	217.0	2.929E+02	1.8E-03	4.5E-05
14	1.560E+02	210.0	2.578E+02	1.0E-03	4.5E-05
15	1.320E+02	204.0	2.260E+02	7.6E-04	4.7E-05
16	1.110E+02	197.0	1.972E+02	6.4E-04	4.7E-05
17	9.370E+01	195.0	1.676E+02	5.6E-04	6.9E-05
18	7.890E+01	199.0	1.382E+02	5.0E-04	9.0E-05
19	6.660E+01	203.0	1.145E+02	4.9E-04	1.4E-04
20	5.650E+01	207.0	9.515E+01	4.5E-04	1.9E-04
21	4.800E+01	211.0	7.938E+01	5.1E-04	2.4E-04
22	4.090E+01	215.0	6.645E+01	5.1E-04	2.8E-04
23	3.500E+01	217.0	5.618E+01	5.4E-04	3.2E-04
24	3.000E+01	219.0	4.763E+01	6.0E-04	3.4E-04
25	2.570E+01	221.0	4.045E+01	6.7E-04	3.4E-04
30	1.220E+01	232.0	1.831E+01	3.6E-04	2.4E-04
35	6.000E+00	243.0	8.600E+00	1.1E-04	9.2E-05
40	3.050E+00	254.0	4.181E+00	4.3E-05	4.1E-05
45	1.590E+00	265.0	2.097E+00	1.9E-05	1.3E-05
50	8.540E-01	270.0	1.101E+00	6.3E-06	4.3E-06
70	5.790E-02	219.0	9.210E-02	1.4E-07	8.6E-08
100	3.000E-04	210.0	5.000E-04	1.0E-09	4.3E-11

Source: Selby and McClatchey (1972)



In practice, the wavelength dependence of the index of refraction may be incorporated into a simplified expression for  $\beta_R^S(\lambda)$  appropriate for standard temperature and pressure conditions:

$$\beta_R^S(\lambda) [\text{km}^{-1}] = 1.0923 \times 10^{-3} \lambda^{-4.0117} \quad (3)$$

and equation (1) approximated as:

$$\tau_R^S(\lambda) = \beta_R^S(\lambda) H_R \quad (4)$$

where  $H_R$  (km) is the equivalent scale height for Rayleigh scattering. For the tropical atmospheric model in Table 2, this scale height equals 8.05 km.

### 3.2 Absorption Optical Depth, $\tau_g$

Figure 3 illustrates the effect of absorption by atmospheric gases on incident solar radiation in the 0.4-1.1  $\mu\text{m}$  spectral region. Absorbing species include ozone,  $\text{O}_3$ , oxygen,  $\text{O}_2$ , and water vapor,  $\text{H}_2\text{O}$ .

The Chappuis bands of ozone lie between 0.45 and 0.74  $\mu\text{m}$  in the visible spectrum. The maximum absorption cross-section for these bands (at about 0.60  $\mu\text{m}$ ) is  $5 \times 10^{-21} \text{ cm}^2$  yielding an optical depth of about .05 (or a transmission of .95) for a typical ozone column abundance of  $10^{19} \text{ cm}^{-2}$  (Goody, 1964). Their effect on remote sensing is, therefore, quite small. The solar "red" bands of oxygen at .688 and .762  $\mu\text{m}$  are relatively strong features, however, since the oxygen abundance is

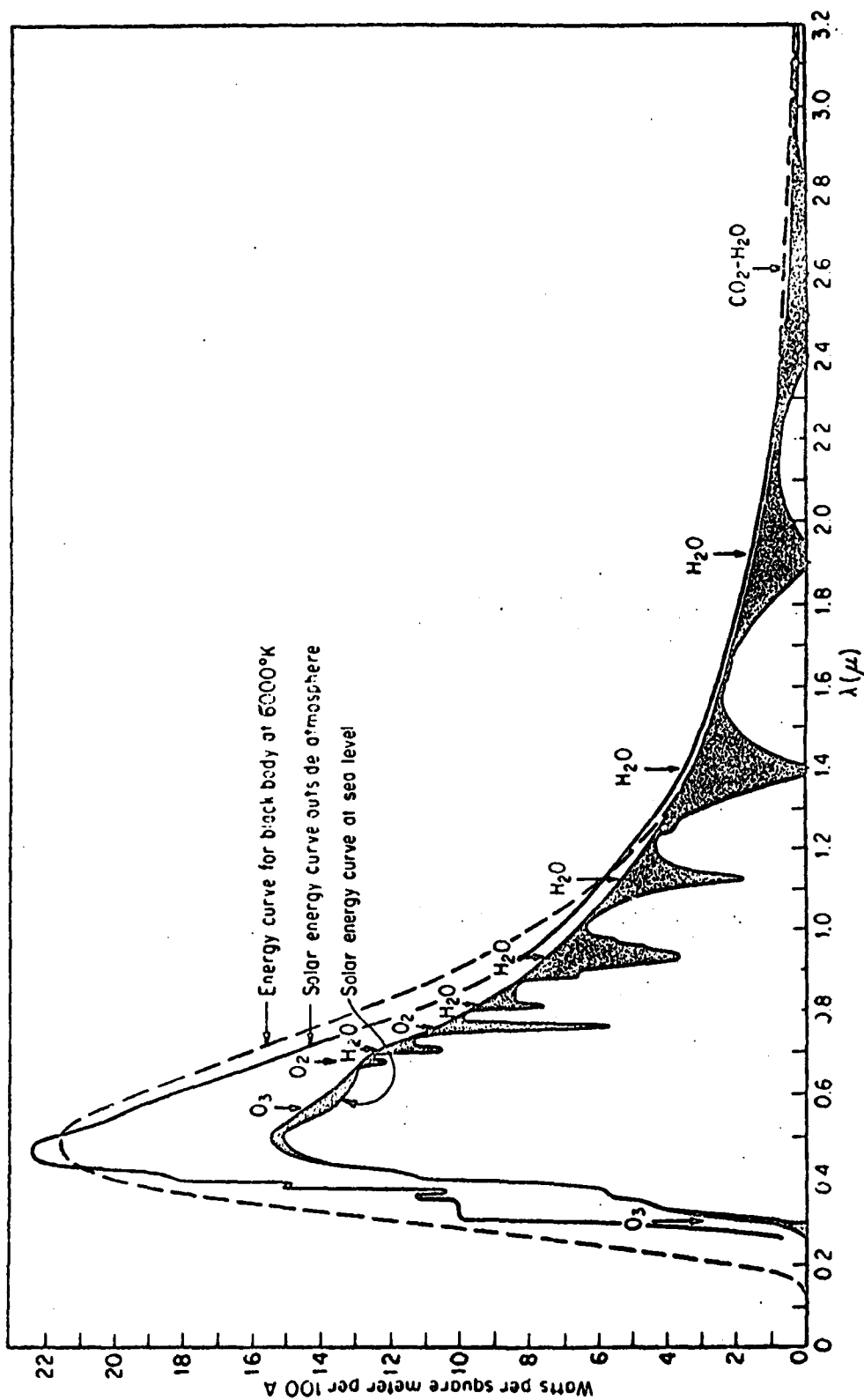


Figure 3

Spectral energy curve of solar radiation at sea level and extrapolated outside the atmosphere, as given by Pettit (1951). The darkened areas represent gaseous absorption in the atmosphere.

constant in the model atmosphere (as is ozone) they do not vary meteorologically. The most prominent gaseous absorber within the spectral region of interest is water vapor. Both visible and NIR bands appear with varying strengths. Some of the qualitative features of Figure 3 can be delineated using Table 3, which gives the quantum mechanical transition, band center, and strength of the water vapor bands (Goody, 1964; McClatchey et al., 1973). (The strength is defined as the integral over the band of the absorption cross-section.) Bands that are identifiable in Figure 3 are marked with an asterisk. Note that all bands are ground-state transitions (initial state 000), and although those in the visible ( $< 0.70 \mu\text{m}$ ) are relatively weak, the near-infrared bands ( $\rho$ ,  $\sigma$ ,  $\tau$ ,  $\phi$ ) are rather strong.

In order to simulate the effect of variations in relative humidity on the optical depth due to water vapor absorption, the climatological water vapor abundance profile in the adopted model atmosphere (Table 2) is replaced in the lowest few kilometers by a constant relative humidity water vapor abundance profile given by:

$$\rho(z, \text{RH}) = \frac{13.238 \text{ RH}}{T(z)} \exp\left[19.85\left(1 - \frac{273.16}{T(z)}\right)\right] \quad (5)$$

where RH is the desired relative humidity expressed in percent and  $T(z)$  is the temperature profile from Table 2. Figure 4 compares the water vapor abundance profiles for the climatologically based LOWTRAN 4 tropical atmosphere and the constant

Table 3

VISIBLE AND NEAR INFRARED WATER VAPOR BANDS

Transition	Band Center ( $\mu\text{m}$ )	Strength ( $\text{cm}$ )
000-411	0.544	$2 \times 10^{-23}$
000-203	0.572	$1 \times 10^{-22}$
000-401	0.592	$3 \times 10^{-22}$
000-302	0.592	$3 \times 10^{-23}$
000-321	0.594	$2 \times 10^{-22}$
000-113	0.632	$2 \times 10^{-23}$
000-311	0.652	$2 \times 10^{-22}$
000-103	0.698	$1 \times 10^{-21*}$
000-400	0.703	$1 \times 10^{-22}$
000-301	0.723	$3 \times 10^{-21*}$
000-202	0.723	$< 2 \times 10^{-23}$
000-221	0.734	$6 \times 10^{-21*}$
000-013	0.796	$1 \times 10^{-22}$
000-112	0.806	$6 \times 10^{-21*}$
000-211	0.823	$6 \times 10^{-23*}$
000-210	0.824	$1 \times 10^{-22*}$
000-131	0.847	$2 \times 10^{-21*}$
$\rho$ 000-003	0.906	$2 \times 10^{-21*}$
000-102	0.920	$4 \times 10^{-22*}$
$\sigma$ 000-201	0.942	$1 \times 10^{-20*}$
000-300	0.943	$6 \times 10^{-22*}$
$\tau$ 000-121	0.968	$2 \times 10^{-21*}$
000-220	0.972	$< 4 \times 10^{-23}$
000-041	1.016	$4.8 \times 10^{-23}$
$\phi$ 000-012	1.111	$1.2 \times 10^{-21}$
000-121	1.135	$5 \times 10^{-20}$

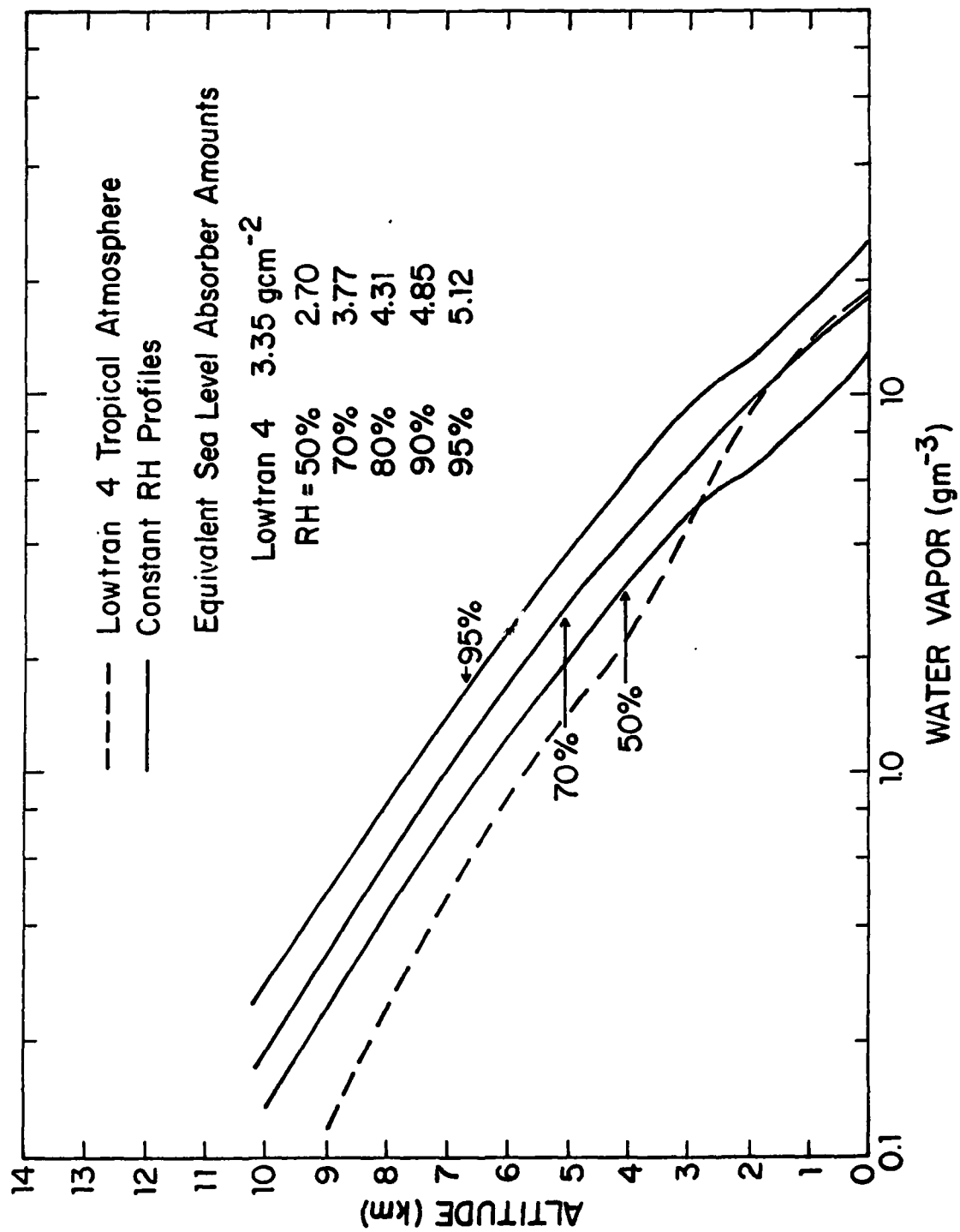


Figure 4

relative humidity profiles adopted in this work.

Constant relative humidity profiles are used in order to maintain consistency between the specification and treatment of optical properties for water vapor absorption and those for aerosol extinction. The subsequently applied radiative transfer algorithm is a one layer model requiring uniform optical properties. Although, in a well-mixed boundary layer water vapor mass mixing ratio may tend to be constant with height rather than relative humidity, this would imply a relative humidity gradient given a representative temperature profile. Since this would require a gradient of aerosol optical properties, constant relative humidity profiles are utilized.

Evaluation of wavelength-dependent gaseous absorption optical depths was accomplished by evaluating transmittances,  $T_g(\lambda, RH)$ , for a vertical path to space using an aerosol-free LOWTRAN 4 atmosphere modified for constant relative humidity as described above and performing the operation:

$$\tau_g(\lambda, RH) = -\ln[T_g(\lambda, RH)] \quad . \quad (6)$$

Although equation (6) is not strictly valid for band models (i.e., where the Beer-Lambert Law does not hold), more sophisticated treatments were deemed inappropriate and inconsistent with the radiative transfer treatment adopted.

### 3.3 Total Non-Aerosol Optical Depths

The total non-aerosol optical depth,  $\tau_{na}$ , given by:

$$\tau_{na}(\lambda, RH) = \tau_R^S(\lambda) + \tau_g(\lambda, RH) \quad (7)$$

was evaluated for the wavelength region 0.4-1.1  $\mu\text{m}$  and for relative humidities of 50, 70, 80, 90 and 95% using the techniques described above. As illustrated in Figure 2, the Rayleigh optical depth (a) and absorbing gas optical depth (b) are fundamental intermediate variables in the subsequent radiative transfer calculation. Figure 5 illustrates the variation of total non-aerosol optical depth with wavelength and relative humidity. It is notable that at visible wavelengths ( $\lambda < 0.7 \mu\text{m}$ ), non-aerosol optical depth is independent of relative humidity and follows the approximate  $\lambda^{-4}$  Rayleigh scattering law given by equations (3) and (4). A barely perceptible increase in optical depth in the vicinity of 0.6  $\mu\text{m}$  is due to the weak Chappuis band ozone absorption previously mentioned. At near infrared wavelengths ( $\lambda > 0.7 \mu\text{m}$ ), however, non-aerosol optical depth is dominated by water vapor absorption in bands identifiable by reference to Table 3. The magnitude of optical depth near the centers of these bands is highly dependent on relative humidity. In the regions approximately between bands (0.75-0.80, 0.85-0.90, 1.0-1.08  $\mu\text{m}$ ), Rayleigh scattering is negligible and non-aerosol optical thickness is near zero.

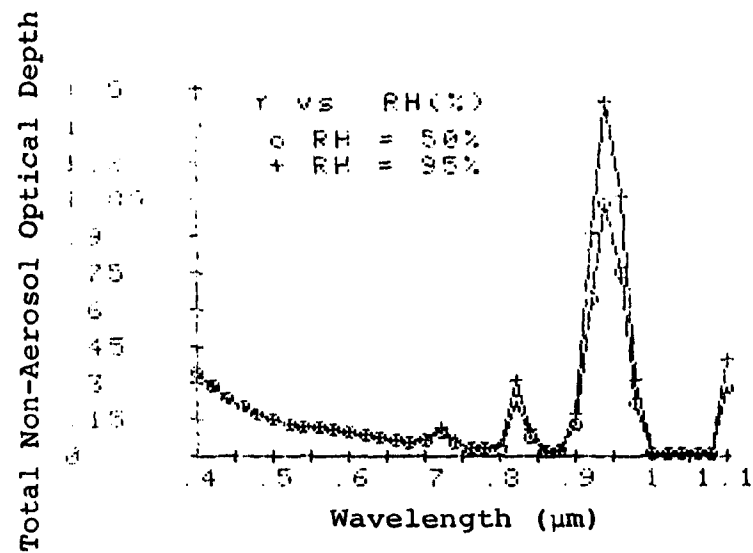


Figure 5

Modified LOWTRAN 4 Based Total Non-Aerosol  
Optical Depth ( $\tau_R^s + \tau_g$ ) for Two Relative Humidities



#### 4. PHYSICAL MODELS OF MARITIME AEROSOLS

The nature of the remote sensing and optical transmission problem in the atmosphere-ocean system is extensively modified by the presence of marine aerosols. These pervasive particulates represent a challenging problem to radiative transfer modelers, due to their inherent spatial and temporal variability and the apparent dependence of their physical properties on meteorological variables such as relative humidity and near-surface wind speed. Reference to Figure 2, indicates that aerosol optical properties (determined by Mie theory calculations) are dependent on the physical properties of the aerosol including size distribution and refractive index.

In this section, the physical mechanisms determining the relationship between meteorological variables and aerosol physical properties are elucidated and the specific physical models adopted in this work are described.

##### 4.1 Aerosol Size Distribution

The fundamental link between meteorological variables and marine aerosol optical properties is the marine aerosol size distribution,  $n(r)$  [units  $\text{cm}^{-3}\mu\text{m}^{-1}$ ]. The size distribution expresses the number density of aerosol "droplets" of radius  $r$  within a size range from  $r$  to  $(r+dr)$ . Thus, the total number density of aerosol droplets in all size ranges is:

$$N (\text{cm}^{-3}) = \int_0^{\infty} n(r) dr \quad (8)$$

Extensive measurements have indicated that the aerosol number density distribution with size range,  $n(r)$  can be reproduced by a mathematical model which assumes a finite number of modes or size ranges (Whitby and Sverdrup, 1978), generally three, consisting of, in order of increasing radius: (a) Aitkin nuclei, (b) an accumulation mode (mass median radius 0.1 to 1.0  $\mu\text{m}$ ), and (c) a coarse mode (mass median radius greater than 1.0  $\mu\text{m}$ ). Since the effect of Aitkin nuclei on optical properties in the 0.4 to 1.1  $\mu\text{m}$  range is negligible (Nilsson, 1979), they are not treated in subsequent discussions. It is generally convenient to describe each of the two remaining modes by a tractable analytical expression. This is particularly advantageous when size-fractionated, compositional data suggest [as in the case of maritime aerosol over remote oceanic regions (Meszaros and Vissy, 1974)] that the accumulation mode and coarse mode have distinct source mechanisms and compositions.

Although many functional forms have been assumed in the past, including Junge (1963; 1972) and Deirmendjian (1969) distributions, a particularly convenient representation is the log-normal size distribution (Dennis, 1976):

$$n(r) = N [\exp(-\ln^2 r/r_n / 2 \ln^2 \sigma)] / r \sqrt{2\pi} \ln \sigma \quad (9)$$

with number median radius  $r_n$  and standard deviation  $\sigma$ . The total number density of particles is normalized to  $N$  ( $\text{cm}^{-3}$ ). On a log probability plot, the number median is that value with 50% of the distributions number density above and below.

The distribution is often given in terms of the mass or volume median radius  $r_m$  related to the number median radius through the standard deviation by:

$$\ln 2r_m = \ln 2r_n + 3.0 \ln^2 \sigma. \quad (10)$$

The maritime aerosol optical properties model adopted by the Air Force (Shettle and Fenn, 1976; 1979) and implemented within their standard atmospheric transmission codes (Selby et al., 1978) are formulated based on the number mean radii and standard deviations [with reference to equation (9) above] shown in Table 4. One advantage of this bimodal log-normal presentation is its applicability to incorporation within optical parameter evaluation models which include the effects of relative humidity on aerosol growth (Nilsson, 1979; Shettle and Fenn, 1979). The gross effect of a positive (negative) change in relative humidity on an aerosol size distribution initially in equilibrium with its environment is an increase (decrease) in the average size of the aerosol droplets within the distribution. The magnitude of the size change is dependent on the initial size and composition of the aerosol. The bimodal log normal representation permits the number median radius for each mode to be suitably modified for aerosol growth while keeping the total number of particles (mode number density) constant.

This allows for investigation of variation in optical properties with changes in relative humidity assuming that

aerosol production and loss mechanisms remain constant. For example, Table 5 presents relative humidity dependent number median radii for the bimodal maritime model described in Table 4. The specific rate of growth with changes relative humidity depends on the aerosol growth law adopted (see Section 4.3) for each mode.

For example, Table 5 suggests that the increase in median size between 50 and 95% relative humidities is a factor of about 1.75 greater in the coarse mode than in the accumulation mode. The relative humidity dependent size distributions given by the parameters in Table 5 using the log normal size distribution [equation (9)] are illustrated in Figure 6. (accumulation mode<sup>†</sup>) and Figure 7 (maritime model-both modes), respectively, assuming constant standard deviations (as given in Table 4) for each mode. One disadvantage of the size distribution models cited above with respect to the present study, is the neglect of the dynamic response of the sea spray produced component of the maritime aerosol (i.e. the coarse mode) to variations in prevailing wind speed. Measurements suggest that the number density of sea spray produced aerosol droplets increases with increased wind speed, especially the larger particles (Junge, 1960).

---

<sup>†</sup>The maritime model accumulation mode properties are equivalent to those of the tropospheric model in Shettle and Fenn 1979.

	Size Distribution Parameters (log normal)			
Aerosol Model	$N(\text{cm}^{-3})$	$r_n(\mu\text{m})$	$\sigma$	Type
<u>Maritime</u>				
Continental Origin (accumulation mode)	1.0	.03	2.24	Rural Aerosol Mixture (water soluble Aerosols)
Marine Origin (coarse mode)	1.0	0.3	2.51	Sea Salt Solution

Table 4. Parameters of maritime aerosol size distributions used in AFGL LOWTRAN models (Shettle and Fenn, 1979).

Relative Humidity %	Number Mode Radius ( $\mu\text{m}$ )	
	Accumulation ( $\sigma = 2.24$ )	Coarse ( $\sigma = 2.51$ )
50	.02748	.1711
70	.02846	.2041
80	.03274	.3180
90	.03884	.3853
95	.04238	.4606

Table 5. Humidity Dependent Mode Radii Maritime Model (Shettle and Fenn, 1979).

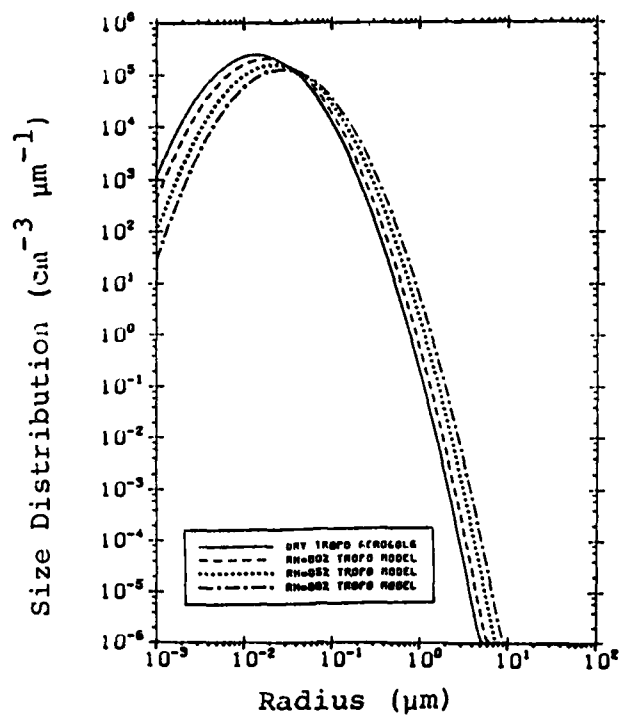


Figure 6

Maritime Model (accumulation mode only)  
[from Shettle and Fenn, 1979]

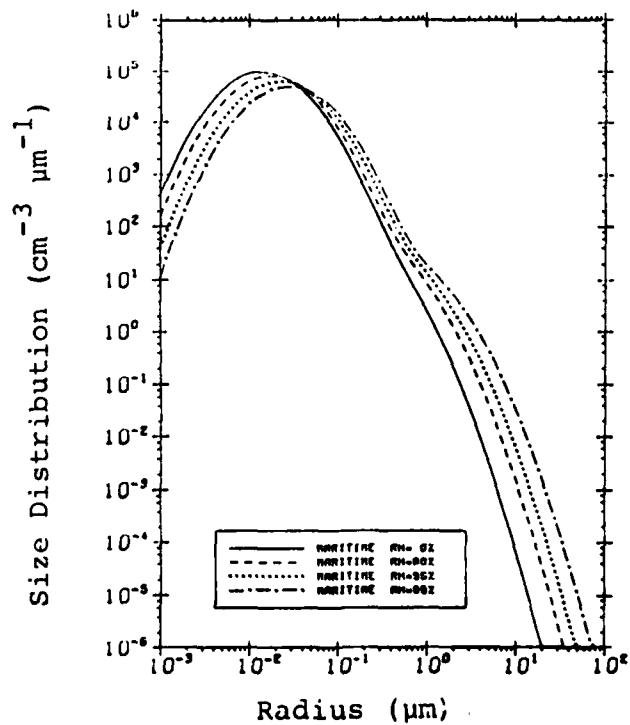


Figure 7

Maritime Model (accumulation and coarse modes)  
[from Shettle and Fenn, 1979]

An alternative size distribution model incorporating this dependence adopted by the Naval Surface Weapons Center (NSWC) utilizes a linear combination of Junge and Deirmendjian (or modified  $\Gamma$ ) distributions for the accumulation and coarse modes, respectively. Based, in part, on an earlier model by Wells et al. (1977) and modified by Katz, the size distribution for the Munn-Katz model is given by:

$$n(r) = 1.7\left(\frac{r}{\alpha}\right)^{-4} + 1.62(C_1 + C_2 V^\delta) \exp\left[\frac{-Z}{h_0 F} - 8.5\left(\frac{r}{\alpha}\right)^\Gamma\right] F^{-1}\left(\frac{r}{\alpha}\right), \quad (11)$$

where  $n(r)$  = number of particles per  $\text{cm}^3$  per  $\mu\text{m}$  (radius)

$r$  = radius ( $\mu\text{m}$ )

$Z$  = altitude (m)

$h_0$  = scale height set at 800 m for  $Z < 1$  km

$\alpha = 0.81 \exp\left[\frac{.066S}{1.058-S}\right]$

$S$  = saturation ratio (relative humidity  $\div$  100)

$V$  = wind factor scaled with surface wind  $V_0$

= .5 m/s for  $0 \leq V_0 \leq 4$  m/s

=  $(V_0 - 3.5)$  m/s for  $V_0 > 4$  m/s

$F = 1 + \left(\frac{V}{60}\right)^3$

$\Gamma = 0.384 - .00293V^{1.25}$

when  $V \leq 7$  m/s,  $C_1 = 350$ ,  $C_2 = 10^3$ ,  $\delta = 1.15$

$V > 7$  m/s,  $C_1 = 0$ ,  $C_2 = 6900$ ,  $\delta = 0.29$

In this model, the coarse mode aerosol [second term in (11)] is dependent on prevailing wind speed, due to contributions of fugitive sea spray components to this size range. This dependence follows the data of Woodcock (1953). Figures 8

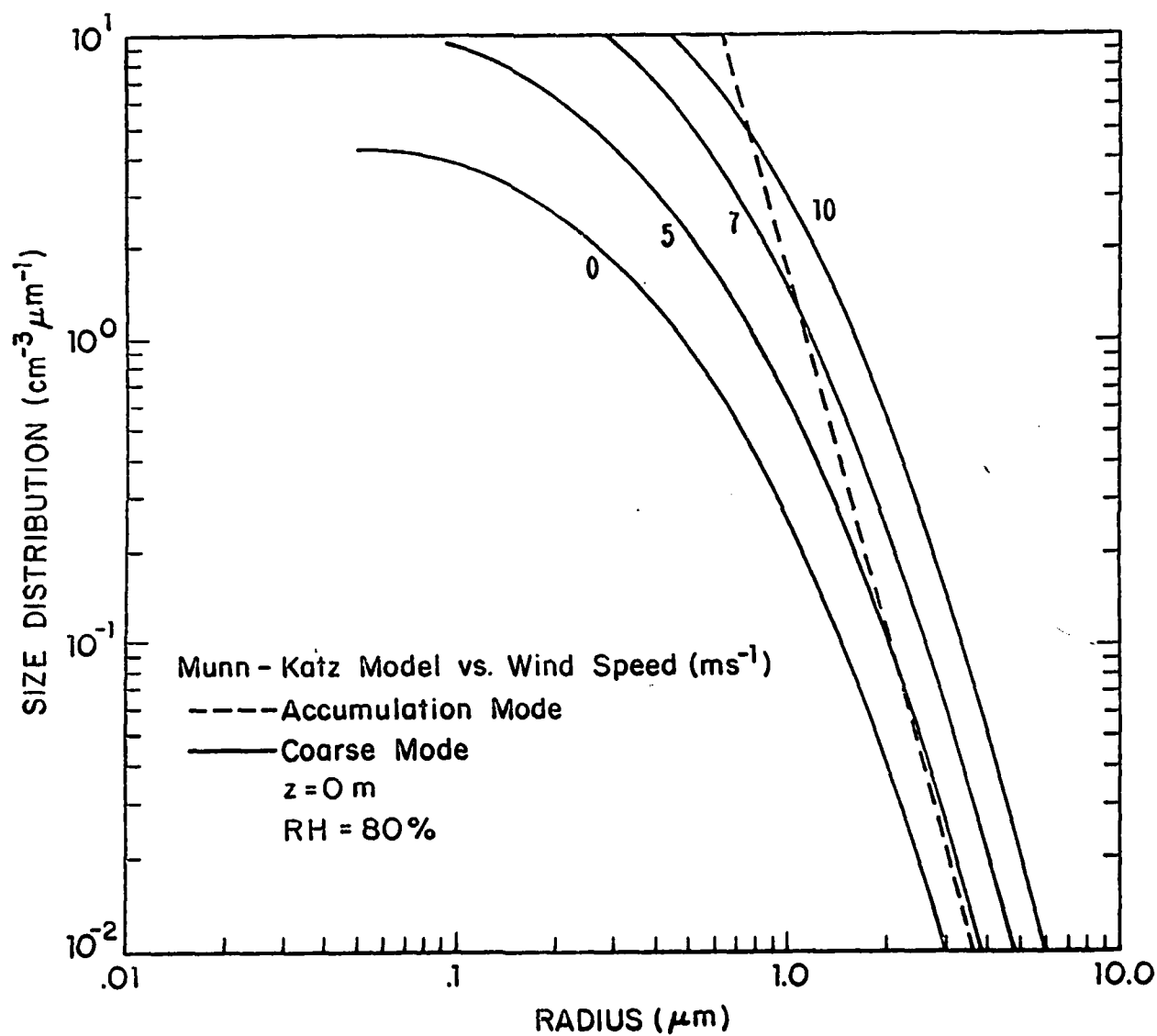


Figure 8  
Dependence of NSW model size distribution  
on wind speed ( $z = 0 \text{ m}$ ,  $\text{RH} = 80\%$ )



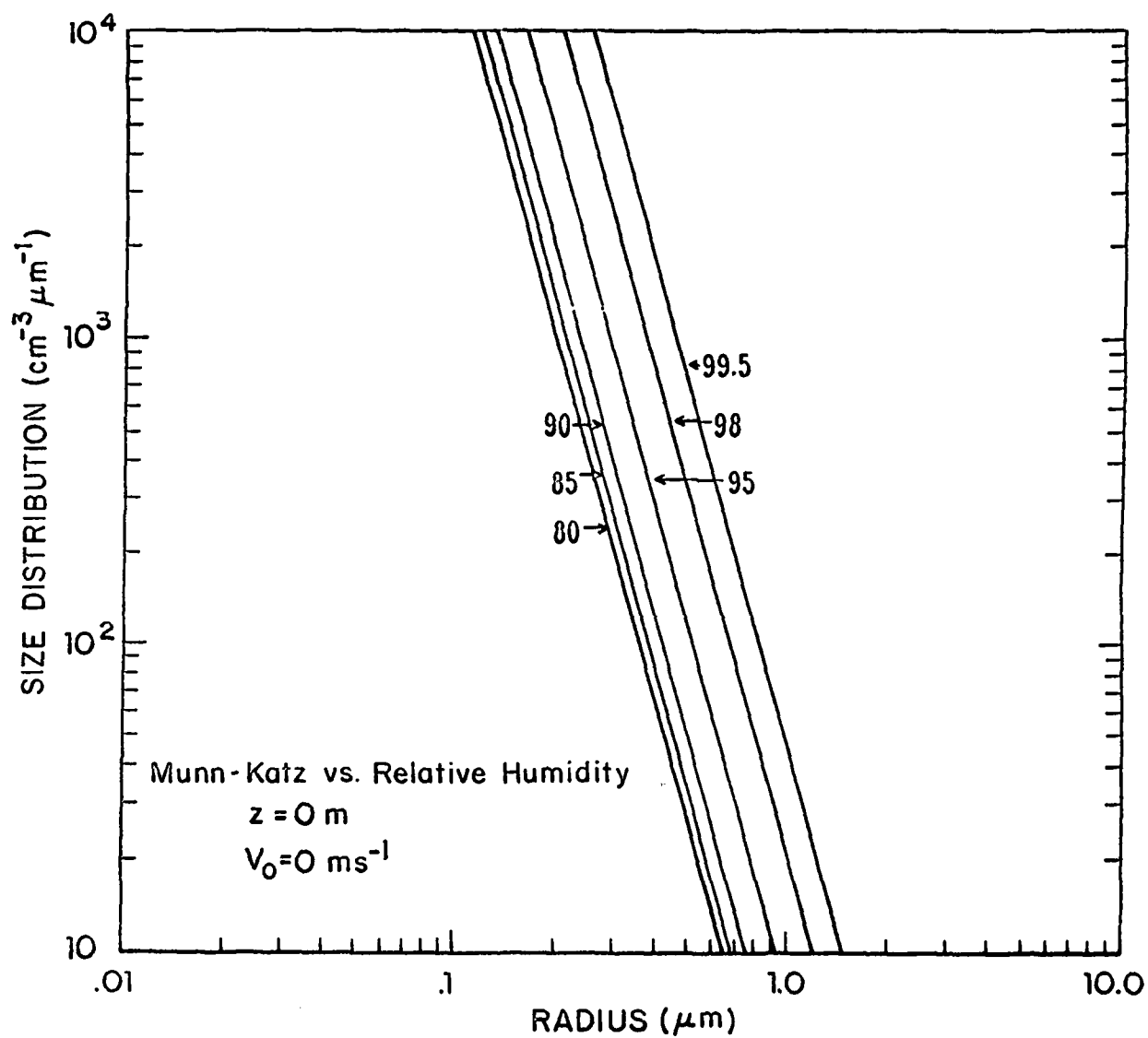


Figure 9

Dependence of NSWC model size distribution  
 on relative humidity ( $z = 0 \text{ m}$ ,  $WS = 0 \text{ ms}^{-1}$ )

and 9 illustrate the dependence of the size distribution given by Equation (11) on wind speed and relative humidity, respectively. The relative humidity dependence given by the growth factor  $F$  in (11) used in both modes is that due to Fitzgerald (1975, 1979).

A recent comparison between LOWTRAN (Selby et al., 1978) and NSWC codes has been performed (Hughes et al., 1979), which illustrates their validity for predicting visible and near infrared extinction. It may be argued that due to compositional and size distinctions between the accumulation and coarse modes, different growth factors should be used. An advantage of the coarse mode expression in equation (11) above is that the number density realistically increases with wind speed as new particles are mechanically added. This is illustrated in Table 6.

#### 4.2 Effect of Relative Humidity

Relative humidity directly affects both the equilibrium size (i.e. radius) of an aerosol droplet and the complex index of refraction. One approach to including relative humidity (RH) effects is based on evaluating the humidity growth factor  $F(f)$  defined as:

$$F(f) = \frac{r(f)}{r_0} \quad (12)$$

where  $r(f)$  is the equilibrium radius of the particle at  $f \approx (RH/100\%)$  and  $r_0$  is the radius of the dry particle. Given the dry particle size distribution  $n(r_0)$ , the response

Relative Humidity (%)	Coarse Mode Number Density ( $\text{cm}^{-3}$ ) Munn-Katz Model			
	0 m/s	5 m/s	7 m/s	10 m/s
50	1.37	3.27	7.33	13.5
70	1.47	3.51	7.86	14.10
80	1.59	3.78	8.47	15.21
90	1.89	4.49	10.05	18.06
95	2.31	5.51	12.34	22.15

Table 6. Coarse Mode Number Densities ( $\text{cm}^{-3}$ ) as a function of relative humidity (RH) and wind speed (ws) for the Munn-Katz model.

to relative humidity is obtained by substituting the appropriate growth factor, such as:

$$n[r(f)] = n[F(f)r_0] \quad (13)$$

where  $n[r(f)]$  is the size distribution at  $RH=f$ . This assumes that the total number density is constant. Alternatively, if the number density distribution is specified by a standard size distribution function (such as log normal, for example), the relative humidity effects can be obtained by multiplying the appropriate median radius parameter by the growth factor.

The complex refractive index at relative humidity  $f$ ,  $\tilde{m}_f$ , is obtained by volume mixing the refractive index of dry particles  $\tilde{m}_0$  and that of water  $\tilde{m}_w$ , according to:

$$\tilde{m}_f = \tilde{m}_0 F(f)^{-3} + \tilde{m}_w [1 - F(f)^{-3}] \quad (14)$$

This combined approach has been used in most modeling of relative humidity effects on aerosol size distribution (Nilsson, 1979; Shettle and Fenn, 1979; Hughes and Richter, 1979).

The appropriate growth factor  $r/r_0=F$  is evaluated based on aerosol growth theory. The theoretical basis of aerosol growth has been discussed by numerous authors (Nilsson, 1979; Köhler, 1926; Hänel, 1968, 1972; Junge and McLaren, 1971; Winkler, 1973; Fitzgerald, 1975, 1979, among others). In general, a particle model is adopted. The average aerosol is assumed to be an internal mixture (Winkler, 1973) made up of

several specifiable substances mass-weighted according to their total proportion in the distribution. At zero relative humidity, the particles are assumed to consist of water-soluble fraction mass  $E$  and a complementary insoluble mass fraction,  $(1 - E)$ . As relative humidity increases a fraction  $E$ , the water-soluble part gradually dissolves, and the aerosol droplet grows by absorption of water vapor (Fitzgerald, 1975). The mass of the dry particle is given by:

$$m_0 = \alpha \rho_0 r_0^3 \quad (15)$$

where  $r_0$  is the radius of the dry particle,  $\rho_0$  is the mean density of the dry particle, and  $\alpha = 4\pi/3$ . The mean density of the dry particle  $\rho_0$  is defined by summing soluble and insoluble volumes to give:

$$\rho_0 = \frac{\rho_s \rho_i}{E \rho_i + (1-E) \rho_s} \quad (16)$$

where  $\rho_s$  is the density of the water soluble fraction, and  $\rho_i$  is the density of the insoluble fraction. The mass of the water soluble fraction  $m_{ds}$  is:

$$m_{ds} = E m_0 \quad (17)$$

while the mass of dissolved matter is:

$$m_s = \epsilon(f) m_{ds} = \epsilon(f) E m_0 \quad (18)$$

where the dissolved fraction  $\epsilon$  depends on relative humidity. The mass of water in a particle of size  $r$  in equilibrium

with  $RH=f$  is:

$$\begin{aligned} m_w &= \alpha(r^3 - r_o^3) \rho_w \\ &= \alpha[F(f)^3 - 1] r_o^3 \rho_w \end{aligned} \quad (19)$$

where  $\rho_w$  is the density of water. Based on (15) - (19), the density of the salt solution  $\rho'$  and the molecular weight of the salt solution,  $M'$  may be derived by volume-weighting:

$$\rho' = \frac{m_s + m_w}{m_s/\rho_s + m_w/\rho_w} = \frac{\rho_s g(r)}{r^3 \rho_s + r_o^3 (\epsilon E \rho_o - \rho_s)} \quad (20)$$

$$M' = \frac{m_s + m_w}{m_s/M_s + m_w/M_w} = \frac{M_s M_w g(r)}{M_s r^3 + (m_w \epsilon E \rho_o - m_s) r_o^3} \quad (21)$$

where:

$$g(r) = r^3 + (\epsilon E \rho_o - 1) r_o^3. \quad (22)$$

and  $M_s$ ,  $M_w$  are the molecular weights of solute and water, respectively.

The growth factor may be evaluated from the relationship between relative humidity and the equilibrium radius of an aqueous solution. The ratio of the equilibrium vapor pressure over the surface of the aerosol droplet of radius  $r$ ,  $P_r$ , and that over a planar water surface,  $P_\infty$  is given by:

$$\frac{P_r}{P_\infty} = \exp \left[ \frac{2\sigma' M'}{r \rho' R_v T} \right] \left[ 1 + \frac{i M_w m_s}{M_s m_w} \right]^{-1} \quad (23)$$

where  $\sigma'$  = surface tension of the solution

$$= \sigma_w(T) + b(m_s/m_w)$$

$\sigma_w(T)$  = surface tension of water at temperature T

b = a constant depending on solute

$M'$  = molecular weight of the solution

r = radius of the droplet

$\rho'$  = density of the solution

$R_v$  = specific gas constant of water vapor

T = temperature of the droplet (K)

i = van't Hoff factor, which is determined empirically, and indicates the degree of dissociation

$M_w$  = molecular weight of water

$M_s$  = molecular weight of the salt

$m_w$  = mass of water, and

$m_s$  = mass of salt

Assuming instantaneous equilibrium with surrounding air (i.e. time-dependent case), the ratio above (23) is identically equal to the relative humidity, or substituting from (15) - (22):

$$f = \exp \left( \frac{2 \left[ \sigma_w(T) + b \frac{\epsilon E \rho_o}{(r/r_o)^3 - 1} \right] \left[ \frac{M_s M_w [(r/r_o)^3 - 1 + \epsilon E \rho_o]}{M_s [(r/r_o)^3 - 1] + M_w \epsilon E \rho_o} \right]}{r_o (r/r_o) \frac{[(r/r_o)^3 - 1 + \epsilon E \rho_o] \rho_s}{[(r/r_o)^3 - 1] \rho_s + \epsilon E \rho_o} R_v T} \right) \quad (24)$$

$$\times \left[ 1 + i \frac{M_w}{M_s} \frac{\epsilon E \rho_o}{(r/r_o)^3 - 1} \right]^{-1}$$

where the growth factor  $F(f)$  is  $r/r_0$  in the expression above. Figure 10 (Fitzgerald, 1979) illustrates a comparison between a number of theoretical models of  $F(f)$  and measurements for maritime aerosols. In this effort we have sought to distinguish between growth factors for the accumulation (or fine) mode and for the coarse mode. Several candidate calculations for each of these modes are presented in Figures 11 and 12, respectively. Note that for a given relative humidity in the range 50-95%, the growth factor for the coarse mode is generally greater than that for the fine (accumulation) mode. Above 80% relative humidity, the coarse mode growth factors of Fitzgerald (1975, 1979) and Shettle and Fenn (1979) are approximately the same. Below 80%, however, Fitzgerald's values essentially average over the hysteresis phenomenon between 40 and 76% relative humidity while the others inherently assume the onset of deliquescence at about 70%.

#### 4.3 Candidate Physical Models

Based on the previous discussion, two models were adopted to perform the sensitivity studies relating meteorological variables to emergent intensities required in this effort. The first of these is the Shettle and Fenn (1979) relative humidity dependent maritime model prescribed by the parameters in Table 5 and the log normal distribution for each mode given by equation (9).



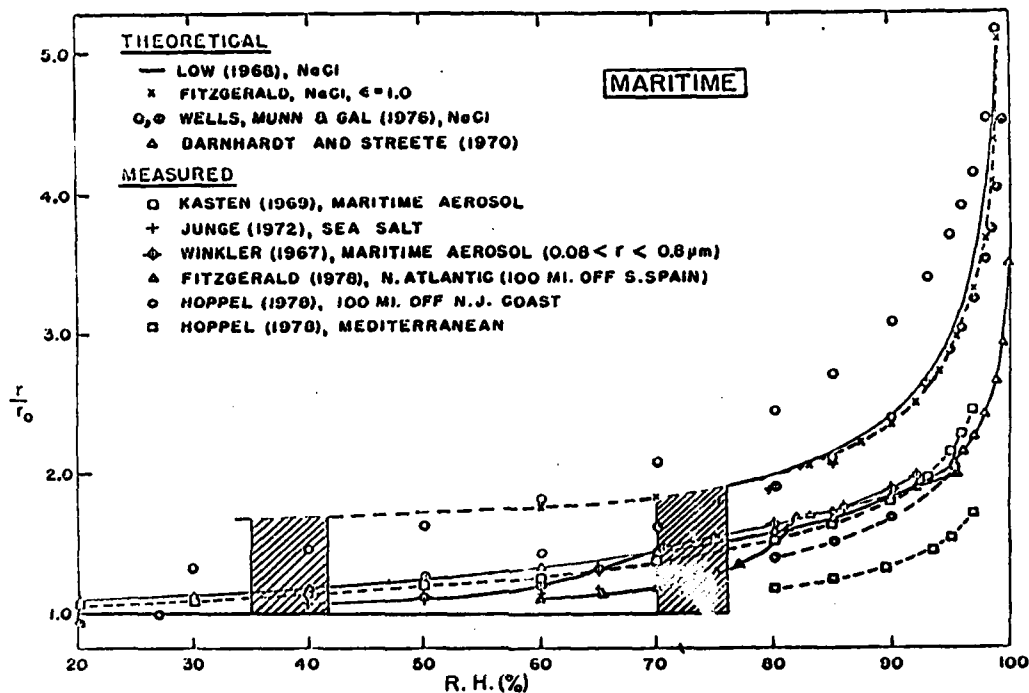


Figure 10

Measured and calculated growth curves for  
NaCl particles and natural aerosols  
(Fitzgerald, 1979)

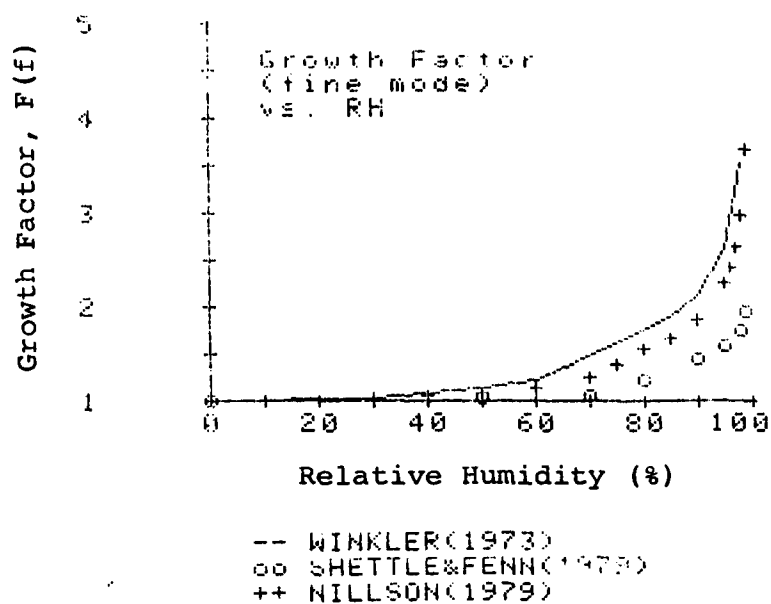


Figure 11  
Growth Factor (accumulation mode)

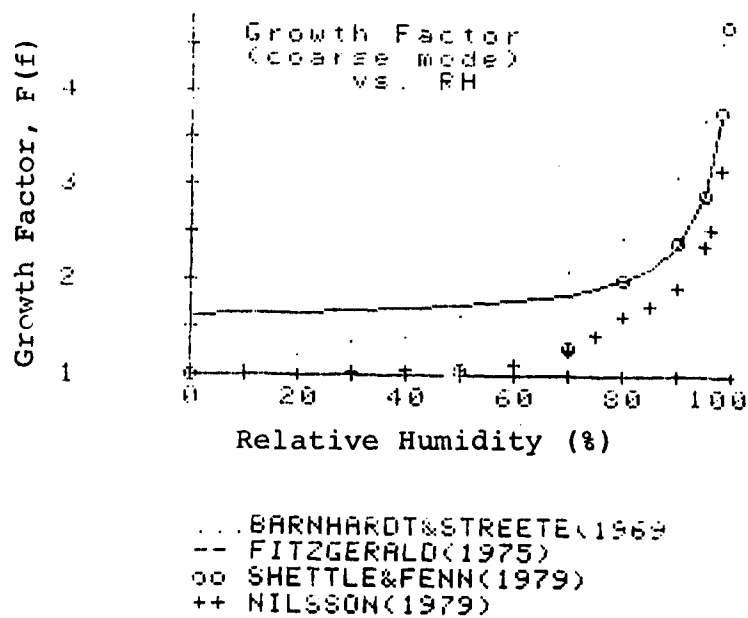


Figure 12  
Growth Factor (coarse mode)

The second model is a hybrid expression consisting of a linear combination of the accumulation or tropospheric mode from Shettle and Fenn (1979) and the wind speed dependent coarse mode from the Munn-Katz model. In employing this model, the aerosol growth factor [equation (12)] for the accumulation (fine) mode is that used by Shettle and Fenn (1979) while that in the coarse mode is that given by Fitzgerald (1975, 1979) [see Figures 11 and 12]. Two advantages of this approach, therefore, are that: (a) aerosol growth rates with relative humidity are distinct between the modes and (b) wind speed dependence is treated in the coarse mode. In employing this hybrid model, number densities in the coarse mode vary with relative humidity and wind speed as given in Table 6, while the accumulation mode number density is either held constant or normalized to correspond to a specified surface visual range. Figures 13(a)-(d) illustrate the hybrid size distribution variation with relative humidity at fixed wind speeds. The number density in the fine mode is set at  $5000 \text{ cm}^{-3}$ . Figures 14(a) and (b) illustrate the variation of the same distribution with wind speed ( $0, 5, 7, 10 \text{ ms}^{-1}$ ) for fixed relative humidities of 50 and 95%, respectively.

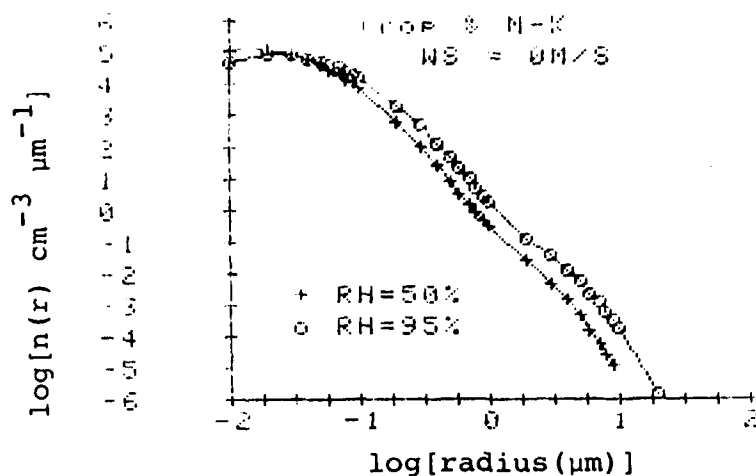


Figure 13(a)

Hybrid Size Distribution Variation  
with Relative Humidity ( $WS = 0.0 \text{ ms}^{-1}$ )

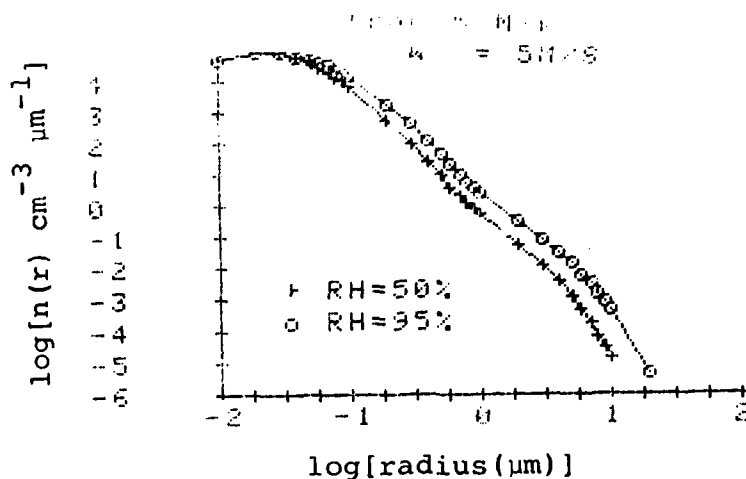


Figure 13(b)

Hybrid Size Distribution Variation  
with Relative Humidity ( $WS = 5 \text{ ms}^{-1}$ )

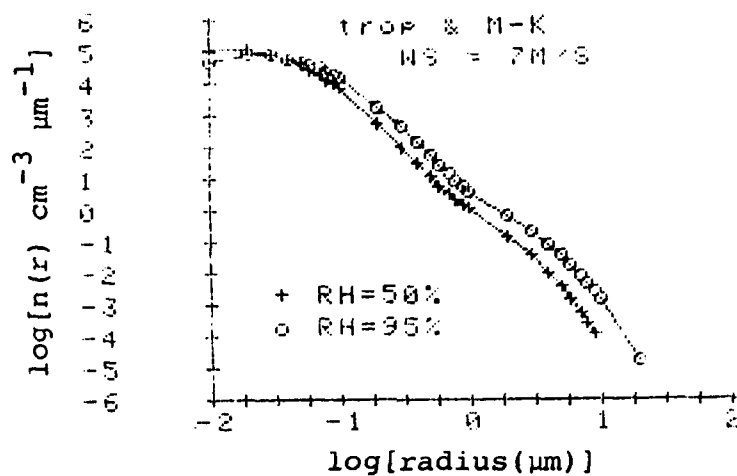


Figure 13(c)

Hybrid Size Distribution Variation  
with Relative Humidity (WS = 7 ms<sup>-1</sup>)

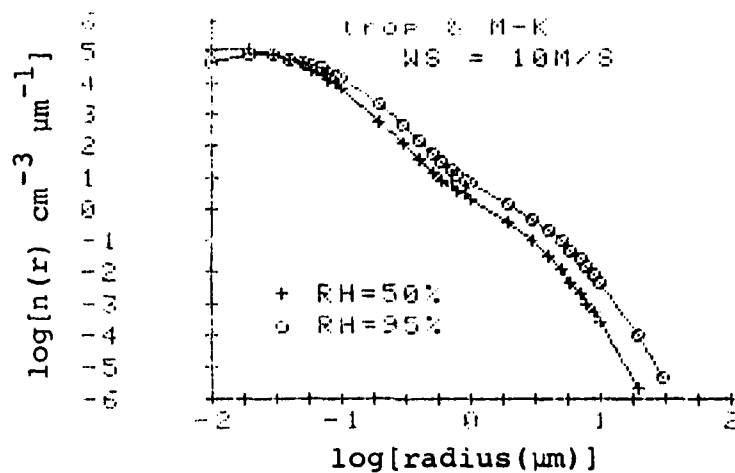


Figure 13(d)

Hybrid Size Distribution Variation  
with Relative Humidity (WS = 10 ms<sup>-1</sup>)

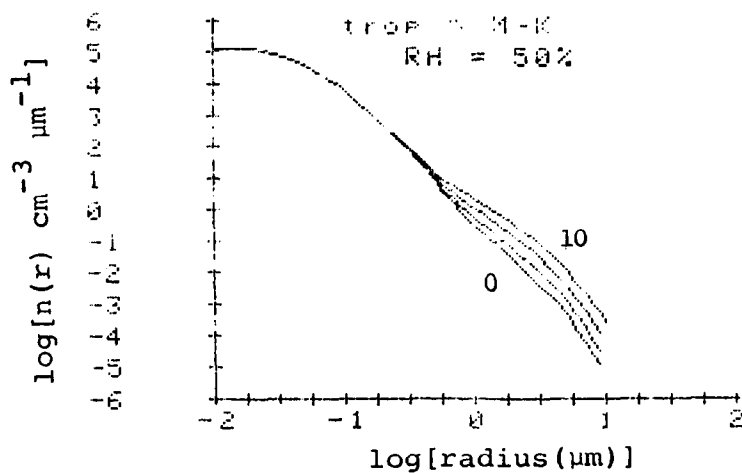


Figure 14(a)

Hybrid Size Distribution Variation  
with Wind Speed ( $RH = 50\%$ )

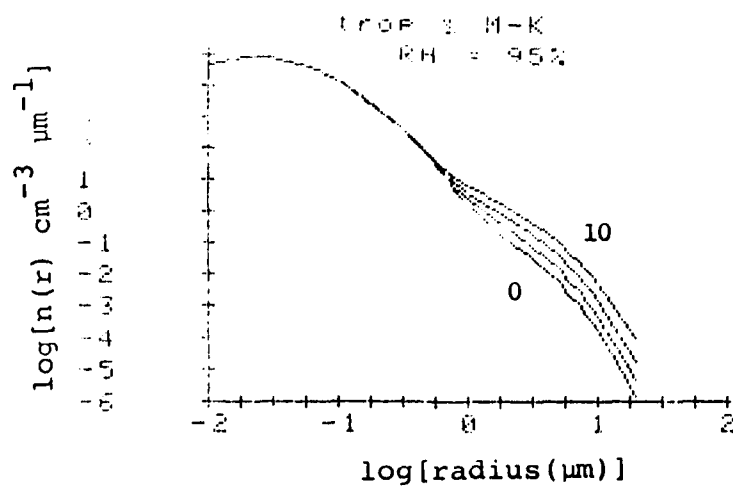


Figure 14(b)

Hybrid Size Distribution Variation  
with Wind Speed ( $RH = 95\%$ )

## 5. AEROSOL OPTICAL PROPERTIES

### 5.1 Mie Theory Calculations

Given the dependence of size distribution on wind speed and relative humidity (i.e. growth factor) and model aerosol complex index of refraction on growth factor [see equation (14)] classical Mie theory (Mie, 1908) may be used to evaluate the optical properties required for radiative transfer calculations (see Figure 2). Details of the Mie theory may be found in a number of standard references Deirmendjian, 1969; van de Hulst, 1957; Hansen and Travis, 1974; McCartney, 1976).

Specifically, these optical properties include: (a) extinction coefficient,  $\beta_e$ ; (b) single scattering albedo,  $\omega_0$ ; and (c) angular scattering function  $P(\theta)$  or asymmetry factor,  $g$ . Each of these parameters is a function of fundamental variables such as wavelength,  $\lambda$ , size distribution,  $n(r)$ , and complex index of refraction,  $\tilde{m}$ . The extinction coefficient,  $\beta_e(\lambda)$ , for an aerosol with size distribution,  $n(r)$ , is given by:

$$\beta_e(\lambda) = \pi \int_0^{\infty} r^2 Q_e(r, \lambda, \tilde{m}) n(r) dr \quad (25)$$

where  $Q_e$  is the Mie efficiency factor for extinction for a particle of radius  $r$ . Similar expressions are applicable for the absorption coefficient,  $\beta_a(\lambda)$ , and scattering

coefficient,  $\beta_s(\lambda)$ , substituting Mie efficiency factors  $Q_a$  and  $Q_s$ , respectively (where  $Q_e = Q_a + Q_s$ ). These efficiency factors are computed using readily available computer programs. (Hansen and Travis, 1974; Dave, 1969; 1970).

The single scattering albedo is the ratio of scattering coefficient to extinction coefficient for a given aerosol size distribution. Based on the discussion above:

$$\omega_0(\lambda) = \beta_s(\lambda)/\beta_e(\lambda) = \int_0^\infty r^2 Q_s n(r) dr / \int_0^\infty r^2 Q_e n(r) dr. \quad (26)$$

The angular scattering (or phase) function determines the fraction of incident light at a particular wavelength  $\lambda$  scattered from the direction of the source into the direction  $\theta$  degrees ( $0 \leq \theta \leq 180$ ) from the source. The expression for the angular scattering function is:

$$P(\theta) = \frac{\lambda^2}{2\pi\beta_s} \int_0^\infty [i_1(\theta) + i_2(\theta)] n(r) dr \quad (27)$$

where  $i_1$  and  $i_2$  are the Mie angular intensity functions for a particulate of radius  $r$  and complex of refraction  $\tilde{m}$  at a specific wavelength  $\lambda$ . These functions can be evaluated using available Mie theory computer codes. For a number of approximate radiative transfer techniques such as the one described in Section 6, it is useful to characterize the aerosol angular scattering function by a single asymmetry parameter,  $g$ , defined as (Joseph et al, 1976):



$$g = \frac{1}{2} \int_{-1}^{+1} \cos\theta P(\theta) d(\cos\theta) \quad (28)$$

Values of the g factor range from +1.0 for complete forward scatter to -1.0 for complete backscatter.

## 5.2 Meteorological Dependence of Aerosol Optical Properties

Mie theory calculations of  $\beta_e(\lambda)$ ,  $\omega_0(\lambda)$ , and  $g(\lambda)$  were required for the model aerosol size distributions described in section 4.3 within the wavelength region 0.4-1.1  $\mu\text{m}$  and for representative values of relative humidity and wind speed. Necessary values for the maritime model and accumulation mode of the hybrid aerosol model were available from tabulations in Shettle and Fenn (1979). For the coarse mode of the hybrid model, Mie theory calculations were performed using a modified version of the code from Hansen and Travis (1974). Appropriate wavelength dependent indices of refraction were obtained by volume weighting according to equation (14) using Fitzgerald's (1975, 1979) growth factor. Indices of refraction for water and sea salt were obtained from Hale and Qerry (1973) and Volz (1972), respectively, as presented in Shettle and Fenn (1979).

### 5.2.1 Maritime Model

Extinction coefficients ( $\text{km}^{-1}$ ) and asymmetry parameters for the maritime model (assuming  $N=4000 \text{ cm}^{-3}$ ) as a function of relative humidity in the spectral range 0.4-1.1  $\mu\text{m}$  are

presented in Figures 15(a) and (b), respectively. Note that both extinction coefficient and asymmetry parameter in this model are relatively wavelength independent within this spectral interval, but strongly influenced by relative humidity.

#### 5.2.2 Hybrid Model

Figures 16(a) and (b) illustrate the wavelength/relative humidity dependence of the extinction coefficient ( $\text{km}^{-1}$ ) and asymmetry parameter, respectively, of the hybrid model fine mode only ( $N=5000 \text{ cm}^{-3}$ ). For this mode, extinction decreases with increasing wavelength with a dependence which may be approximated by:

$$\beta_e(\lambda) = \text{const} / \lambda^\alpha \quad (29)$$

where the Angstrom (1961) coefficient is such that  $1.0 \leq \alpha \leq 2.0$ . Additionally, as wavelength increases scattering asymmetry decreases.

Analogous calculations for the hybrid model, wind speed dependent coarse mode are presented in Figures 17(a,b), 18(a,b), 19(a,b) and 20(a,b) for wind speeds of 0, 5, 7, and  $10 \text{ ms}^{-1}$ , respectively. Generally, although the magnitude of the extinction due to the coarse mode is less than that in the fine mode [Figure 16(a)], the coarse mode extinction is much less wavelength dependent and much more dependent on relative humidity due to its larger sized particles. For

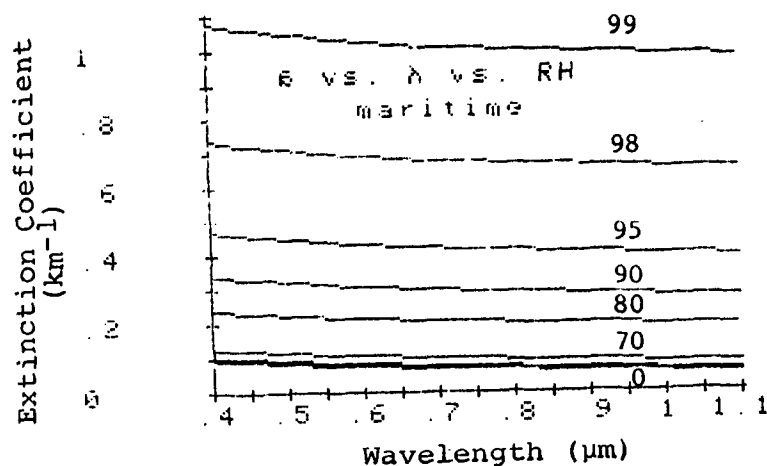


Figure 15(a)  
Extinction Coefficient ( $\text{km}^{-1}$ ) - Maritime Model  
(from Shettle and Fenn, 1979)

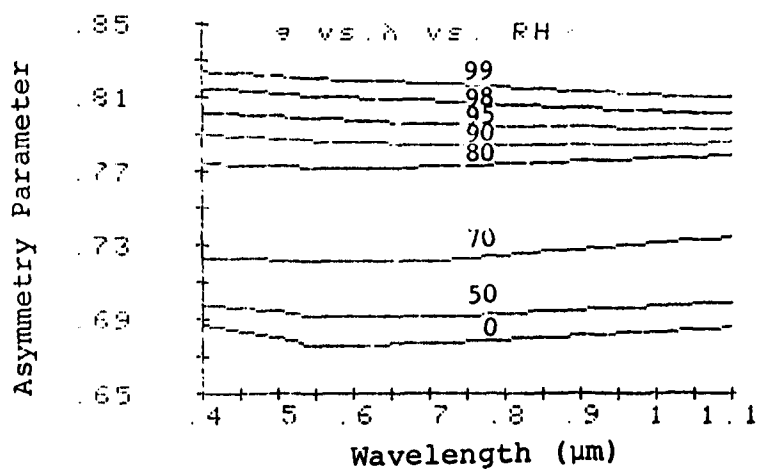


Figure 15(b)  
Asymmetry Parameter-Maritime Model  
(from Shettle and Fenn, 1979)

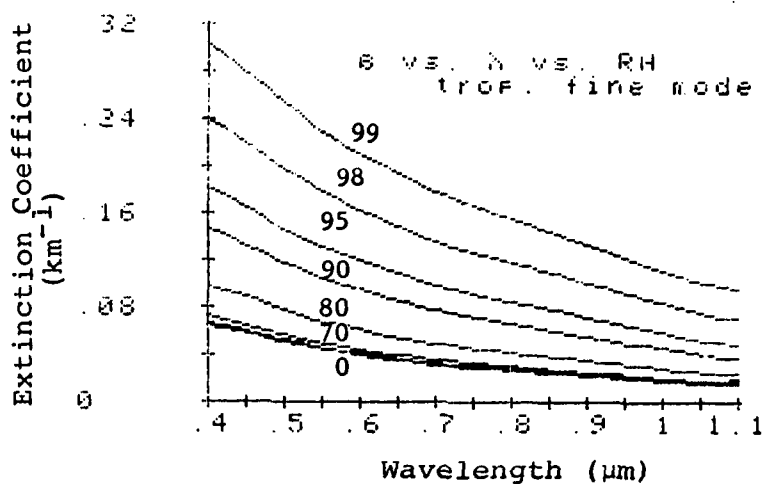


Figure 16(a)

Extinction Coefficient ( $\text{km}^{-1}$ ) -  
Hybrid Model Fine Mode  
(from Shettle and Fenn, 1979)

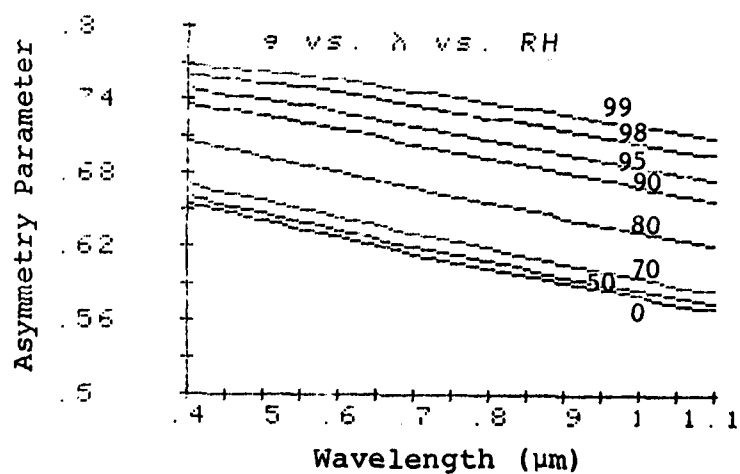


Figure 16(b)

Asymmetry Parameter-Hybrid Model Fine Mode  
(from Shettle and Fenn, 1979)

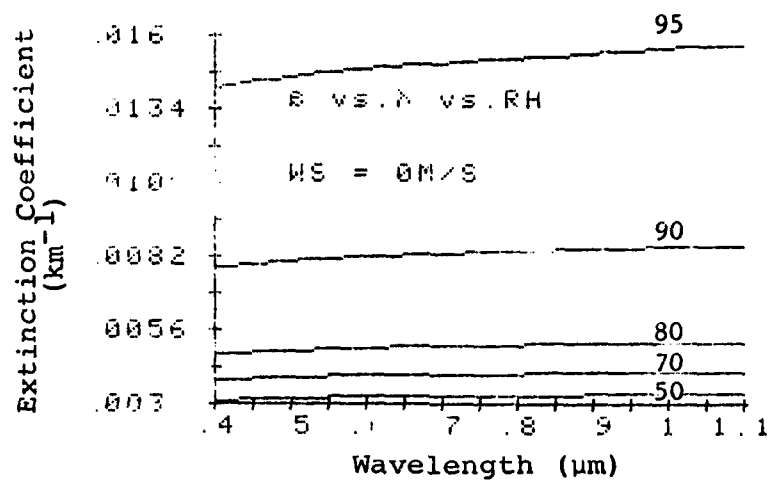


Figure 17(a)

Extinction Coefficient ( $\text{km}^{-1}$ ) -  
Hybrid Model Coarse Mode (WS = 0  $\text{ms}^{-1}$ )

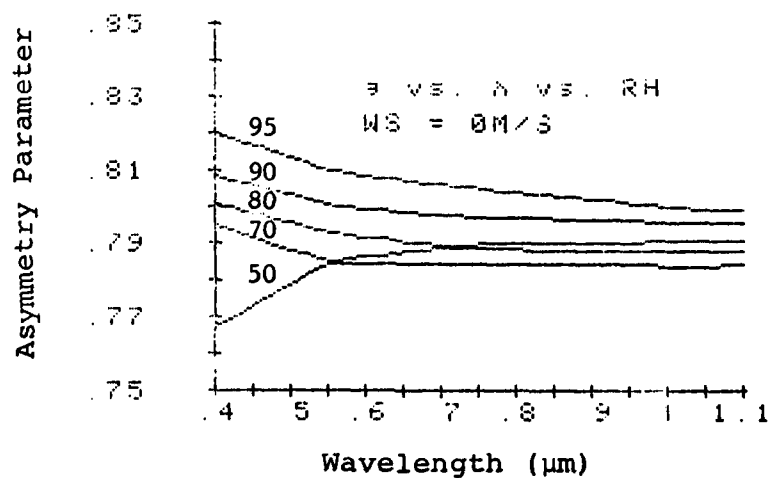


Figure 17(b)

Asymmetry Parameter-Hybrid Model  
Coarse Mode (WS = 0  $\text{ms}^{-1}$ )

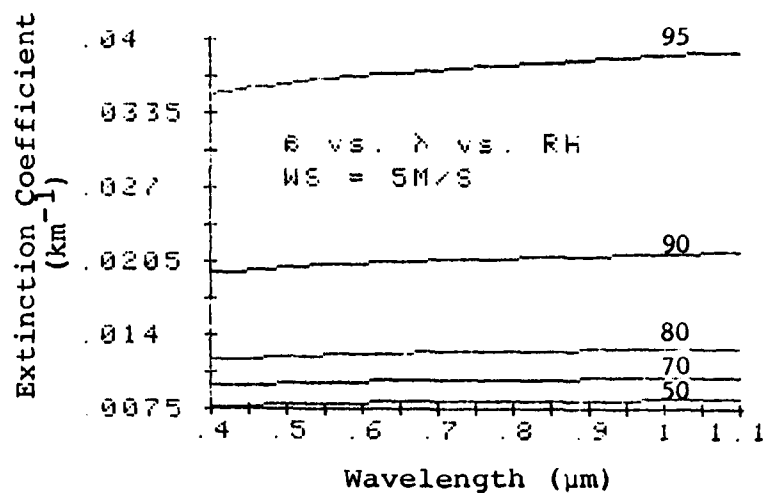


Figure 18(a)

Extinction Coefficient ( $\text{km}^{-1}$ ) -  
Hybrid Model Coarse Mode (WS = 5  $\text{ms}^{-1}$ )

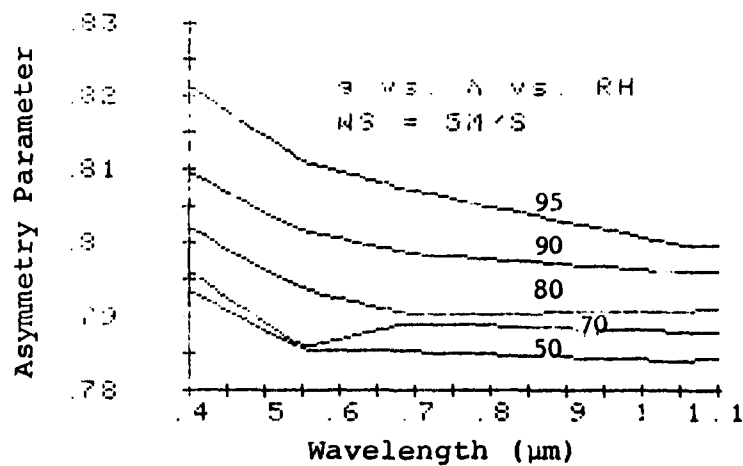


Figure 18(b)

Asymmetry Parameter-Hybrid Model  
Coarse Mode (WS = 5  $\text{ms}^{-1}$ )

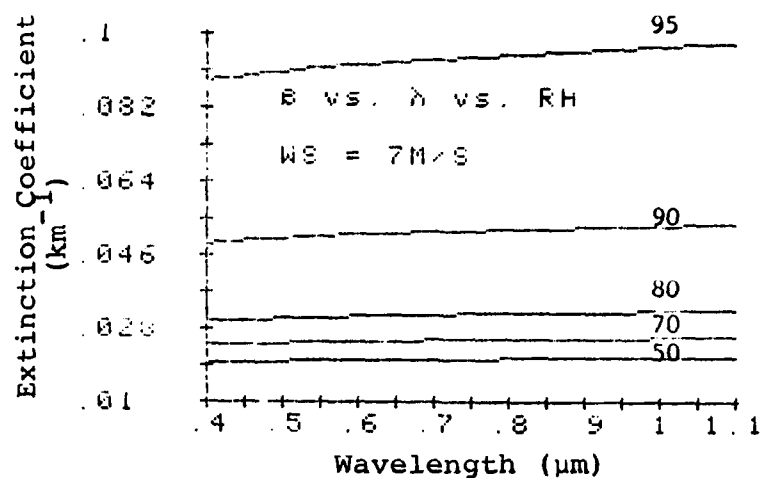


Figure 19(a)

Extinction Coefficient ( $\text{km}^{-1}$ ) -  
Hybrid Model Coarse Mode (WS = 7  $\text{ms}^{-1}$ )

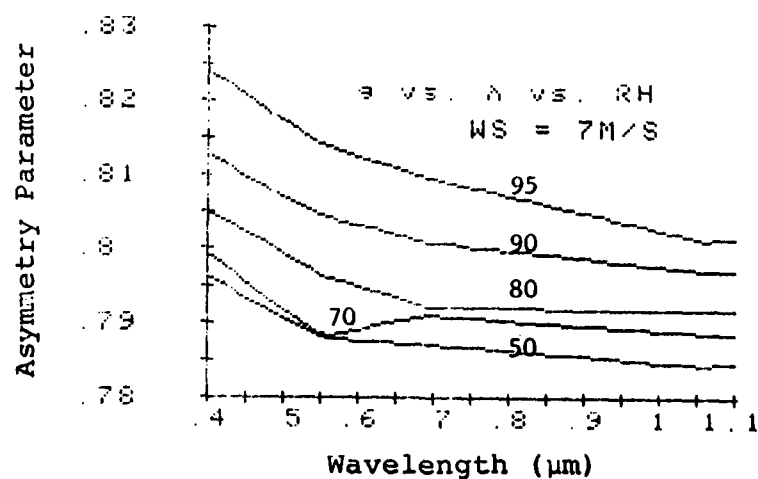


Figure 19(b)

Asymmetry Parameter-Hybrid Model  
Coarse Mode (WS = 7  $\text{ms}^{-1}$ )

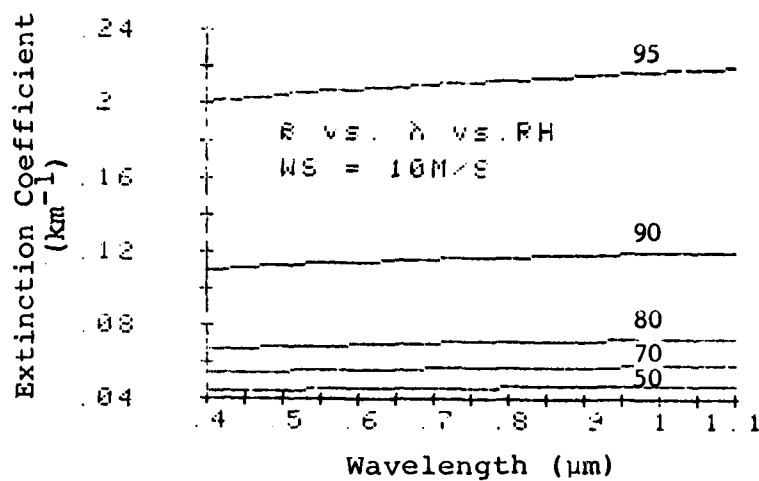


Figure 20(a)

Extinction Coefficient ( $\text{km}^{-1}$ ) -  
Hybrid Model Coarse Mode (WS =  $10 \text{ ms}^{-1}$ )

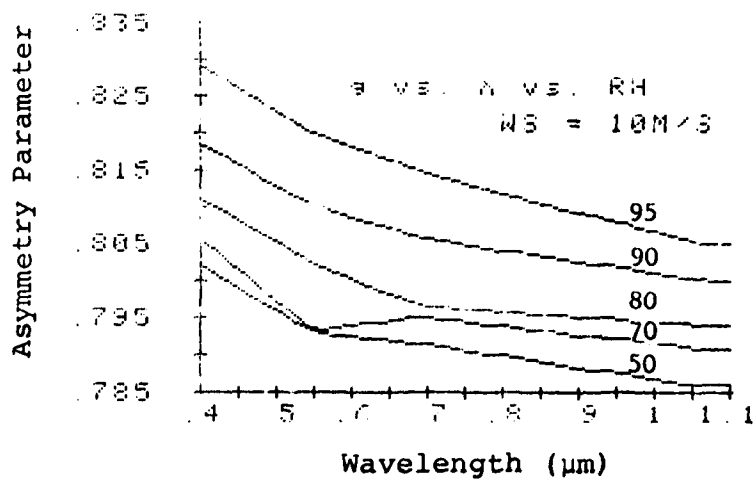


Figure 20(b)

Asymmetry Parameter-Hybrid Model  
Coarse Mode (WS =  $10 \text{ ms}^{-1}$ )



the same reason, its range of asymmetry parameters is greater than that in the fine mode.

### 5.3 Number Density/Visual Range Normalization

As remarked earlier, the overall normalization of the aerosol size distributions adopted may be discussed either in terms of number density ( $\text{cm}^{-3}$ ) or visual range (km). Aerosol extinction at  $0.55 \mu\text{m}$ ,  $\beta^e(0.55)$ , and visual range,  $V_R$ , are related approximately by the relation (Koschmieder, 1924; Horvath and Noll, 1969):

$$V_R(\text{km}) = 3.912/[\beta^e(0.55) + \bar{\beta}_R^s(0.55)] \quad (30)$$

where the Rayleigh scattering coefficient at  $0.55 \mu\text{m}$  given by equation (3) is  $0.012 \text{ km}^{-1}$ .

Using equation (30) and the aerosol extinction coefficients evaluated in §5.2, corresponding visual ranges may be calculated assuming the fixed number densities of  $4000 \text{ cm}^{-3}$  for the maritime model and  $5000 \text{ cm}^{-3}$  for the fine mode of the hybrid model. For the hybrid model including the Munn-Katz coarse mode, the coarse mode number densities are not constant but are given in Table 6. The visual ranges corresponding to the adopted models are presented in Table 7 as a function of relative humidity and, where appropriate, wind speed.

Alternatively, it may be desirable to consider constant visual range scenarios. In this case, it is necessary to

adjust the total number density in the distribution to provide the appropriate value of aerosol extinction at 0.55  $\mu\text{m}$ . Number densities adjusted to correspond to visual ranges of 5,10,23, and 50km are presented in Table 8. For the hybrid model it was decided to retain the coarse mode number densities given in Table 6 and adjust only the fine mode number densities.

For the most part subsequent simulated radiance results are presented in terms of the fixed number density models as given in Table 7. However, a few results are presented as functions of visual range.

#### 5.4 Aerosol Optical Depths, $\tau_i^{e,s}$

Aerosol optical depths for scattering and extinction required in the radiative transfer calculation may be evaluated based on the scattering and extinction coefficients described above for each adopted model. The scattering or extinction optical depth for a given mode  $i$  is defined in analogy to equation (1) as:

$$\tau_i^{e,s}(\lambda) = \int \beta_i^{e,s}(\lambda, z) dz \quad (31)$$

If an approximately exponential dependence of aerosol number density with altitude is assumed with scale height  $H_i$  (or a uniformly mixed situation with mixing height  $H_i$ ), equation (31) may be approximated as :

Relative Humidity (%)	Visual Range (km)				
	Shettle & Fenn (1979)		Combined Tropospheric-Munn-Katz		
	Tropospheric N=5000 cm <sup>-3</sup>	Maritime N=4000 cm <sup>-3</sup>	0 m/s	5 m/s	7 m/s 10 m/s
50	67.7	39.6	64.1	59.4	50.2 38.0
70	63.8	32.1	59.9	55.0	45.5 33.5
80	49.1	16.9	46.3	42.6	35.5 26.3
90	33.8	12.0	31.7	28.8	23.5 17.0
95	27.4	8.7	25.0	21.8	16.7 11.2

Table 7. Dependence of visual range on specified meteorological variable for adopted aerosol models.

Number Density (cm <sup>-3</sup> ) [Adjusted for Visual Range]													
Visual Range (km)	Maritime Model (Both Nodes) Relative Humidity (%)			Tropospheric & Munn-Katz Model (Fine Mode) Relative Humidity (%)									
				50			80			95			
				Wind Speed (m/s)									
	50	80	95	0	7	10	0	7	10	0	7	10	
5	35484	14042	7047	83750	82083	79166	56666	54583	51833	28958	25958	21625	
10	17467	6912	3469	41250	39167	36458	27667	25833	22917	14000	11000	6625	
23	7283	2882	1446	17083	15000	12333	11333	9417	6583	5500	2542	*	
50	3053	1208	606	7083	5000	2292	4542	2625	*	2000	*	*	

(\* non-physical)

Table 8. Number Densities ( $\text{cm}^{-3}$ ) for adopted aerosol models as a function of specified visual range and meteorological variables.

$$\tau_i^{e,s}(\lambda) = \bar{\beta}_i^{e,s}(\lambda) H_i \quad (32)$$

where  $\bar{\beta}_i^{e,s}$  represents a near surface or uniformly mixed value. In general, subsequent results assume a scale height of 1.2 km for the maritime model and fine mode of the hybrid model based in part on Elterman (1970). For the Munn-Katz coarse mode a scale height of 0.8 km is used (Hughes and Richter, 1979). These choices of scale height qualitatively describe the relatively longer lifetime of accumulation mode aerosols due to their smaller sizes and resultant resistance to loss due to gravitational settling. For the sensitivity studies which are performed on scale height, however, it should be noted that the scale height value may be considered as the product of a physical height and a dimensionless constant which increases or decreases the total number density (with associated changes in surface visual range). Therefore, these calculations may be viewed as constant scale height calculations for varying number densities if desired.

## 6. RADIATIVE TRANSFER

### 6.1 Technique Selection Criteria

Radiative transfer theory provides a mathematical description of the interaction between incident solar radiation and the relevant optically active constituents of the atmosphere. For our purposes, these species include both ambient gases and aerosols. The interaction mechanisms treated by radiative transfer theory have been alluded to in the preceeding discussions of atmospheric optical properties and include molecular (Rayleigh) scattering (§3.1), gaseous absorption (§3.2), and aerosol absorption and scattering (§5.2). For the purpose of this study, it is minimally required that the radiative transfer treatment adopted handle: (a) multiple scattering, (b) the inherent anisotropic (i.e. highly directional) scattering characteristic of aerosols, (c) reflection of radiation at the atmosphere-ocean interface, and (d) the azimuthal dependence given by the sun/sensor/geometry.

A hierarchy of potential radiative transfer treatments exists (Hansen and Travis, 1974; Lenoble, 1977) ranging from the simple, single scattering analysis demonstrated in Fett and Isaacs (1979) to a variety of highly numerical computational algorithms (e.g. Braslau and Dave, 1947 a,b). In selecting an appropriate approach in this investigation, criteria have included: (a) ability to satisfactorily treat mechanisms cited above, (b) maximization of the number of sensitivity analyses which could be undertaken, (c)

optimization of available computer resources, and (d) consistency of approach with accuracies in other components of the investigation such as in specifying the physical aerosol models. For these reasons an approximate, analytical treatment was adopted.

## 6.2 Analytical Approaches

From a practical perspective, the essential difference between numerical and analytical approaches is that the latter require very little computational effort and hence a significant amount of computer time may be saved if they are implemented. Unfortunately, exact analytical treatments are available only for a few cases which are not immediately applicable to geophysical remote sensing problems. They are of interest mathematically, however, to compare with corresponding cases of more computationally complex numerical techniques. These cases include, for the most part, approaches based on Chandrasekhar's H functions for semi-infinite atmospheres and X and Y functions for finite atmospheres (Chandrasekhar, 1950). For the former set of problems solutions are available for isotropic (Stibbs and Weir, 1959; Abhyankar and Fymat, 1971), Rayleigh (Chandrasekhar, 1950; Lenoble, 1970). and various anisotropic phase functions (Chandrasekhar, 1950; Sobolev, 1956; Kolesov, 1972). For finite atmospheres, solutions are available only for isotropic (Carlstedt, 1966) and Rayleigh scattering (Sekera and Kahle, 1966).

For remote sensing problems relevant to radiative transfer in the atmosphere-ocean system, methods are required which treat a finite atmosphere (i.e., the total optical depth is not infinite) with scattering properties which are anisotropic in order to simulate aerosol scattering. Although exact analytical treatments are not available in such cases, a variety of approximate analytical methods with quantifiable accuracy may be employed. The utility of approximate analytical treatments lies in their extreme computational efficiency while retaining many of the salient physical mechanisms of radiative transfer involved.

Approximate analytical methods may be conveniently classified into one of two groups:

- . approaches based on taking the first few tractable orders of more extensive numerical treatments
- . approaches formulated specifically as approximate treatments

Examples falling into the first category include first (Deirmendjian, 1969) and second (Hovenier, 1971) order of scattering treatments explicitly formulated from successive order of scattering approaches (Irvine, 1965; Nagel et al., 1978), analytic two and four stream (Liou, 1974) approximations based on discrete ordinate methods (Liou, 1973), and the two-step function approach (Burke and Sze, 1977) derived from more general variational methods (Sze, 1976).

Treatments explicitly formulated as approximate



approaches include various similarity relations (van de Hulst and Grossman, 1968; Hansen, 1969), the Eddington approximation (Shettle and Weinman, 1970), and various general two-stream methods (Chu and Churchill, 1955; Coakley and Chylek, 1975).

The degree of accuracy intrinsic to a specific approximate analytical treatment varies not only with the treatment itself, but with the relevant optical propagation parameters involved. Expected errors may be quantified by examining certain standard cases and comparing accuracies either with available exact solutions or with numerical solutions of specified precision. For example, Table 9 lists percent error figures for a comparison between emergent,  $I(0, -1.0, \mu)$ , and transmitted,  $I(\tau^*, -1.0, \mu)$ , intensities derived from single scattering vs. multiple scattering (Coulson et al., 1960) treatments in a Rayleigh atmosphere with the sun at zenith ( $\mu_0=1.0$ ) and zero surface albedo ( $A_L=0.0$ ).<sup>†</sup> Results are presented for various observer zenith angles ( $\mu$ ) and total atmospheric optical depths ( $\tau^*$ ). Note that even for this fundamental approximate analytical approach, errors are highly dependent on atmospheric optical depth, emphasizing the need to quantify the behavior of such treatments a priori.

---

<sup>†</sup> These parameters are defined in §6.4.

Table 9

	$I^+(\tau = 0, \mu)$			$I^-(\tau = \tau^*, \mu)$		
	$\tau^*$			$\tau^*$		
$\mu$	<u>0.10</u>	<u>0.25</u>	<u>0.50</u>	<u>0.10</u>	<u>0.25</u>	<u>0.50</u>
1.00	13.2	24.6	37.1	12.3	24.7	37.9
0.72	13.8	25.6	39.3	13.4	26.1	40.3
0.52	14.3	26.9	40.8	13.9	27.2	42.3
0.28	14.7	27.8	41.9	14.6	28.5	44.6
0.10	14.8	27.6	40.2	14.9	29.3	46.1

Percent error: single scattering vs. multiple scattering  
with Rayleigh phase function ( $\mu_0 = 1.0$ ,  $A_L = 0.0$ ).

### 6.3 Adopted Approach

Of the approximate techniques described above, simple finite stream approximations are particularly convenient to use. A recent review (Meador and Weaver, 1980) of extant two-stream approximations has compared the many approaches available within the formalism and defined domains of applicability and accuracy vs. total optical depth. Two-stream approximations are attractive, since accuracies are easily quantified, and the mathematics reduces to a set of analytical (although algebraically complex) equations. For the latter reason, computational efficiencies are extremely high (i.e., machine-usage time is minimal). Furthermore, with appropriate care in the formulation, scattering anisotropy and surface reflection may be treated by employing physically realistic boundary conditions.

For these reasons, the specific treatment adopted in this work is based on a recent extension (Kaufman, 1979) to an earlier two-stream formulation (Coakley and Chylek, 1975), which allows the specific azimuth/zenith angle dependence of emergent and transmitted intensities to be simulated. By employing calculated backscatter fractions (Wiscombe and Grams, 1976) for general aerosol-phase functions in the analysis, the general scattering anisotropy of the real atmosphere-ocean system may be calculated. This particular two-stream approach (Coakley and Chylek, 1975) is formulated to be well-behaved in the thin atmosphere limit, a trait particularly valuable for treating problems in the visible

and near infrared spectral regions.

#### 6.4 Theory

In order to simulate the emergent radiance  $I$ , measured by a meteorological satellite viewing the earth-atmosphere system, it is necessary to solve the radiative transfer equation for each wavelength (Goody, 1964):<sup>†</sup>

$$\mu \frac{dI}{d\tau}(\tau, \mu, \phi) = I(\tau, \mu, \phi) - \omega_0 J_S(\tau, \mu, \phi) \quad (33)$$

where:

$$J_S(\tau, \mu, \phi) = \frac{P(\theta_0)}{4\pi} Fe^{-\tau/\mu_0} + \frac{1}{4\pi} \int_0^{2\pi} \int_{-1}^1 P(\theta) I(\tau, \mu'; \phi) d\mu' d\phi' \quad (34)$$

In the above:

$I(\tau, \mu, \phi)$  = wavelength dependent radiance ( $\text{mW cm}^{-2} \mu\text{m}^{-1} \text{sr}^{-1}$ )

$J(\tau, \mu, \phi)$  = wavelength dependent source function

$\tau = \int_z^\infty \beta_\lambda(z) dz$  = wavelength dependent optical depth

$\tau^* = \int_0^\infty \beta_\lambda(z) dz$  = total optical depth from surface to space

---

<sup>†</sup>The derivation is treated in greater detail in the Appendix.

$\beta_{\lambda}(z) = \beta_R^S(\lambda) + \beta_g(\lambda) + \beta^e(\lambda)$  = height dependent,  
total extinction coefficient per unit length  
( $\text{km}^{-1}$ ) including Rayleigh scattering, gas  
absorption, and aerosol extinction contribu-  
tions.

$\mu = \cos\theta$  ( $\theta$  zenith angle of emergent radiance)

$\mu_0 = \cos\theta_0$  ( $\theta_0$  zenith angle of sun)

$\phi$  = azimuth angle of emergent radiance

$\omega_0(\lambda)$  = wavelength dependent single scattering albedo

$P[\theta]$  = wavelength dependent phase function for  
redirection of scattered radiance<sup>1</sup>

$\theta$  = scattering angle

$$= \mu\mu' + (1-\mu^2)^{\frac{1}{2}}(1-\mu'^2)^{\frac{1}{2}}\cos(\phi-\phi')$$

i.e. incident beam  $\mu, \phi$

scattered beam  $\mu', \phi'$

$\theta_0$  = scattering angle between direction of emergent  
radiance and direction of solar incidence  
( $\mu_0, \phi_0$ )

---

<sup>1</sup>The phase function  $P(\theta)$  is the effective phase function due to both molecular (Rayleigh) scattering and aerosol scattering properly weighted:

$$P(\theta) = \frac{\beta_R^S(z)P_R(\theta) + \beta^S(z)P_A(\theta)}{\beta_R^S(z) + \beta^S(z)}$$

where

$\beta_R^S, \beta^S$  = scattering coefficients due to Rayleigh and  
aerosol scattering, respectively

$P_R(\theta), P_A(\theta)$  = phase functions for Rayleigh and aerosol compo-  
nents

$F$  = wavelength dependent extraterrestrial solar  
flux

(These values shown in Fig. 21 from Thekaekara  
et al, 1969)

Equations (33) and (34) may be transformed into coupled  
differential equations for upward,  $F^+(\tau)$ , and downward,  
 $F^-(\tau)$ , flux profiles:

$$\tilde{A}\tilde{F} = \tilde{F} \quad (35)$$

where  $\tilde{F} = \begin{bmatrix} F^+(\tau) \\ F^-(\tau) \end{bmatrix}$

$$\tilde{F} = \begin{bmatrix} f_1 \\ f_2 \end{bmatrix},$$

the operator  $\tilde{A}$  is given by:

$$\tilde{A} = \left[ \frac{d}{d\tau} \tilde{1} - \tilde{\Gamma} \right] \quad (36)$$

where  $\tilde{1}$  is the identity operator:

$$\tilde{\Gamma} = \begin{pmatrix} \gamma_1 & -\gamma_2 \\ \gamma_2 & -\gamma_1 \end{pmatrix},$$

$$\gamma_1 = 2 [1 - \omega_0 (1 - \beta')] ,$$

$$\gamma_2 = 2\omega_0 \beta' ,$$

$$f_1 = -\pi F \omega_0 \beta(\mu_0) e^{-\tau/\mu_0} ,$$

$$f_2 = \pi F \omega_0 [1 - \beta(\mu_0)] e^{-\tau/\mu_0} .$$

(37)

and

$\beta'$  = backscatter fraction for isotropically  
incident radiation (Wiscombe and Grams, 1976)

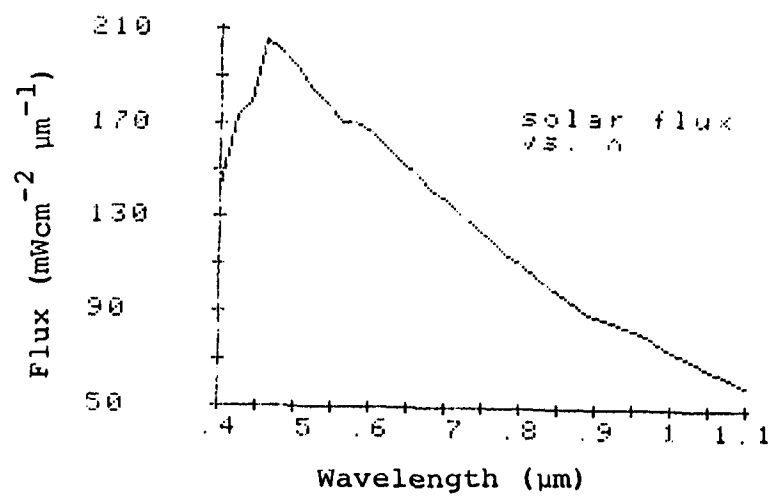


Figure 21  
Solar Flux (Thekaekara et al., 1969)

$\beta(\mu)$  = backscatter fractions for monodirectionally  
 $\beta(\mu_0)$  incident radiation (Wiscombe and Grams, 1976)

The backscatter fractions defined above result from angular integration over the phase function in Equation (34) and are dependent on the asymmetry parameter ( $g$ ) for the specific wavelength under consideration. Figure 22 illustrates the dependence of both  $\beta'$  and  $\beta(\mu)$  on asymmetry parameter. Generally  $\beta'$  varies from 0.5 for isotropic or Rayleigh scattering ( $g=0$ ) to 0.0 for total forward scattering ( $g=1.0$ ) [i.e. there is no backscatter.] The range of  $\beta(\mu)$  values is similar, however, the rate of change in the domain  $0.0 \leq g \leq 1.0$  is dependent on the specific value of  $\mu$  ( $= \cos\theta$ ) chosen.

Equation (35) is subject to the boundary conditions:

$$\begin{aligned} F^-(\tau = 0) &= 0 \\ F^+(\tau = \tau^*) &= A_L [\pi F \mu_0 e^{-\tau^*/\mu_0} \\ &+ F^-(\tau = \tau^*)]. \end{aligned} \quad (38)$$

where  $A_L$  is the wavelength-dependent surface albedo. For the purpose of this work, the surface has been assumed to be a Lambert reflector with an albedo spectrum taken from Ramsey (1968) [as given in Curran (1972)]. Ocean surface albedo as a function of wavelength is illustrated in Figure 23.

Solutions to (35) have the simple forms:

$$\bar{F} = \bar{A} \exp(k\tau) + \bar{B} \exp(-k\tau) + \bar{C} \exp(-\tau/\mu_0) \quad (39)$$

where  $k$  represents the eigenvalues of (35).



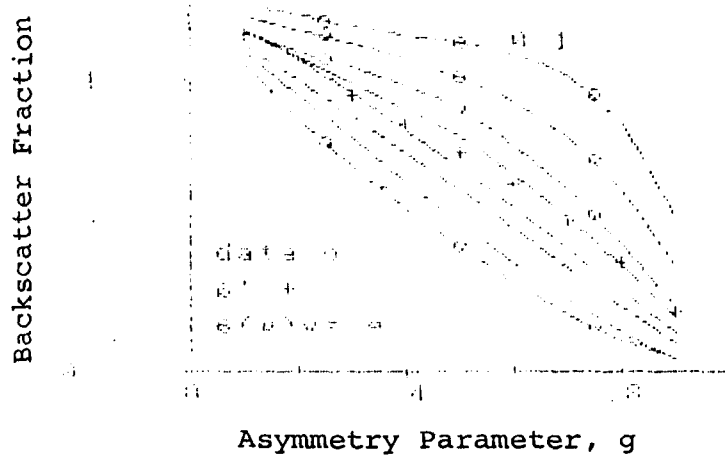


Figure 22

Backscatter Fractions as a Function  
of Asymmetry Parameter  
(Wiscombe and Grams, 1976)

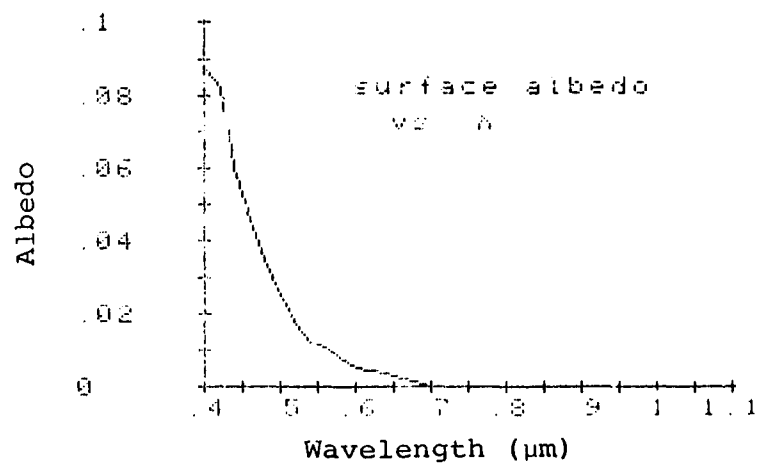


Figure 23  
Ocean Surface Albedo  
(Ramsey, 1968)

The zenith angle dependent radiances  $I^{\pm}(\tau, \mu, \phi)$  will satisfy:

$$\tilde{L}\tilde{I} = -\frac{\omega_0}{\pi} \tilde{C}\tilde{F} - \frac{F}{4} e^{-\tau/\mu_0} \tilde{P} \quad (40)$$

where  $\tilde{I} = \begin{bmatrix} I^+ \\ I^- \end{bmatrix}(\tau, \mu, \phi)$

$$\tilde{F} = \begin{bmatrix} F^+ \\ F^- \end{bmatrix}(\tau)$$

$$\tilde{P} = \begin{bmatrix} P(\mu, -\mu_0, \phi) \\ P(\mu, \mu_0, \phi) \end{bmatrix}$$

and the operator  $\tilde{L}$  is given by:

$$\tilde{L} = [\pm\mu \frac{d}{d\tau} - 1] \quad (41)$$

and

$$\tilde{C} = \begin{bmatrix} [1-\beta(\mu)] & \beta(\mu) \\ \beta(\mu) & [1-\beta(\mu)] \end{bmatrix} \quad (42)$$

Equation (40) is subject to boundary conditions derived from (38) namely:

$$I^-(\tau = 0, \mu, \phi) = 0.0 \quad (43)$$

and

$$I^+(\tau = \tau^*, \mu, \phi) = F^+(\tau = \tau^*)/\pi \quad (44)$$

Solutions to (40) have the simple form:

$$\begin{aligned} \tilde{I} = & \tilde{D} \exp(\pm\tau/\mu) + \frac{\tilde{U} \exp(k\tau)}{(1 - \mu k)} + \frac{\tilde{V} \exp(-k\tau)}{(1 + \mu k)} \\ & + \frac{\tilde{W} \exp(-\tau/\mu_0)}{(1 + \mu/\mu_0)} \end{aligned} \quad (45)$$

where  $\bar{D}$ ,  $\bar{U}$ ,  $\bar{V}$ ,  $\bar{W}$  are analytical, algebraic functions of the input variables.

A variety of comparisons with exact and numerical results have been made to quantify the accuracy of this simple analytical approach. Table 10 summarizes a comparison between the two-stream model and exact results for isotropic scattering obtainable using Chandrasekhar's X and Y functions tabulated in Carlstedt and Mullikin (1966). It is particularly notable that errors are less than 5% over much of this domain, and particularly for emergent intensities with zenith angles approaching unity ( $\mu \rightarrow 1.0$ ). This geometry simulates a nadir-pointing satellite.

Analogous results for Rayleigh scattering are provided in Table 11. In this case, the solar zenith angle is fixed at  $57^\circ$  and the observer zenith at  $13.5^\circ$  to simulate a satellite field of view for a polar-orbiting sensor. Percent errors are given, comparing two-stream results to the exact calculation of Rayleigh scattering by Coulson et al. (1960) for a variety of optical depths, surface albedos of 0.0 and 0.25, and azimuth distances of  $30^\circ$ ,  $90^\circ$ , and  $150^\circ$ . A comparison of these results to the single scattering approximation results in Table 9, indicates that a much higher degree of accuracy is achievable using the two-stream approach.

The most stringent test of an approximate multiple-scattering radiative transfer model is highly anisotropic aerosol scattering. Results of comparison with numerical successive order of scattering approaches (Nagel et al., 1978)

Table 10

	$I^+(\tau=0, \mu)$			$I^-(\tau=\tau^*, \mu)$		
	$\tau^*$			$\tau^*$		
	0.4	1.0	3.5	0.4	1.0	3.5
$\mu$						
0.2	-14.6	2.7	2.7	4.8	1.8	2.5
0.6	-24.8	-4.6	1.8	5.0	2.6	.2
0.9	- 3.0	<.1	1.4	4.9	2.7	-.3

Percent error: Two-stream approximation vs. exact result for isotropic scattering evaluated from Chandrasekhar's X and Y functions. ( $\omega_0=0.5$ ,  $\mu_0=1.0$ )

Table 11

$\tau^*$	$\Lambda_L$	$I^+(\tau=0, \mu, \phi)$			$I^-(\tau=\tau^*, \mu, \phi)$		
		$30^\circ$	$90^\circ$	$150^\circ$	$30^\circ$	$90^\circ$	$150^\circ$
.05	0.0	-10	-5	-1	4	4	3
	0.25	-1	0	0	3	3	2
.10	0.0	6	-2	1	6	5	4
	0.25	-1	-1	0	5	4	3
.25	0.0	-2	2	5	9	7	6
	0.25	-1	0	2	7	6	4
.50	0.0	0	4	8	10	7	4
	0.25	-1	2	4	8	6	4

Percent Error: Two-stream approximation vs. exact result  
for Rayleigh scattering. ( $\mu=.98$ ,  $\mu_0=.60$ )

essentially verify (Kaufman, 1979) accuracy on the order of 6-18% for the near zenith observation angles characteristic of many polar-orbiting satellites. Accuracy for these cases degrades to unacceptable levels for solar or observer zenith angles near the horizon. However, for non-terminator solar illumination conditions, the two-stream approach should provide a practically useful remote sensing analysis tool.

#### 6.5 Ensemble Atmosphere Optical Properties

The total optical depth,  $\tau^*$ , single scatter albedo,  $\omega_0$ , and scattering asymmetry parameter,  $g$ , (which determines the backscatter fractions, see Figure 22) used in solving equations (35) to (45) are derived from the wavelength and meteorologically dependent atmospheric optical properties discussed previously (see Figure 2). These ensemble atmospheric optical properties are given by:

$$\tau^*(\lambda) = \tau_R^S(\lambda) + \tau_g(\lambda) + \tau_1^e(\lambda) + \tau_2^e(\lambda) \quad (46)$$

$$\omega_0(\lambda) = \left[ \tau_R^S(\lambda) + \tau_1^S(\lambda) + \tau_2^S(\lambda) \right] / \tau^*(\lambda) \quad (47)$$

$$g(\lambda) = \frac{\tau_1^S(\lambda)g_1(\lambda) + \tau_2^S(\lambda)g_2(\lambda)}{\tau_R^S(\lambda) + \tau_1^S(\lambda) + \tau_2^S(\lambda)} \quad (48)$$

where  $g_1$  and  $g_2$  are asymmetry parameters for the accumulation and coarse modes, respectively. The optical depths are those for Rayleigh scattering [ $\tau_R^S$ ; eqn.(4)], gaseous absorption [ $\tau_g$ ; eqn.(6)], and aerosol extinction ( $\tau_{1,2}^e$ ) and scattering ( $\tau_{1,2}^S$ ) for the accumulation and coarse modes respectively [eqn. (32)]. Eqn. (48)

represents a weighting of the respective Rayleigh and aerosol scattering phase function with  $g(\text{Rayleigh}) = 0.0$ .

#### 6.6 DMSP Bandpass Weighted Radiances

The solution to equation (45) for each set of meteorological variables investigated provides a wavelength-dependent intensity spectrum,  $I(\lambda)$ . The intensity measured by the DMSP sensor at the satellite,  $\bar{I}(\text{DMSP})$ , however, is given by weighting these monochromatic intensities by the DMSP spectral bandpass function given in Figure 1 according to:

$$\bar{I}(\text{DMSP}) = \int_{\Delta\lambda} \phi(\lambda) I(\lambda) d\lambda \quad (49)$$

where  $\phi$  is the sensor response function over wavelength interval  $\Delta\lambda$  (0.4-1.1  $\mu\text{m}$  for DMSP VHR, LF). (See Figure 1.)



## 7. DISCUSSION OF RESULTS

### 7.1 Scope

In support of the objectives of this study, the sensitivity of DMSP incident radiances in the 0.4-1.1  $\mu\text{m}$  spectral region to variations in meteorological variables (see Table 1) was investigated by performing approximately 3600 individual calculations employing the technical approach summarized in Figure 2 and described in Sections 3 to 6. These results include both wavelength-dependent, simulated radiance spectra,  $I(\lambda)$ , and DMSP-weighted radiance,  $\bar{I}$  (DMSP). A discussion of these results follows.

### 7.2 Maritime Model Geometry

As discussed in §6.4 above, radiance computations are dependent on the relative sun/sensor geometry through various backscatter fractions and the composite angular scattering (phase) function of the atmosphere. For the purpose of this study these geometric factors were deemphasized in favor of the meteorological dependences of the results. Figures 24 and 25, however, illustrate the dependence of radiances on solar zenith angle cosine  $\mu_0$  ( $= \cos \theta_0$ ) and relative azimuth angle, respectively. The model atmosphere is the maritime model with RH = 80% and a scale height of 1.2 km. A nadir viewing sensor ( $\mu=1.0$ ) is assumed. Results in Figure 24 indicate a general increase in radiances when the sun is closer to the zenith position

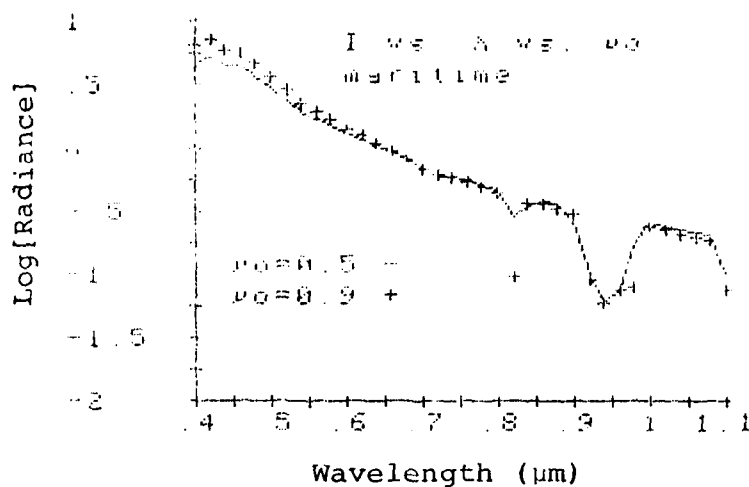


Figure 24

Dependence on Solar Zenith Angle  
(Maritime Model,  $H = 1.2$  km,  $RH = 80\%$ )

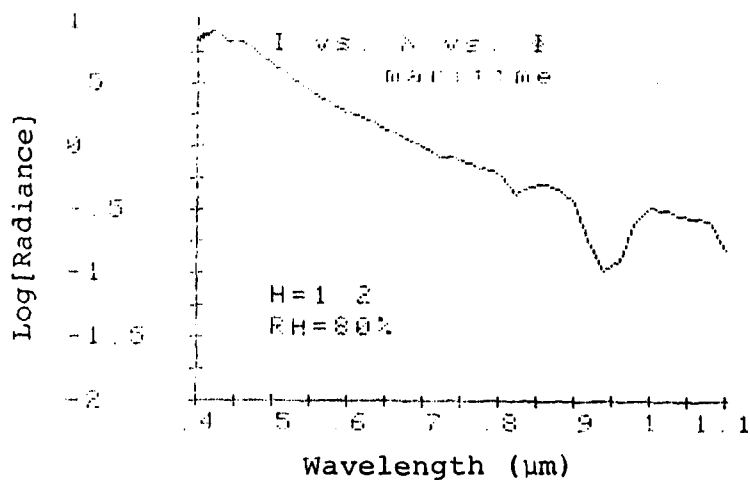


Figure 25

Dependence on Azimuth Angle  
(Maritime Model,  $H = 1.2$  km,  $RH = 80\%$ )

$(\mu_0=1.0)^+$ . Since this effect is dependent on optical depth, it is enhanced toward shorter wavelengths where molecular scattering is important. Since most of the available solar radiation is at shorter wavelengths (see Figure 21), DMSP radiances are increased by this effect.

Since the general spectral features of the radiances in Figure 24 are not markedly different for the two cases, subsequent calculations assume  $\mu_0=0.5$ .

Radiances for a nadir viewing instrument ( $\mu=1.0$ ) are independent of azimuth angle difference  $(\phi-\phi_0)$  [see definitions related to equations (33) and (34)]. For off-nadir ( $\mu \neq 1.0$ ) positions within the sensor scan, radiances may vary with azimuth angle. In Figure 25, a sensor zenith angle of about  $37^\circ$  ( $\mu=0.8$ ) is assumed and azimuth angles of  $0, 45, 90, 135$ , and  $180^\circ$  are evaluated for a solar zenith angle cosine of 0.8. The five curves are generally coincident except for a small region in the vicinity of  $0.4 \mu\text{m}$ . These calculations indicate that DMSP radiances are approximately independent of azimuth angle difference.

### 7.3 Maritime Model Surface Albedo

The Lambert surface albedo assumption adopted in the radiative transfer theory boundary conditions [equation (38)] ignores the possibilities of surface albedo enhancement

---

+Note: The solar zenith angles in Figure 24 are  $\theta_0 = \cos^{-1} \mu_0$  or  $60^\circ$  and  $25.8^\circ$  for  $\mu_0 = 0.5$  and  $0.9$ , respectively.

due to sun glitter on a wind-ruffled ocean (Guinn et al, 1979) or decreases due to subsurface absorption by biological materials such as phytoploukton (Curran, 1972). These effects were parametrically investigated by varying the assumed ocean surface albedo (see Figure 23) with multiplicative factors of 0.0, 0.5, 1.0, 1.5, and 2.0, where 1.0 represent the assumed surface albedo and 2.0 an increase by a factor of 2.0. These results are illustrated in Figure 25(a). It is noteworthy that any variations in surface albedo affect only the visible portion ( $\lambda < 0.7\mu\text{m}$ ) of DMSP incident radiances.

Increased surface albedos increase radiances from 0.4-0.7  $\mu\text{m}$  [Figure 25(b)] although the effect is not linearly dependent on the surface albedo. Bandpass-weighted calculations corresponding to those in Figures 25(a) and (b) indicate a 20% enhancement in radiance for a change from zero albedo to 2.0 times the assumed value.

#### 7.4 Maritime Model - Scale Height and Relative Humidity Dependence

A fundamental objective of this study was to present an internally consistent picture of simulated radiance dependence on relative humidity including the effects of both water vapor absorption and aerosol growth. Figures 26(a) - (d) present the results of calculations illustrating the dependence of the maritime aerosol model ( $N=4000\text{ cm}^{-3}$ ) on relative humidity for assumed scale heights of 0.5, 1.0,

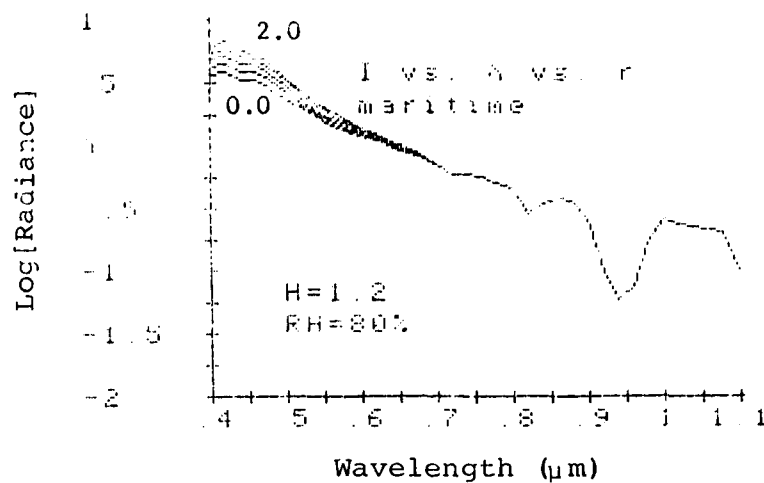


Figure 25(a)

Dependence on Surface Albedo  
(Maritime Model,  $H = 1.2 \text{ km}$ ,  $RH = 80\%$ )

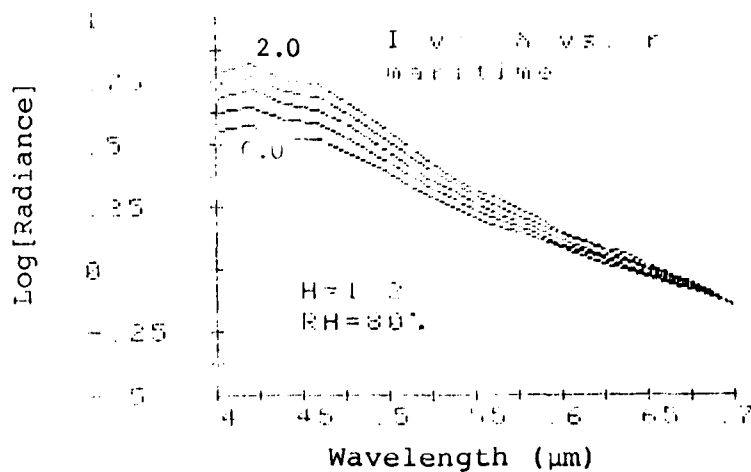


Figure 25(b)

Dependence on Surface Albedo  
in the Visible Region

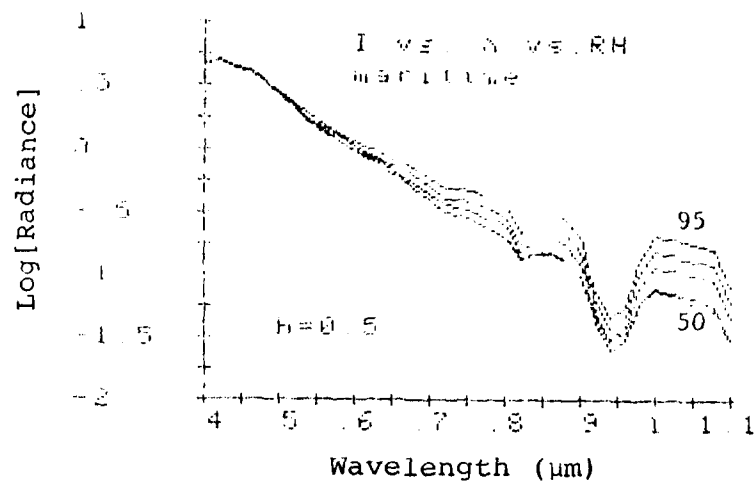


Figure 26(a)  
Dependence on Relative Humidity  
(Maritime Model,  $H = 0.5$ )

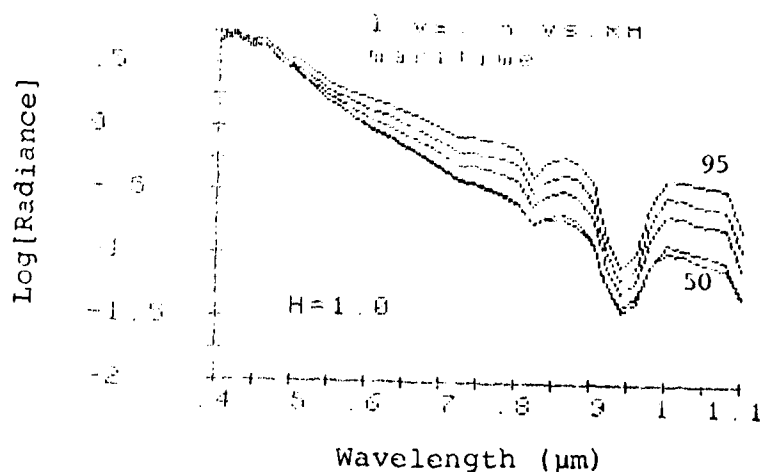


Figure 26(b)  
Dependence on Relative Humidity  
(Maritime Model,  $H = 1.0$ )

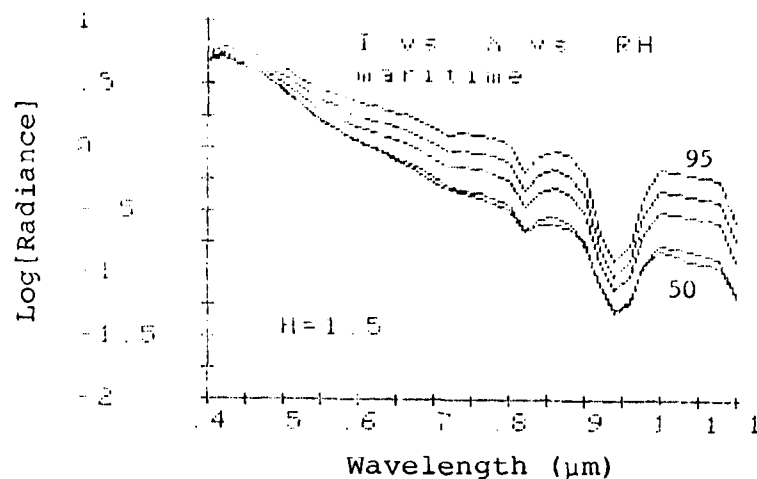


Figure 26(c)

Dependence on Relative Humidity  
(Maritime Model,  $H = 1.5$ )

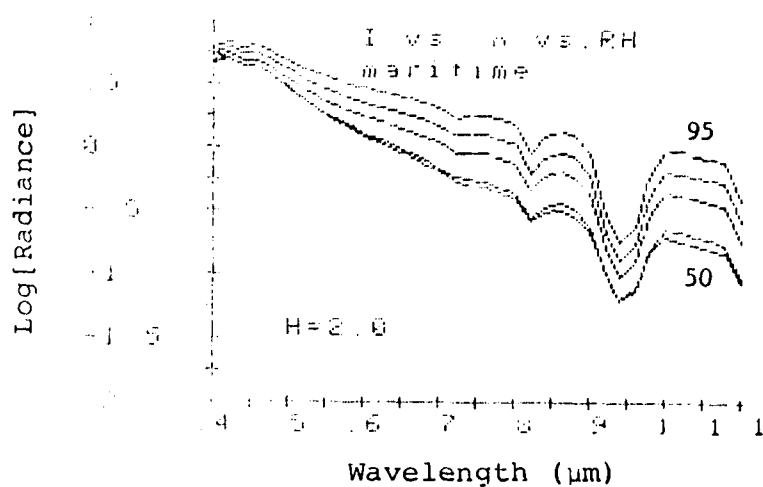


Figure 26(d)

Dependence on Relative Humidity  
(Maritime Model,  $H = 2.0$ )

1.5, and 2.0 km, respectively<sup>+</sup>. Each figure consists of five curves corresponding to 50,70,80,90, and 95% relative humidity. For the fixed number density above, surface visual ranges in the modeled situations vary with relative humidity according to Table 7.

An apparent feature of these results is the marked increase of simulated radiances in the near infrared window regions (see §3.2) with increases in relative humidity. In contrast, this response is much less evident at visible wavelengths. For example, assuming a scale height of 0.5 [Figure 26(a)], the ratio of simulated intensities for relative humidities of 95 (visual range, 8.7 km) and 50% (visual range, 39.6 km) is near unity at 0.55  $\mu\text{m}$ , while it is about 2.8 near 1.0  $\mu\text{m}$ . This corresponds to an approximate 28% increase in bandpass-weighted DMSP radiance for the transition from 50 to 95% relative humidity. These results are in qualitative agreement with those discussed in Fett and Isaacs (1979). As scale height increases, there is a corresponding increase in radiances throughout the DMSP spectral interval. For a fixed relative humidity of 80%, for example, a scale height increase from 0.5 to 2.0 km corresponds to an increase in DMSP bandpass-weighted radiances by a factor of about 2.0.

---

<sup>+</sup>Note: As discussed in §5.4, variations in scale height may also be interpreted as increase in number density (with corresponding changes visual range) for a fixed scale height.



In light of the strong dependence of visual range on relative humidity-dependent aerosol extinction as given by the Koschmieder relation [Equation (30)] applied in Table 7, the apparent insensitivity of simulated emergent visible radiances to changes in relative humidity may be difficult to comprehend. The situation may be partially reconciled by examination of the back scattering geometry considered in the radiative transfer calculation and the angular scattering properties of the aerosols treated in comparison to Rayleigh scattering by gases. While visual range is inversely proportional to the sum of Rayleigh scattering and aerosol extinction coefficients visible radiances are qualitatively dependent on the product of this sum and the appropriate angular scattering function. As described in Section 5, increasing relative humidity implies not only increased aerosol extinction [see Figure 15(a)], but also larger asymmetry parameters [see Figure 15(b)]. Larger asymmetry parameters mean less back scattering to the satellite sensor. At visible wavelengths, the effective angular scattering function (see footnote p. 6-8) or asymmetry factor [Equation (48)] must be weighted to account for both aerosol scattering and Rayleigh scattering. Rayleigh scattering back scatters much more than aerosol scattering at the scattering angles of  $120^\circ$  used here. Therefore, although increases in relative humidity increase aerosol extinction, they decrease the effective magnitude of backscattering due to aerosols and gases. These effects partially compensate for one another in the visible region.

At near infrared wavelengths, however, the influence of Rayleigh scattering is small. Thus, the backscatter is primarily determined by the aerosol angular scattering function and increases in aerosol extinction are directly translated into increased radiances without compensatory decreases in the effective amount of backscatter

#### 7.5 Hybrid Model - Relative Humidity, Wind Speed, and Size Range Dependence

As discussed in §4.3 the hybrid tropospheric-Munn Katz model provides the capabilities to examine dependence of emergent radiances on size range and wind speed in addition to scale height and relative humidity.

##### 7.5.1 Hybrid Model - Accumulation Mode only

One question which arose early in this study concerns the relative role of fine (accumulation) mode and coarse mode aerosols in determining wavelength-dependent emergent radiances. In order to address this point, simulations were performed using only the accumulation mode of the adopted hybrid model ( $N=5000\text{cm}^{-3}$ ). These results are presented in Figures 27(a)-(d) as functions of relative humidity (50,70, 80,90,95%) for scale heights of 0.5, 1.0, 1.5, and 2.0 km. Visual ranges corresponding to these relative humidities are given in Table 7. Notable in these figures is the suppressed dependence of accumulation mode aerosols on relative humidity when compared to the bimodal maritime results presented in §7.4. This is particularly true in the near

AD-A093 466

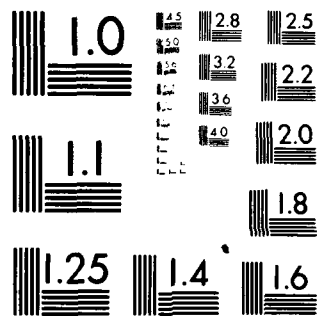
ATMOSPHERIC AND ENVIRONMENTAL RESEARCH INC CAMBRIDGE MA F/6 17/8  
INVESTIGATION OF THE EFFECT OF LOW LEVEL MARITIME HAZE ON DMSP --ETC(U)  
SEP 80 R G ISAACS N00014-80-C-0262

UNCLASSIFIED

NL

2 of 2  
2/2  
2/2


END  
DATE  
FILMED  
2-81  
DTIC



MICROCOPY RESOLUTION TEST CHART  
NATIONAL BUREAU OF STANDARDS-1963-A

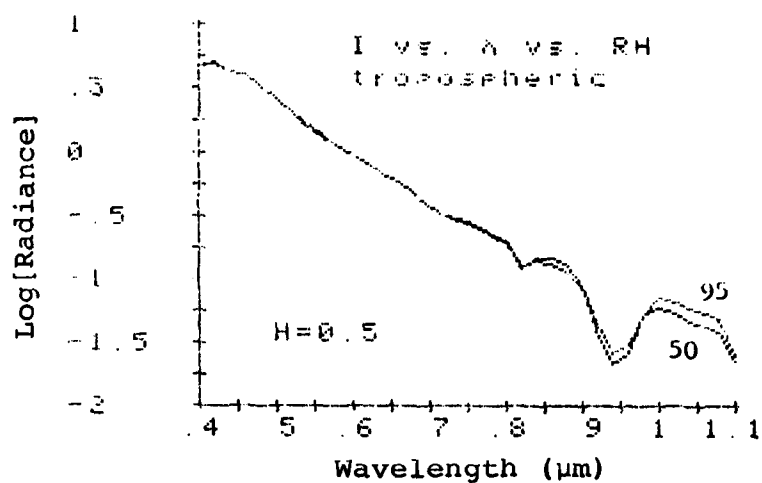


Figure 27(a)  
Dependence on Relative Humidity  
(Tropospheric Model, H = 0.5)

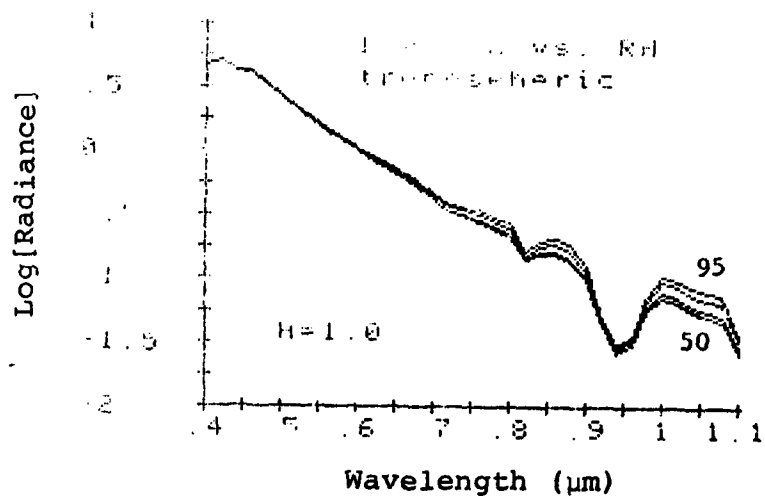


Figure 27(b)  
Dependence on Relative Humidity  
(Tropospheric Model, H = 1.0)

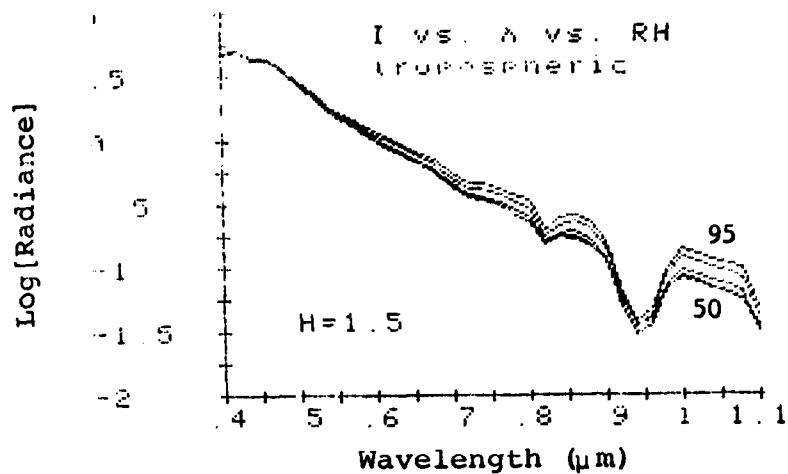


Figure 27(c)

Dependence on Relative Humidity  
(Tropospheric Model, H = 1.5)

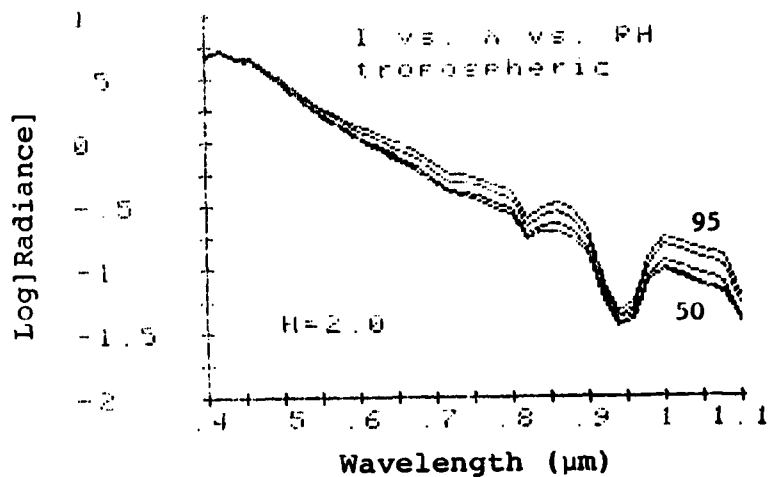


Figure 27(d)

Dependence on Relative Humidity  
(Tropospheric Model, H = 2.0)

infrared window regions. A comparison between corresponding cases illustrated in Figures 26 and 27 suggests that coarse mode aerosols play a predominant role in influencing the dependence of simulated emergent radiances on relative humidity. For moderate relative humidities (i.e. <70-80%), visible radiances are much more dependent on accumulation mode aerosols while near infrared wavelengths are influenced primarily by the coarse mode.

#### 7.5.2 Hybrid Model - Relative Humidity

Figures 28(a)-(d) illustrate the effect of including the coarse mode of the hybrid aerosol model. The accumulation mode is as described above with number densities in the coarse mode determined by relative humidity and wind speed as given in Table 6. The visual ranges corresponding to these meteorological variable for the combined model are given in Table 7. For these cases scale heights are fixed at 1.2 km (H1) for the accumulation mode and 0.8 km (H2) for the coarse mode. Suitable comparisons (H=1.0) are to Figure 26(b) for the maritime model or Figure 27(b) for the accumulation mode only calculation.

Dependence is shown as a function of relative humidity (50,70,80,90,95%) for fixed windspeeds of 0,5,7, and 10  $\text{ms}^{-1}$ , respectively. The influence of coarse mode aerosols on near IR radiances for this model is approximately intermediate between those for either the maritime model (which generally

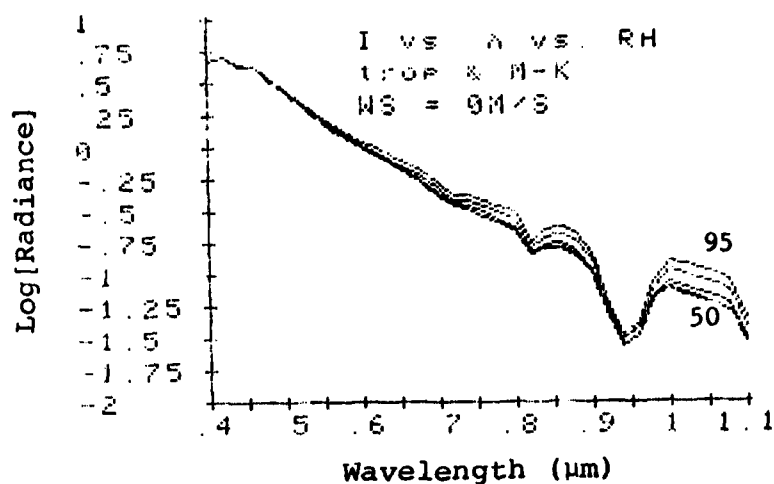


Figure 28(a)

Dependence on Relative Humidity  
(Hybrid Model,  $H_1 = 1.2 \text{ km}$ ,  
 $H_2 = 0.8 \text{ km}$ ,  $WS = 0 \text{ ms}^{-1}$ )

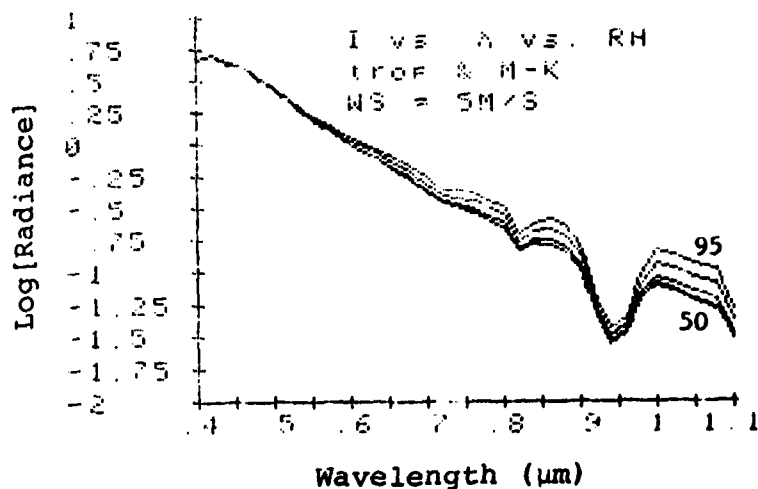


Figure 28(b)

Dependence on Relative Humidity  
(Hybrid Model,  $H_1 = 1.2 \text{ km}$ ,  
 $H_2 = 0.8 \text{ km}$ ,  $WS = 5 \text{ ms}^{-1}$ )



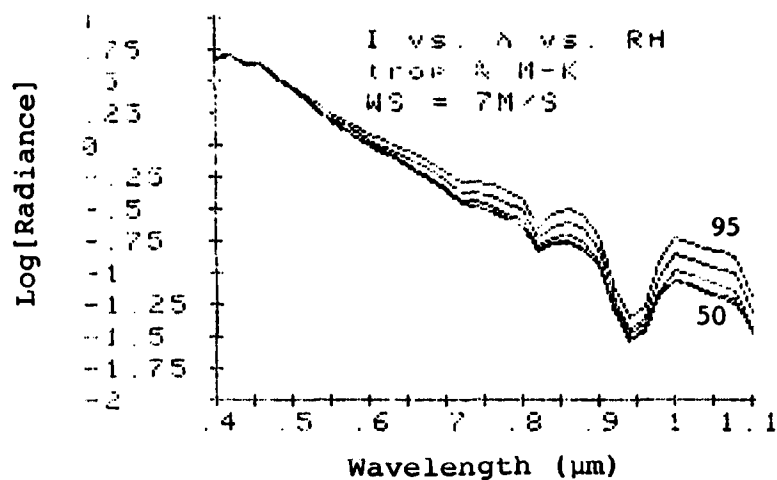


Figure 28(c)

Dependence on Relative Humidity  
(Hybrid Model,  $H_1 = 1.2$  km,  
 $H_2 = 0.8$  km, WS = 7  $\text{ms}^{-1}$ )

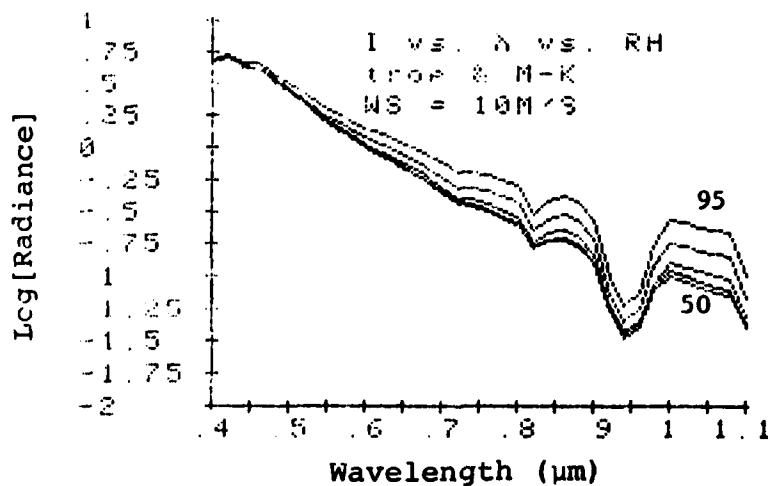


Figure 28(d)

Dependence on Relative Humidity  
(Hybrid Model,  $H_1 = 1.2$  km,  
 $H_2 = 0.8$  km, WS = 10  $\text{ms}^{-1}$ )

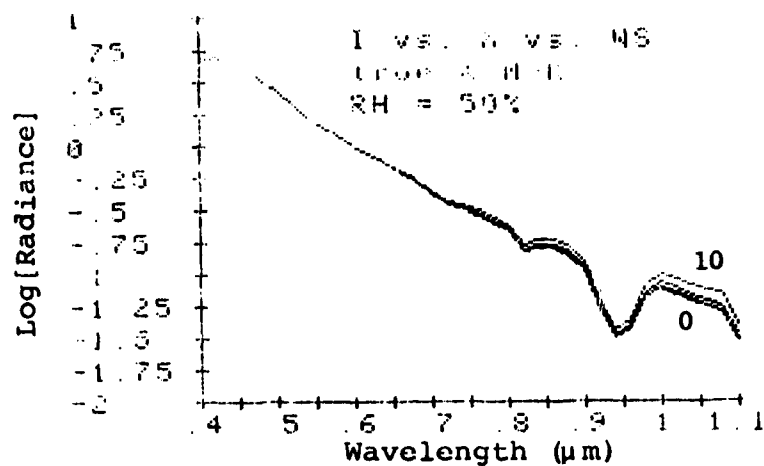
has a higher coarse mode number density) or the tropospheric model (which has no coarse mode). Again, there is very little dependence of visible radiances on relative humidity.

#### 7.5.3 Hybrid Model Wind Speed

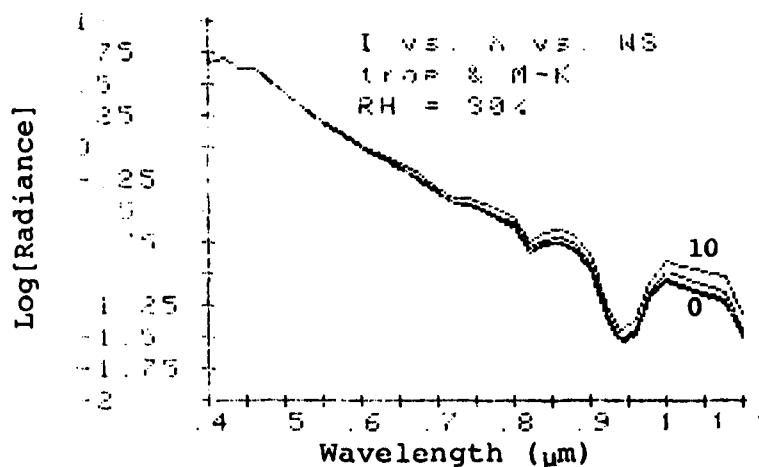
For fixed relative humidities, increases in wind speed enhance simulated radiances particularly in the near IR region. Figure 29(a)-(c) illustrate the dependence of radiance on windspeed for relative humidities of 50, 80, and 95%, respectively. Again, the effect of windspeed is not apparent at visible wavelengths. Figures 28 and 29 collectively suggest that both windspeed and relative humidity are crucial in determining near IR radiances incident on the DMSP sensor.

#### 7.6 Visual Range

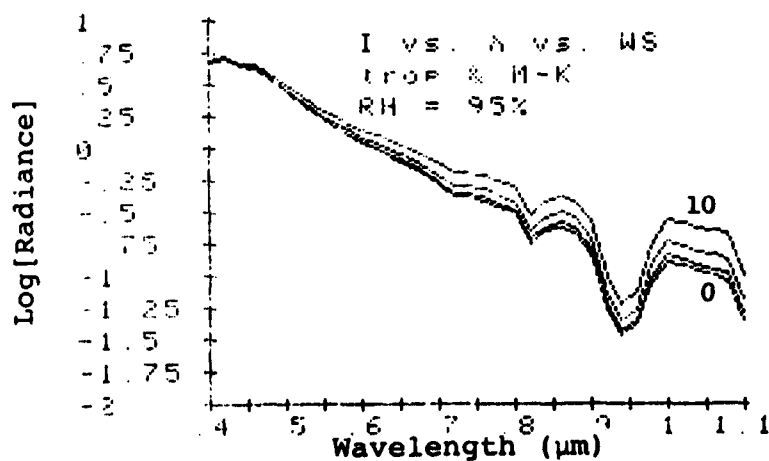
The discussion in §5.3 provides a prescription to adjust number densities in the adopted models to correspond to specific surface visual ranges at fixed relative humidity (and if applicable wind speed). These number densities are summarized in Table 8. Calculations were performed using these values at visual ranges of 5, 10, 23, and 50 km for both the maritime and hybrid models. These results are illustrated in figures 30 and 31, respectively. Results are qualitatively similar, indicating an increase in radiances at all wavelengths between 0.4 and 1.1  $\mu\text{m}$  with a decrease in visual range. Note that visible wavelengths are dramatically



(a) RH = 50%



(b) RH = 80%



(c) RH = 95%

Figure 29

Dependence on Wind Speed  
(Hybrid Model,  $H_1=1.2$  km,  $H_2=0.5$  km)

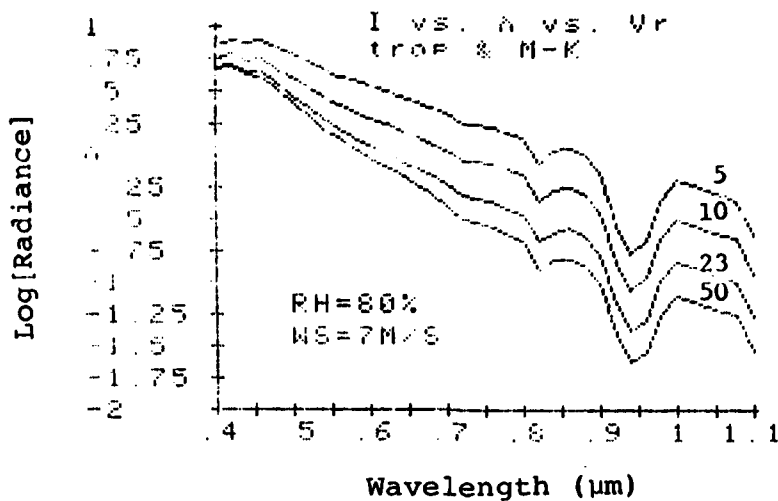


Figure 30

Dependence on Visual Range  
(Maritime Model,  $H = 1.2$  km, RH = 80%)

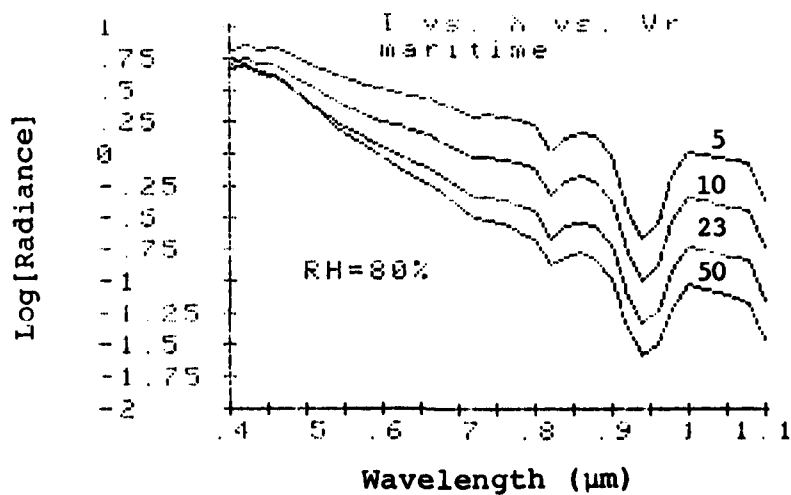


Figure 31

Dependence on Visual Range  
(Hybrid Model,  $H_1 = 1.2$  km,  
 $H_2 = 0.8$  km, RH = 80%, WS = 7  $\text{ms}^{-1}$ )

affected since the number density adjustments cited above are applied to both the accumulation and coarse modes in the maritime model and exclusively to the fine mode in the hybrid model.

#### 7.7 DMSP Bandpass-Weighted Radiances

In the preceeding discussion of results reference was made to DMSP bandpass-weighted radiances. For each of the cases described above, simulated DMSP radiances were evaluated according to the procedure described in §6.6. Plotting these values on a common scale, the sensitivity of simulated DMSP radiances to variations in the meteorological variables discussed above can be demonstrated. These results, although preliminary, also provide potentially useful tools for meteorological analyses which may be developed into user oriented operational nomographs.

##### 7.7.1 Maritime Model

Figure 32, illustrates the dependence of DMSP bandpass-weighted radiances on both relative humidity (RH) and scale height (H) for the maritime model. As previously discussed (§5.4), scale height may act as a surrogate for changes in number density with a fixed scale height. Solid curves represent the variation of radiance with scale height (upper ordinate) for the labeled, fixed relative humidity. Dashed curves present the converse case, that is, variation with relative humidity (lower ordinate) for the labeled,

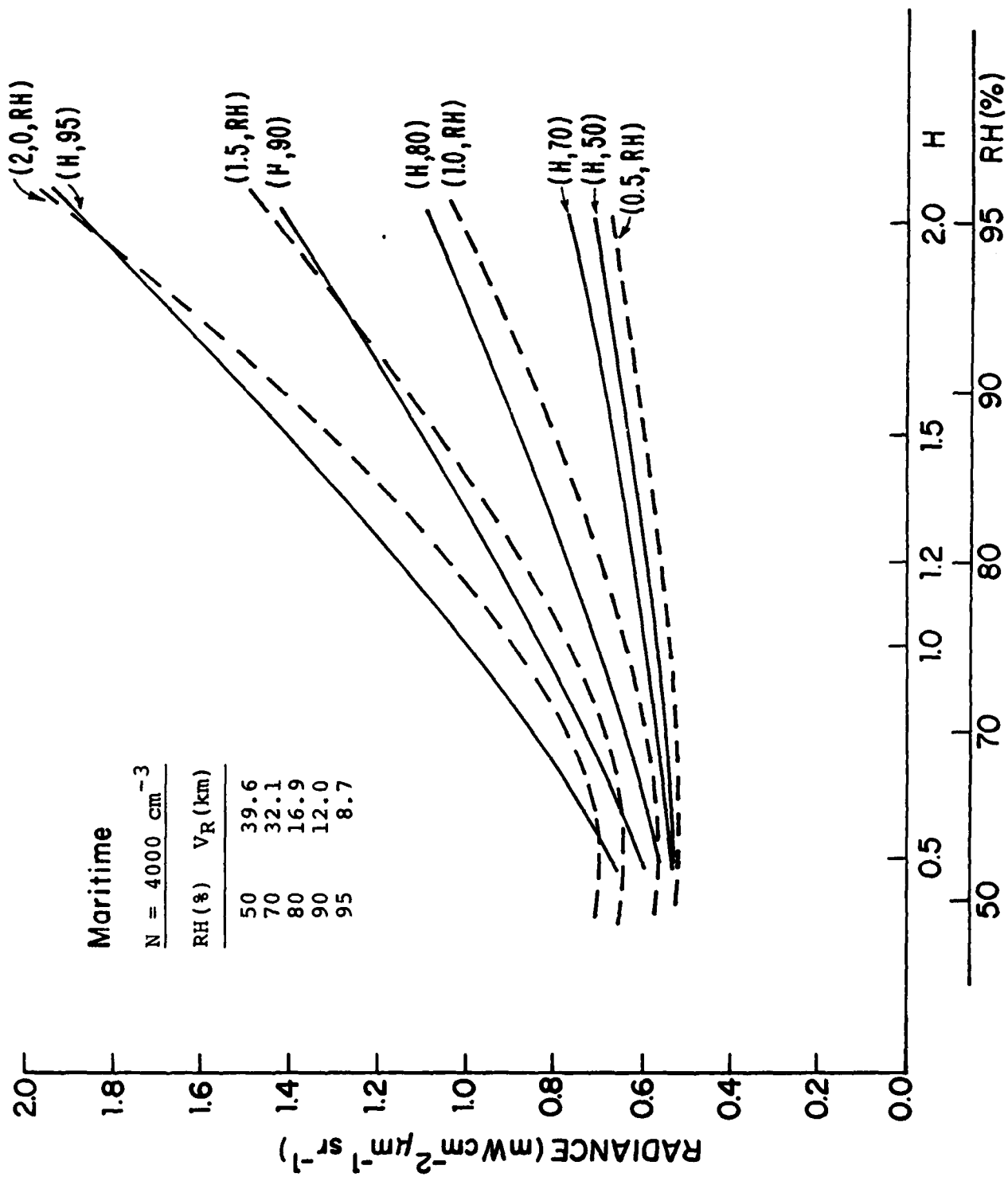


Figure 32  
DMSP Bandpass-Weighted Radiances (Maritime Model)

fixed scale height. As indicated in the figure, a particular DMSP radiance is a multivalued function of relative humidity and scale height. For example, assuming  $I(\text{DMSP}) = 1.0 \text{ mWcm}^{-2} \mu\text{m}^{-1}\text{sr}^{-1}$ , this radiance corresponds to (RH,H) pairs including (95,1.0), (90,1.3), (80,1.8), etc. Therefore, it is unlikely that both values can be uniquely determined from DMSP data alone. However, supporting meteorological data or other remotely sensed data may provide information on either variable. In this case, DMSP radiances can be used to estimate the other. For example, if  $\bar{I}(\text{DMSP}) = 1.0 \text{ mWcm}^{-2} \mu\text{m}^{-1}\text{sr}^{-1}$  and RH=80%, the scale height is about 1.8 km.<sup>+</sup> Furthermore, if it is estimated that the actual scale height is 1.2 km, then there must be about 1.5 (=1.8/1.2) times more aerosol particles present than in the aerosol model (i.e.,  $4000 \text{ cm}^{-3}$ ) or  $6000 \text{ cm}^{-3}$ . For 80% relative humidity, Table 8 suggests a surface visual range of slightly over 10 km.

#### 7.7.2 Hybrid Model

The introduction of wind speed dependence complicates the picture somewhat for the hybrid model, although the basic idea remains the same. Figure 33, illustrates these results with labeled curves corresponding to fine mode scale height (H<sub>1</sub>), the coarse mode scale height is fixed at 0.8 km,

---

<sup>+</sup>Note: Due to the approximate nature of the model used in these calculations, such applications will have computational errors associated with them.

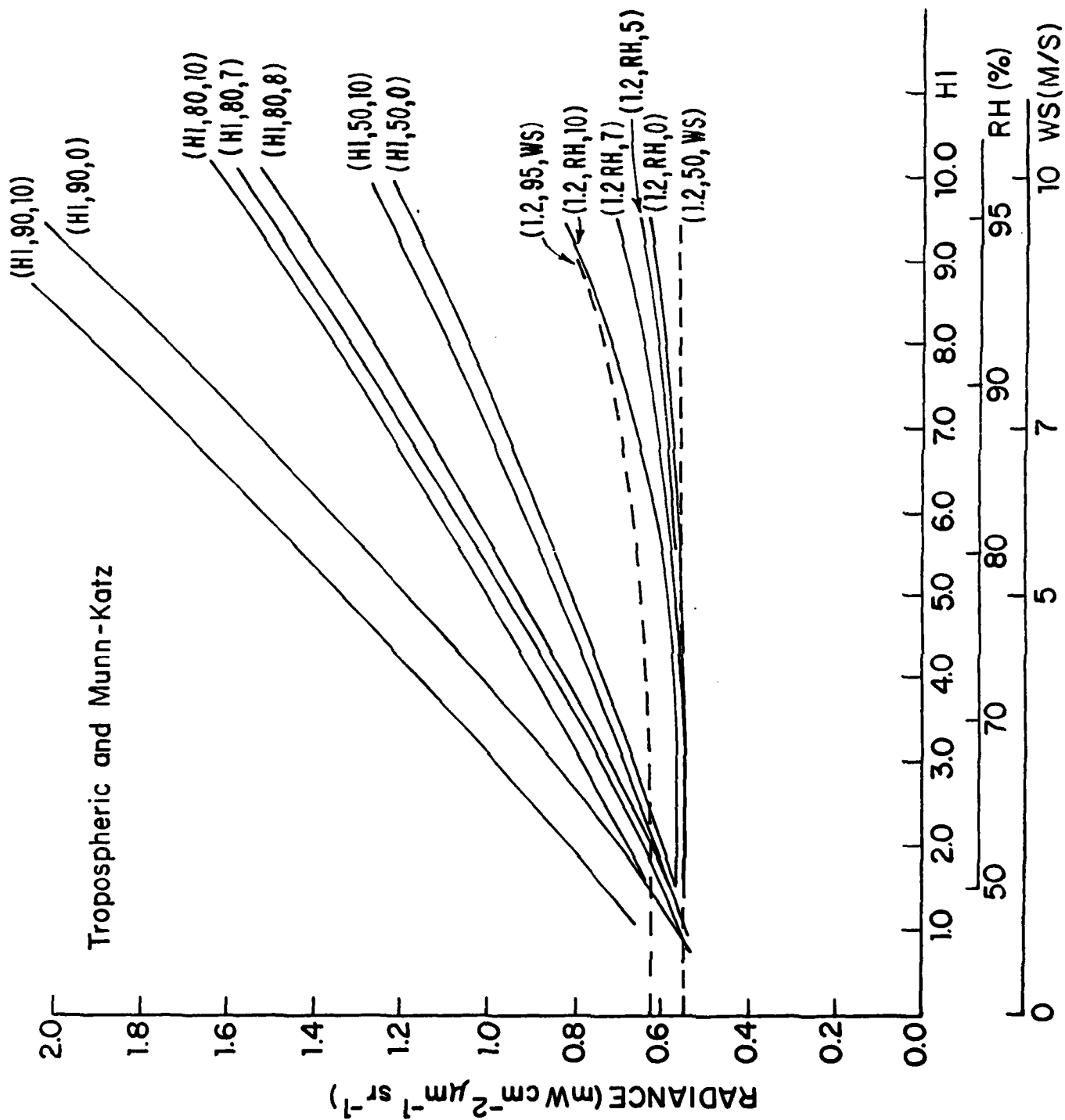


Figure 33  
DMSB Bandpass-Weighted Radiances (Hybrid Model)



relative humidity (RH), and wind speed (WS). For fixed values of two of these variables, the appropriate estimate of the third corresponding to a specific DMSP radiance can be read from the relevant ordinate scale. For example, if  $\bar{I}$  (DMSP) =  $1.0 \text{ mWcm}^{-2} \mu\text{m}^{-1} \text{sr}^{-1}$ , and RH=90%, WS=0, one obtains  $H1 \sim 3.8 \text{ km}$ . Again this may be interpreted as a measure of number density in the fine mode for a given scale height.

## 8. SUMMARY OF RESULTS

This report has described the technical approach, development, and implementation of a model to relate simulated satellite incident radiances (in the wavelength region from 0.4 to 1.1  $\mu\text{m}$ ) to variations in meteorological variables such as relative humidity, windspeed, aerosol number density, visual range, and aerosol scale height. In this context, the results of this effort may be considered an extension of existing optical propagation models capable of relating remotely-sensed and insitu optical transmission data bases.

Technical elements treated in this investigation included: (1) calculation of non-aerosol atmospheric transmission properties (Rayleigh scattering and gaseous absorption), (2) implementation of physical aerosol models describing dependence of size distribution and index of refraction on aerosol growth and wind speed dependence of aerosol oceanic components, (3) calculations of maritime aerosol optical properties using Mie theory and, (4) incorporation of the above in an efficient radiative transfer calculation. The model was exercised to provide sensitivity analyses of both wavelength-dependent and DMSP bandpass weighted radiance to the meteorological variables cited above.

## 9. CONCLUSIONS AND RECOMMENDATIONS

### 9.1 Conclusions

A number of conclusions emerge based on the results reported in Section 7.

- . Calculations using both the maritime and hybrid aerosol models indicate that simulated emergent radiances in the near infrared window regions ( $\lambda > 0.7 \mu\text{m}$ ) are highly sensitive to the presence of coarse mode (oceanic origin) particulates.
- . Enhanced radiances in these regions are indicated for increasing relative humidity and windspeed, primarily due to the characteristically greater aerosol growth for these large particles and the mechanical addition of particles due to wind mixing.
- . Results from the hybrid model indicate that the near infrared effect is enhanced when higher wind speeds and relative humidity occur concurrently.
- . The dependence of simulated radiances in the visible spectral region ( $\lambda < 0.7 \mu\text{m}$ ) on these factors, by contrast, is significantly less than that evidenced at larger wavelengths. At these shorter wavelengths radiances appear to be determined primarily by Rayleigh scattering and accumulation mode aerosols.
- . Calculations suggest that the DMSP sensor is capable of delineating reduced visibility situations due to

the dependence of visual range on the number density of accumulation mode aerosols. However, a quantification of the relationship between DMSP radiances and surface visual range requires independent knowledge of other variables such as relative humidity and fine mode aerosol scale height.

- . For fixed relative humidities and wind speeds (if applicable), wavelength-dependent, simulated radiances generally increase with aerosol scale height. Variation with relative humidity and wind speed are enhanced with increases in aerosol scale height.
- . The effect of water vapor on remote sensing within this spectral range cannot be ignored outside the water vapor absorption bands due to its coupling through aerosol growth laws with aerosol continuum scattering elsewhere.
- . Variations in ocean surface albedo appear to affect only simulated visible wavelength radiances.
- . The dependence of simulated DMSP bandpass-weighted radiances on the meteorological variables discussed above suggests that the sensor may be used to provide correlating evidence to characterize the meteorological situation within the field of view, given that some of the relevant variables are available independently from surface observations or other satellite sensors. Standing alone, the DMSP sensor cannot uniquely characterize the meteorological variables treated above.

## 9.2 Recommendations

The results of this study may potentially provide an economical tool to assess the effects of meteorological variables on remotely sensed radiances in the visible and near infrared portion of the spectrum. A broader application than the present study concerning the DMSP sensor may be envisioned by examining other spectral regions and incorporating other relevant bandpass functions. These ambitious goals should be undertaken with great caution, however, until a number of matters arising from the present study are resolved.

A variety of recommendations can be made concerning the physical elements of the modeling approach adopted. These include: (1) examination of other aerosol growth laws and physical models, (2) implementation of a surface albedo model coupling surface windspeed to sun glitter effects, and (3) improved treatments of radiative transfer. As a minimal requirement, with respect to the last item, results reported here should be compared with more accurate, numerical radiative transfer treatments run with the same data set of optical parameters to better quantify errors associated with the approximate method adopted.

This study was conceived and initiated as a theoretical, modeling exercise. The utility of the approach presented and the validity of the results reported must be verified by conducting a validation study based on an appropriate set of field data including aerosol optical and physical

parameters, meteorological variables, and, if possible, concurrent remotely-sensed radiances.

## 10. ACKNOWLEDGEMENTS

The author wishes to thank Mr. R. Fett and Dr. A. Goroch of the Naval Environmental Prediction Research Facility and Dr. E. Shettle of the Air Force Geophysics Laboratory for helpful discussions during the course of this work. The programming support of Mr. R. Specht at AER is gratefully acknowledged. Administrative assistance was kindly provided by W. Martin of the Office of Naval Research.

## 11. REFERENCES

- Abhyankar, K.D., Fymat, A.L., (1971) Tables of Auxiliary Functions for Non-Conservative Rayleigh Phase Matrix in Semi-Infinite Atmospheres, Astroph. J. Supplement Series. No. 195, 23, 35-192.
- Angstrom, A. (1961) Techniques of Determining the Turbidity of the Atmosphere. Tellus 13, 214-223.
- Barnes, J.C., R.G. Isaacs, C.J. Bowley and A.J. Bussey (1978) Comparative Study of Anomalous Gray Shade Patterns in DMSP and LANDSAT Imagery. ERT No. P 3469 F, Concord, MA.
- Braslau, N. and J.V. Dave (1973a) Effect of aerosols on the transfer of solar energy through realistic model atmospheres. Part I: Non-absorbing aerosols. J. Appl. Meteor., 12, 601.
- Braslau, N. and J.V. Dave (1973b) Effect of aerosols on the transfer of solar energy through realistic model atmospheres. Part II: Partly absorbing aerosols. J. Appl. Meteor., 12, 616.
- Burke, H.H., and N.D. Sze, (1977) A comparison of variational and discrete ordinate methods for solving radiative transfer, J. Quant. Spectrosc. Radiat. Transfer, vol. 17, 783-793.
- Carlstedt, J.L., T.W. Mullikin, (1966) Chandrasekhar's X and Y Functions, Astroph. J. Suppl. 12, No. 113, 449.
- Chandrasekhar, S., (1950) Radiative Transfer, Oxford University Press, reprinted by Dover Publications 1960.
- Chu, C.M., S.W. Churchill, (1955) Numerical Solution of Problems in Multiple Scattering of Electromagnetic Radiation, J. Phys. Chem., 59, 855-863.
- Coakley, J.A., Jr., and P. Chylek, (1975) The two-stream approximation in radiative transfer: Including the angle of the incident radiation, J. Atmos. Sci., 32, 409-418.
- Coulson, K.L., J.V. Dave, Z. Sekera, (1960) Tables Related to Radiation Emerging from a Planetary Atmosphere with Rayleigh Scattering, University of Calif. Press.
- Curran, R.J., (1972) Ocean color determination through a scattering atmosphere. Appl. Opt., 11, 1857-1866.
- Dave, J.V., (1969) Effect of coarseness of the integration increment on the calculation of the radiation scattered by polydispersed aerosols. Appl. Opt., 8, 1161-1167.



- Dave, J.V., (1970) Subroutines for Computing the Parameters of the Electromagnetic Radiation Scattered by a Sphere. IBM System 360 Program 3600-17.4.002.
- Deirmendjian, D., (1969) Electromagnetic Scattering on Spherical Polydispersion, New York Elsevier Publ.
- Dennis, R., (1976) Handbook on Aerosols. ERDA. NTIS TID-26608.
- Edlen, B. (1966) Metrologia 2, 12.
- Elterman, L. (1970) Vertical-Attenuation Model with Eight Surface Meteorological Ranges 2 to 13 kilometers. AFCRL-70-0200.
- Fett, R.W., and R.G. Isaacs (1979) Concerning Causes of "Anomalous Gray Shades" in DMSP Visible Imagery. J. Appl. Meteor., 18, 1340.
- Fett, R.W., and W.F. Mitchell (1977) Navy Tactical Applications Guide: Vol. 1, Technique and Applications of Image Analysis (DMSP). NEPRF Applications Report 77-03. Tactical Applications Department, NEPRF, Monterey, CA.
- Fitzgerald, J.W., 1975: Approximation formulas for the equilibrium size of an aerosol particle as a function of its dry size and composition and the ambient relative humidity. J. Appl. Meteor., 14, 1044-1049.
- Fitzgerald, J.W., (1979) On the Growth of Aerosol Particles with Relative Humidity, NRL Memorandum Report 3847, Naval Research Laboratory, Washington, D.C.
- Goody, R.M., (1964) Atmospheric Radiation: I. Theoretical Basis. Oxford University, 436.
- Gomez, R.B. and L.D. Duncan (1978) Description of the Atmospheric Sciences Laboratory smoke obscuration model (ASLSOM). The Technical Cooperation Program Symposium on Smoke and Adverse Weather Effects on Electro-Optical Systems, Malvern, England, May 22-23, 1978.
- Guinn, J.A., Jr., G.N. Plass, and G.W. Kattawan (1979) Sunlight glitter on a wind-ruffled sea: further studies. Appl. Opt. 18, 6, 842-849.
- Hale, George M., and Querry, Marvin R. (1973) Optical constants of water in the 200-nm to 200  $\mu$ m wavelength region, Appl. Opt. 12:555-563.
- Hanel, G., (1968) The real part of the mean complex refractive index and the mean density of samples of atmospheric aerosol particles. Tellus, 20, 371.
- Hanel, G., (1972) Computation of the extinction of visible radiation by atmospheric aerosol particles as a function of the relative humidity based upon measured properties. Atmos. Environ., 3, 377.

- Hansen, J.E., (1969) Absorption Line Formation in a Scattering Planetary Atmosphere: A Test of van de Hulst's Similarity relations, Astroph. J. **158**, 337-349.
- Hansen, J.E., and L.D. Travis, (1974) Light Scattering in Planetary Atmospheres. Space Sci. Rev., **16**, 527-610.
- Horvath, H. and K.E. Noll (1969) The Relationship Between Atmospheric Light Scattering Coefficient and Visibility. Atmos. Env. **3**: 543-552.
- Hughes, H.G. and J.H. Richter (1979) Extinction coefficients calculated from aerosol size distributions measured in a marine environment. Atmos. Effects on Radiat. Trans., SPIE **195**, 39.
- Irvine, W.M., (1965) Multiple Scattering by Large Particles, Astroph. J. **142**, 1563-1575.
- Joseph, J.H., W.Wiscombe, and J. Weinman, (1976) The delta-Eddington approximation for radiative flux transfer, J. Atmos. Sci. **33**, 2452-2459.
- Junge, C.E., (1960) "Aerosols", in Handbook of Geophysics, Revised edition, MacMillan, N.Y.
- Junge, C.E., (1963) Air Chemistry and Radioactivity, 382., Academic Press, New York.
- Junge, C.E., and E. McLaren, (1971) Relationship of cloud nuclei spectra to aerosol size distribution and composition. J. Atmos., **28**, 382-390.
- Junge, C.E., (1972) Our knowledge of the physico-chemistry of aerosols in the undisturbed marine environment. J. Geophys. Res., **77**, 5183-5200.
- Kaufman, Y.J. (1979) Effect of the Earth's Atmosphere on Contrast for Zenith Observations. J. Geophys. Res., **84**, C6, 3165-2451.
- Kohler, H. (1926) Zur Thermodynamik der Kondensation an Hygroskopischen Kernen und Bemerkungen über das Zusammenfließen der Tropfen, Meddelande from Statens Meteorologiska-Hydrologiska Anstalt, Band 3, no 8, Stockholm.
- Kolesov, A.K., (1972) Reflection and Transmission of Light by a Semi-Infinite Atmosphere for Anisotropic Scattering, Trudy Astron. Obs. Leningrad God. Univ. **29**.
- Koschmieder, H., (1924). Theorie der Horizontalen Sichtweite. Beitr. Phys. Atmos. **12**:171.
- Lenoble, J., (1970) Importance de la polarisation dans le Rayonnement Diffuse par une Atmosphere Planetaire, J. Quant. Spectro. Radiat. Trans. **10**, 533.

- Lenoble, J. (1977) Standard Procedures to Compute Atmospheric Radiative Transfer in a Scattering Atmosphere. IAMAP, Boulder, CO.
- Liou, K.N. (1973) A numerical experiment on Chandrasekhar's discrete-ordinate method for radiative transfer: Applications to cloudy and hazy atmospheres, J. Atmos. Sci., 30, 1303-1326.
- Liou, K.N. (1974) Analytic two-stream and four-stream solutions for radiative transfer, J. Atmos. Sci., 31, 1473-1475.
- Mason, B.J. (1957) The Physics of Clouds, Clarendon Press.
- McCartney, E.J. (1976) Optics of the Atmosphere: Scattering by Molecules and Particles. J. Wiley, New York.
- McClatchey, R.A., W.S. Benedict, S.A. Clough, D.E. Burch, R.F. Calfee, K. Fox, L.S. Rothman and J.S. Garing (1973) AFRCL Atmospheric Absorption Line Parameters Compilation. AFCL-TR-0096.
- McClatchey, R.A. and A.P. D'Agati (1978) Atmospheric Transmission of Laser Radiation: Computer Code LASER. AFGL-TR-0029.
- Meador, W.E., and W.R. Weaver (1980) Two-Stream Approximations to Radiative Transfer in Planetary Atmospheres: A Unified Description of Existing Methods and a New Improvement., J. Atmos. Sci., 37, 630-643.
- Meszaros, A. and K. Vissy (1974) Concentration, size distributions, and chemical nature of atmospheric aerosol particles in remote oceanic areas. Aerosol Sci. 5, 101-109.
- Mie, G. (1908) Beitrage zur optik trueber medien, speziell kolloidaker metallosunger. Annalen der Physik, 25, 377.
- Nagel, M.R., H. Quenzel, W. Kweta, and R. Wendling (1978) Daylight Illumination-Color-Contrast Tables. Academic Press.
- Nilsson, B. (1979) Meteorological Influence on Aerosol in the 0.2-40.0  $\mu$ m wavelength range. Appl. Opt., 18, 3457-3473.
- Penndorf, R. (1957) 'Tables of the Refractive index for standard air and the Rayleigh scattering coefficient for the spectral region between 0.2  $\mu$  and 20.0  $\mu$  and their application to atmospheric optics', J. Opt. Soc. Am. 47, p. 176.
- Pettit, E. (1951) The Sun and Stellar Raiation in Astrophysics, T. Hynek, ed. New York, McGraw-Hill, 703.
- Ramsey, R.C. (1968) Study of the Remote Measurement of Ocean Color, Final Report, TRW, NASW-1658.
- Rothman, L.S. and R.A. McClatchey (1976) Appl. Optics, 15, 2615.

- Sekera, Z., A.B. Kahle (1966) Scattering Functions for Rayleigh Atmospheres of Arbitrary Thickness, Memorandum R-452-PR, The Rand Corporation.
- Selby, J.E.A., F.X. Kneizys, J.H. Chetwynd, Jr. and R.A. McClatchey (1978) Atmospheric Transmittance/Radiance: Computer Code LOWTRAN 4. AFGL-TR-78-0053.
- Selby, J.E.A. and R.A. McClatchey (1972) Atmospheric Transmittance from 0.25 to 28.5  $\mu\text{m}$ : Computer Code LOWTRAN 2. AFCRL-TR-72-0745.
- Selby, J.E.A. and R.A. McClatchey (1975) Atmospheric Transmittance from 0.25 to 28.5  $\mu\text{m}$ : Computer Code LOWTRAN 3. AFCRL-TR-75-0225.
- Selby, J.E.A., E.P. Shettle and R.A. McClatchey (1976) Atmospheric Transmittance from 0.25 to 28.5  $\mu\text{m}$ : Supplement LOWTRAN 3B. AFGL-TR-76-0258.
- Shettle, E.P. and J.A. Weinman (1970) The transfer of solar irradiance through inhomogeneous turbid atmosphere evaluated by Eddington's approximation. J. Atmos. Sci., 27, 1048-1055.
- Shettle, E.P. and R.W. Fenn (1976) Models of the Atmospheric Aerosols and their Optical Properties. AGARD Conference Proceedings No. 183, Optical Propagation in the Atmosphere. Presented at Electromagnetic Wave Propagation Panel Symposium, Lyngby, Denmark, 27-31 October 1975. NTIS Acc. No. N76-29817.
- Shettle, E.P. and R.W. Fenn (1979) Models for the Aerosols of the Lower Atmosphere and the Effects of Humidity Variations on their Optical Properties. AFGL-TR-79-0214 Air Force Geophysics Laboratories, Hanscom AFB, MA.
- Sobolev, V.V. (1956) A Treatise on Radiative Transfer, Gos. Izd. Tekh-Teor. Lit., MOSCOW (Eng. trans. D. Van Nostrand, 1963).
- Stibbs, D.W.M., and R.E. Weir (1959) On the H-Functions for Isotropic Scattering, Month. Nat. R. Astron. Soc. 119, 512.
- Sze, N.D. (1976) Variational Methods in Radiative Transfer Problems. J. Quant. Spectrosc. Radiat. Transfer, Vol. 17, 783-793.
- Thekaekara, M.P., R. Kruger, C.H. Duncan (1969) Appl. Optics 8, 1713.
- Van de Hulst, H.C. (1957) Light Scattering by Small Particles. Wiley, NY.
- Van de Hulst, H.C. and K. Grossman (1968) Multiple Light Scattering in Planetary Atmospheres. The Atmospheres of Mars and Venus, ed. J.C. Brandt and M.B. McElroy, Gordon and Breach, New York.
- Volz, Frederic E. (1972) Infrared absorption by atmospheric aerosol substances, J. Geophys. Res. 77, 1017-1031.

- Wells, W.C., G. Gall and M.W. Munn (1977) Aerosol distributions in maritime air and predicted scattering coefficients in the infrared. Appl. Optics., 16, 543.
- Whitby, K.T. and G.M. Sverdrup (1978) California Aerosols: Their Physical and Chemical Characteristics, Publ. No. 347. Particle Technology Lab. University of Minnesota, Minneapolis, MN.
- Winkler, P. (1973) The growth of atmospheric aerosol particles as a function of the relative humidity. II. An improved concept of mixed nuclei. Aerosol Sci., 4, 373-387.
- Wiscombe, W.J. and G.W. Grams (1976) The Backscattered Fraction in Two-Stream Approximations. J. Atmos. Sci., 33, 2440-2451.
- Woodcock, A.H. (1953) Salt nuclei in marine air as a function of altitude and wind force. J. Meteorol. 10, 362-371.

## 12. APPENDIX: DERIVATION OF APPROXIMATE ANALYTICAL SOLUTION TO RADIATIVE TRANSFER EQUATION

Following Kaufman (1979), the analytical solution to the radiative transfer Equation [(33)-(34)] used in this study is derived by approximating the integral term in the source function  $J$  [Equation (34)] by assuming that the upward ( $\mu > 0$ ) and downward ( $\mu < 0$ ) diffuse (i.e. scattered) intensity fields are independent of direction ( $\mu, \phi$ ) and given by  $I^+$  and  $I^-$ , respectively. Mathematically, this approach may be considered as a two-point quadrature of the angular integration over upper and lower hemispheres. Physically, the method is interpretable as an approximation of the multiply scattered contributions to the intensity field. For incident solar irradiance  $\pi F$ , Equation (34) is approximated as:

$$\begin{aligned}
 J_s(\tau, \pm \mu, \phi) \approx & \frac{F e^{-\tau/\mu_0}}{4} P(\mu, \mp \mu_0; \phi, \phi_0) \\
 & + \frac{I^+}{4\pi} \int_0^1 \int_0^{2\pi} P(\mu, \pm \mu'; \phi, \phi') d\mu' d\phi' \\
 & + \frac{I^-}{4\pi} \int_0^1 \int_0^{2\pi} P(\mu, \mp \mu'; \phi, \phi') d\mu' d\phi' \quad (A.1)
 \end{aligned}$$

Upon substitution of (A.1), the radiative transfer Equation (33) is written separately for each of the two streams,  $I^\pm$ , as:

$$\begin{aligned}
\mu \frac{dI^+}{d\tau} = I^+ - \frac{I^+}{4\pi} \int_0^{2\pi} \int_0^1 P(\mu, +\mu'; \phi, \phi') d\mu' d\phi' \\
- \frac{I^-}{4\pi} \int_0^{2\pi} \int_0^1 P(\mu, -\mu'; \phi, \phi') d\mu' d\phi' \\
- \frac{F}{4} P(\mu, -\mu_0; \phi, \phi_0) e^{-\tau/\mu_0}
\end{aligned} \tag{A.2a}$$

$$\begin{aligned}
- \mu \frac{dI^-}{d\tau} = I^- - \frac{I^+}{4\pi} \int_0^{2\pi} \int_0^1 P(\mu, -\mu'; \phi, \phi') d\mu' d\phi' \\
- \frac{I^-}{4\pi} \int_0^{2\pi} \int_0^1 P(\mu, \mu'; \phi, \phi') d\mu' d\phi' \\
- \frac{F}{4} P(\mu, \mu_0; \phi, \phi_0) e^{-\tau/\mu_0}
\end{aligned} \tag{A.2b}$$

The angular integrations in (A.2a,b) are performed by noting the phase function normalization:

$$\omega_0 = \frac{1}{4\pi} \int_0^{2\pi} \int_{-1}^{+1} P(\mu, \mu'; \phi, \phi') d\mu' d\phi' \tag{A.3}$$

and defining the azimuthally symmetric function,  $P^0$ ; the backscatter fraction for monodirectional radiation,  $\beta$ ; and the backscatter fraction for isotropic radiation,  $\beta'$  as:

$$P^0(\mu, \mu') = \frac{1}{2\pi} \int_0^{2\pi} P(\mu, \mu'; \phi, \phi') d\phi' \quad (\text{A.4})$$

$$\beta(\mu) = \frac{1}{2\omega_0} \int_0^1 P^0(\mu, \mu') d\mu' \quad (\text{A.5})$$

$$\beta' = \int_0^1 \beta(\mu') d\mu' \quad (\text{A.6})$$

Applying these definitions, the intensity Equations (A.2) become:

$$\begin{aligned} \mu \frac{dI^+}{d\tau} &= I^+ - I^+ \omega_0 [1 - \beta(\mu)] - I^- \omega_0 \beta(\mu) \\ &\quad - \frac{F}{4} P(\mu, -\mu_0; \phi, \phi_0) e^{-\tau/\mu_0} \end{aligned} \quad (\text{A.7a})$$

$$\begin{aligned} -\mu \frac{dI^-}{d\tau} &= I^- - I^+ \omega_0 \beta(\mu) - I^- \omega_0 [1 - \beta(\mu)] \\ &\quad - \frac{F}{4} P(\mu, \mu_0; \phi, \phi_0) e^{-\tau/\mu_0} \end{aligned} \quad (\text{A.7b})$$

Assuming that the scattered diffuse intensities are given by the fluxes  $F^\pm(\tau)$  such that:

$$I^\pm(\tau, \mu, \phi) = F^\pm(\tau)/\pi \quad (\text{A.8})$$



Equation (A.7) may be written as:

$$\mu \frac{dI^+}{d\tau} - I^+ = - \frac{\omega_0}{\pi} \left\{ F^+[1-\beta(\mu)] + F^-\beta(\mu) \right\} - \frac{F}{4} P(\mu, -\mu_0; \phi, \phi_0) e^{-\tau/\mu_0} \quad (A.9a)$$

$$- \mu \frac{dI^-}{d\tau} - I^- = - \frac{\omega_0}{\pi} \left\{ F^+\beta(\mu) + F^-[1-\beta(\mu)] \right\} - \frac{F}{4} P(\mu, \mu_0; \phi, \phi_0) e^{-\tau/\mu_0} \quad (A.9b)$$

In matrix rotation, these correspond to equations (40), (41), and (42) in the text.

The flux equations [equations (35), (36) and (37)] in the text may be obtained by integration of equations (A.9) over the angle  $\mu$  to give:

$$\frac{dF^+}{d\tau} = 2F^+ [1-\omega_0(1-\beta')] - 2F^- \omega_0\beta' - \pi F\omega_0\beta(\mu_0) e^{-\tau/\mu_0} \quad (A.10a)$$

$$\frac{dF^-}{d\tau} = -2F^- [1-\omega_0(1-\beta')] + 2F^+ \omega_0\beta' + \pi F\omega_0[1-\beta(\mu_0)] e^{-\tau/\mu_0} \quad (A.10b)$$

Applying the boundary conditions [of equation (38) in the text]:

$$\left. \begin{aligned} F^-(\tau=0) &= 0 \\ F^+(\tau=\tau^*) &= A_L [\pi \mu_0 e^{-\tau^*/\mu_0} + F^-(\tau=\tau^*)] \end{aligned} \right\} \quad (38)$$

the solutions for  $F^\pm$  are [cf (39) in text]:

$$F^+(\tau) = Ae^{k\tau} + Be^{-k\tau} + Ce^{-\tau/\mu_0} \quad (A.11a)$$

$$F^-(\tau) = \frac{1}{\gamma_2} \left\{ A(\gamma_1 - k)e^{k\tau} + B(\gamma_1 + k)e^{-k\tau} + Ye^{-\tau/\mu_0} \right\} \quad (A.11b)$$

where the appropriate constants are given by:

$$\gamma_1 = 2 [1 - \omega_0(1 - \beta')] \quad (A.12)$$

$$\gamma_2 = 2 \omega_0 \beta' \quad (A.13)$$

$$k = (\gamma_1^2 - \gamma_2^2)^{1/2} \quad (A.14)$$

$$A = [B(\gamma_1 + k) + Y]/(k - \gamma_1) \quad (A.15)$$

$$B = (E_1 e^{k\tau^*} + E_2 e^{-\tau^*/\mu_0}) / (E_3 e^{k\tau^*} + E_4 e^{-k\tau^*}) \quad (A.16)$$

$$C = \pi \omega_0 \left\{ \frac{\beta(\mu_0)}{\mu_0} - \gamma_1 \beta(\mu_0) - \gamma_2 [1 - \beta(\mu_0)] \right\} \times \left( \frac{\mu_0^2}{1 - k^2 \mu_0^2} \right) \quad (A.17)$$

$$Y = C \left( \gamma_1 + \frac{1}{\mu_0} \right) - \pi F \omega_0 \beta(\mu_0) \quad (\text{A.18})$$

$$E_1 = Y \left[ 1/(\gamma_1 - k) - A_2/\gamma_2 \right] \quad (\text{A.19})$$

$$E_2 = \left[ -C + \pi F \mu_0 A_L + \frac{A_L Y}{\gamma_2} \right] \quad (\text{A.20})$$

$$E_3 = (\gamma_1 + k) \left[ 1/(k - \gamma_1) + A_L/\gamma_2 \right] \quad (\text{A.21})$$

$$E_4 = \left[ 1 - A_L (\gamma_1 + k)/\gamma_2 \right] \quad (\text{A.22})$$

The solution for the upward (i.e. emergent) intensity,  $I^+(\tau, \mu, \phi)$ , is obtained by integrating equation (A.9) subject to the boundary conditions [see text (43), and (44)]:

$$I^-(\tau=0, \mu, \phi) = 0 \quad (43)$$

$$I^+(\tau=\tau^*, \mu, \phi) = F^+(\tau=\tau^*)/\pi \quad (44)$$

to obtain [compare to text (45)]:

$$I^+(\tau, \mu, \phi) = D_1 e^{\tau/\mu} + \frac{U_1 e^{k\tau}}{1-\mu k} + \frac{U_2 e^{-k\tau}}{1+\mu k} + \frac{U_3 e^{-\tau/\mu_0}}{1+\mu/\mu_0} \quad (\text{A.23})$$

where:

$$D_1 = \left[ \frac{F^+(\tau^*)}{\pi} - \frac{U_1 e^{k\tau^*}}{1-\mu k} - \frac{U_2 e^{-k\tau^*}}{1+\mu k} - \frac{U_3 e^{-\tau^*/\mu_0}}{1+\mu/\mu_0} \right] e^{-\tau^*/\mu} \quad (\text{A.24})$$

$$U_1 = \frac{A\omega_0}{\pi} [1 - \beta(\mu) + \frac{\beta(\mu)}{\gamma_2} (\gamma_1 - k)] \quad (A.25)$$

$$U_2 = \frac{B\omega_0}{\pi} [1 - \beta(\mu) + \frac{\beta(\mu)}{\gamma_2} (\gamma_1 + k)] \quad (A.26)$$

$$U_3 = \frac{C\omega_0}{\pi} [1 - \beta(\mu)] + \frac{\omega_0}{\pi} \frac{\beta(\mu)}{\gamma_2} Y + \frac{F}{4} P(\mu, -\mu_0; \phi, \phi_0) \quad (A.27)$$

The required value of  $F^+(\tau^*)$  in  $D_1$  (A.24) is available from equation (A.11a). The values of  $\beta'$ ,  $\beta(\mu)$ , and  $\beta(\mu_0)$  in the above expressions are obtained from Figure 22, after calculating the appropriate asymmetry parameter,  $g$ , using equation (48). Values of  $\tau^*$  and  $\omega_0$  used above are obtained from equations (46) and (47), respectively, using the modeled optical data for gases and aerosols described in Sections 3 and 5, respectively.